NTNU

Norwegian University of
Science and Technology

Silicon Nitride Waveguide Mach-Zehnder Interferometer Biosensor

Processing of a Biosensor and Investigation
of Biofunctionalization

Morten Hage

Problem Description

The aim of this master´s project is to design and process a photonic biosensor, and the sensor of choice is based on a Mach-Zehnder Interferometer (MZI) configuration with silicon nitride rib waveguides. In-depth study of photonic waveguides and simulation of the MZI was carried out in the project thesis, laying the foundation for the processing.

The MZI will be made on mono-crystalline silicon substrate, and the fabrication process will consist of plasma enhanced chemical vapor deposition (PECVD), electron beam lithography (EBL) and inductively coupled plasma reactive ion etching (ICP-RIE). Characterization will be performed using scanning transmission electron microscopy (S(T)EM) and atomic force microscopy (AFM).

A significant amount of time is expected spent acquiring the necessary experience with NanoLab equipment.

The sensor functionality depends strongly upon the biofunctionalization processes needed for the capture of analytes, and bio-sensing is very much limited by the biofunctionalization chemistry. The sensor surface is to be uniformly coated with antibodies which act as capture agents. The antibodies need to be selective to, and have high affinity towards, the analyte. These requirements are challenging to obtain and is one of the major limitations in the work towards high sensitivity biosensors. Due to this limitation, the issue is addressed with the goal of achieving increased understanding and experience in this field.

The immobilization of catcher antibodies will be performed using fundamental crosslinking chemistry on silicon nitride surfaces. The biofunctionalization process will consist of plasma oxidation, organosilane modification of silicon nitride and covalent immobilization of anti-mouse IgG using carbodiimide crosslinking. Characterization will be accomplished using AFM, contact angle measurements (CAM) and fluorescence microscopy.

Biofunctionalization of silicon nitride is pioneering work at the NTNU NanoLab, and a vast amount of time is expected spent on literature study and getting to know the equipment available at the chemical area at NTNU NanoLab.

Sammendrag

Denne oppgaven omhandler fabrikasjon av bølgeledere i silisiumnitrid med mål om å prosessere et fungerende Mach-Zehnder interferometer (MZI). MZI er velutprøvd og det er forsket mye på bruk av dette i biosensorer da interferometri er en robust og pålitelig metode for direkte deteksjon av analytter.

Fabrikasjonen baserte seg på teoretisk arbeid utført gjennom et forprosjekt, samt geometriberegninger for singel-mode propagering i bølgeledertypen som ble valgt. Metoder for å prosessere bølgeledere i silisiumnitrid ble undersøkt. 'Plasma enhanced chemical vapor deposition' ble benyttet for å deponere silisiumdioksid og silisiumnitrid, karakterisert ved hjelp av refraktometri og 'atomic force' mikroskopi (AFM). En overflateruhet på $3.1\,\mathrm{nm}$ and $0.4\,\mathrm{nm}$ ble funnet på silisiumoksid og silisiumnitrid, respektivt.

Deretter ble elektronstråle-litografi benyttet til å forme bølgelederstrukturen i fotoresist. Med den nyinstallerte Elionix EBL var det kun erfaringen som begrenset resultatene, og kun en justering av eksponeringsdose var nødvendig.

Etsing av ribbe-type bølgeledere ble gjort ved hjelp av tørretsemetoder hvor 'inductively coupled plasma reactive ion etch' (ICP-RIE) ble benyttet. RIE-ets ga en lavere og mer kontrollerbar etserate sammenlignet med kombinert ICP-RIE. Den resulterende ruheten på veggene var dog noe større ved bruk av RIE, men optiske transmisjonsmålinger må utføres for å undersøke effekten av dette.

Mye av utfordringene med biosensor ligger i biokjemien benyttet til å immobilisere f.eks antistoffer, hvis oppgave er å spesifikt fange og binde seg til analytten av interesse. En stor del av denne oppgaven er dermed gitt til å undersøke og utforske kryssbindingskjemi for immobilisering av antistoffer på overflater av silisiumnitrid.

Karbodiimid kryssbindingskjemi ble benyttet for å immobilisere antistoffer på silaniserte overflater av silisiumnitrid, senere karakterisert ved hjelp av

iii

kontaktvinkelmålinger, AFM og fluorescens-mikroskopi. Flere teknikker ble utprøvd og silanisering ved bruk av fordamping av aminosilan og funksjonalisering med lav konsentrasjon av kryssbindingskjemi ble funnet til å gi mest uniform fordeling av antistoffer.

Abstract

The main part of the project is devoted to processing of a MZI waveguide structure using silicon on insulator technology which is carried out at the NTNU NanoLab. MZI is a common interferometry technique that suits bio-sensing applications due to its robustness and rigid sensing mechanism. The processing is based on previous simulations performed in the project thesis, and calculations using the effective index method in order to determine waveguide geometries yielding single-mode propagation.

This work includes silicon dioxide and silicon nitride deposition by plasma enhanced chemical vapor deposition (PECVD), characterized using refractometry and atomic force microscopy (AFM). A surface roughness of $3.2\,\mathrm{nm}$ and $0.4\,\mathrm{nm}$ was achieved for the silicon dioxide and silicon nitride, respectively.

Electron beam lithography (EBL) with a newly installed Elionix EBL was used to pattern the waveguide structures on photoresist. Only a minor adjustment of the exposure dose was necessary in order to achieve satisfying results. However, tuning of the beam current and dot size could provide smoother structures and need to be addressed in order to optimize the waveguide profile.

Dry etching methods by inductively coupled plasma reactive ion etch (ICP-RIE) were used to process shallow rib waveguides in the silicon nitride. The RIE etch tested had a lower etch rate compared to the combined ICP-RIE etch, giving better etch control. The resulting wall roughness was however larger for the RIE etch, but optical transmission measurements are needed to investigate the influence of roughness on light propagation.

The sensor functionality depends strongly upon the biofunctionalization processes needed for the capture of analytes. Bio-sensing is very much limited by the biofunctionalization chemistry due to its critical function of analyte capture. The sensor surface is coated with antibodies which act as capture

agents. The antibodies need to be selective to, and have high affinity towards, the analyte. These requirements are challenging to obtain and is one of the major limitations in the work towards high sensitivity biosensors. Due to this limitation, the issue is addressed with the goal of achieving increased understanding and experience in this field.

Amino-silane was used to generate a surface with primary amines on silicon nitride. Both vapor phase (VP) and liquid phase (LP) silanization were researched, and the methods was characterized using contact angle measurements and AFM. The VP method resulted in more uniformly silanized surface. Carbodiimide crosslinker chemistry was further used to conjugate and immobilize capture antibodies to the amines and fluorescence microscopy was used to characterize secondary antibody fluorescence conjugate that had bound to the primary antibodies. Low crosslinker concentration was found to yield the most uniform fluorescence with less aggregate formation.

Preface

Through my studies at NTNU, I have been introduced to a number of challenges the world as we know it today are facing. The concerns regarding the health of our rapid growing population have triggered my interest for medical diagnostics. New and better technology, suitable for point of care diagnostic instruments could be one solution preventing future pandemics; provide people in developing countries their fundamental medical equipment; and provide us the important feeling of safety in a world with increased focus on health-related issues.

The promising aspects of photonic biosensors inspired me to investigate their function regarding biomarker detection. Through this Master's thesis, fabrication techniques needed for the processing of a waveguide Mach-Zehnder interferometer biosensor have been investigated based on preparations done in the project thesis. Additionally, the intriguing aspect of the challenging topic biofunctionalization has been explored.

Acknowledgements

I would like to thank my supervisor Astrid Aksnes for all her help with my writing, providing superb constructive feedback as well as being a good dialogue partner to discuss the selected topic with.

I would give special thanks to PhD student Jens Høvik for answering recurrent questions regarding the theory and processing methods, giving me a better understanding of the physics behind lithography processes.

Furthermore, I would like to thank division director at NanoLab, Kay Gastinger, for all support, enthusiasm and valuable insight regarding NTNU NanoLab.

I would like to thank professor in nanomedicine at NTNU, Øyvind Halaas, who has been a great asset providing literature recommendations and

Contents

List of Figures

List of Tables

List of Abbreviations

Ab . . . . . .   Antibody

AFM . . . . .   Atomic Force Microscopy

Ag . . . . . .   Antigen

APTES . . .   Aminosilane, 3-aminopropyl-triethoxy-silane

BSA . . . . .   Bovine Serum Albumin

CAM . . . . .   Contact Angle Measurement

CRP . . . . .   C-Reactive Protein

CVD . . . . .   Chemical Vapor Deposition

DIW . . . . .   Deionized Water

DNA . . . . .   Deoxyribonucleic Acid

EDC . . . . .   1-ethyl-3-carbodiimide hydrochloride

EIM . . . . .   Effective Index Method

ELISA . . . .   Enzyme Linked Immunosorbent Assay

FEM . . . . .   Finite Element Method

HF . . . . . .   Hydrogen Fluoride

HMDS . . . .   Hexamethyldisilizane

IBD . . . . . .   Ion Beam Deposition

ICP-RIE . . .   Inductively Coupled Plasma Reactive Ion Etch

IgG . . . . . .   Immunoglobulin class G

IgG2a . . . .   Immunoglobulin G, isotype 2a

IPA . . . . . .   Isopropanol

LOC	Lab on Chip
LOD	Limit of Detection
LB-ADSA . .	Low Bond Axisymmetric Drop Shape Analysis
MES	2-(N-morpholino)ethanesulphonic acid
MZI	Mach Zehnder Interferometer
NHS	N-hydroxysulfosuccinimide
PBS	Phosphate Buffered Saline
PCR	Polymerase Chain Reaction
PDMS	Polydimethylsiloxane
PECVD . . .	Plasma-Enhanced Chemical Vapor Deposition
POC	Point of Care
R	Reactive group
R_a	Average roughness
R_q	RMS roughness
RF	Radio Frequency
RMS	Root Mean Square
RT	Room Temperature
SE	Secondary Electrons
Si	Silicon
Si_3N_4	Silicon nitride
SiO_2	Silicon di-oxide
SOI	Silicon on Insulator
S(T)EM . . .	Scanning transmission Electron Microscopy
TEM	Transverse Electro-Magnetic
TIR	Total Internal Reflection

Chapter 1

Introduction

Optical biosensors that enable label-free protein detection are an attempt to overcome the drawbacks of commercial micro-arrays. The standard detection methods in use today, i.e. enzyme linked immuno-sorbent assay (ELISA) and polymerase chain reaction (PCR), rely on the detection of labeled molecules [1]. In ELISA the label is often an enzyme which catalyzes the added substrate, causing a measurable color change. The color signal corresponds to the amount of analyte present in the sample. The limit of detection (LOD) is rather low, although more recent methods utilize the properties of nanoparticles for signal amplification [2]. The most common label used in PCR is fluorophores, whose fluorescence depends on the amount of analyte present after DNA amplification [3, 4].

The standard ELISA and PCR methods require skilled personnel and expensive, immobile laboratory equipment. The amount of reagents used and the power-demanding thermal cycles in the PCR makes it less suitable for e.g. Point of Care (POC) devices. ELISA uses incubation for binding processes and thermal control is therefore a major challenge in different environments. Additionally, the amount of time these methods require and the needed sample volume makes them non-suitable for rapid diagnosis [3, 4].

Utilizing the sensitive evanescent field in interferometric waveguide biosensors could provide better LOD, and due to the small space and low analyte volume required the sensors could be multiplexed. Maximizing the number of biomarkers a patient sample can be analyzed against is preferred. The greater number of disease markers probed leads to the extraction of more information, much needed in diagnostics [5].

Evanescent field sensors have the ability of label-free sensing, i.e. biomarker

detection without the need of e.g. color or fluorescent tags. This is an advantage that requires fewer sample processing steps and fewer chemical reagents, which is both time and cost saving [1]. Additionally, the chemicals effect on the analyte is also avoided, enabling real time analysis of unaffected biomarkers [5]. However, even though labeling chemistry is redundant, the target analytes still need to be immobilized close to the surface of evanescent field sensors. The most critical limitations regarding biosensing may therefore lie within the field of target immobilization [6].

Silicon and silicon nitride are common materials used in waveguide-based biosensors, and silicon nitride enables the use of visible light, yielding a higher sensitivity compared to infrared wavelengths because the interaction length enters in units of the wavelength [7].

The processing of a silicon nitride waveguide Mach-Zehnder interferometer (MZI) biosensor is investigated in this project based on literature study and simulations performed in the project thesis [8]. In order to get a better understanding of the processes involved in the making of a MZI biosensor, both processing methods and the aspect of biofunctionalization is investigated.

Silicon wafers were used as the substrate, and silicon dioxide and silicon nitride were deposited. This process was carried out using plasma enhanced chemical vapor deposition (PECVD). Imaging of the waveguide pattern in photoresist was done by electron beam lithography (EBL) using a newly installed, top notch Elionix EBL. The etching of the waveguide structures was done by dry etch using inductively coupled plasma reactive ion etching (ICP-RIE). Subsequently characterization of the process steps was conducted using refractometry, scanning (transmission) electron microscopy (S(T)EM) and atomic force microscopy (AFM). It may be worth noting that at the start of this thesis, the author had next to no knowledge regarding lithography techniques, and especially no experience regarding the biofunctionalization involving chemical laboratory work and biochemistry.

The biofunctionalization of silicon nitride has not been done before at the NTNU NanoLab, hence much of the work being done in the first months mostly revolved around taking courses and learning what laboratory equipment to use and how to use it. Anti-mouse IgG antibodies were immobilized on amino-silanized silicon nitride surfaces using carbodiimide crosslinking chemistry. The biofunctionalization protocols were characterized using contact angle measurements (CAM), AFM and fluorescence microscopy.

Chapter 2

Theory

In order to understand the working principle of an optical waveguide, and subsequently a Mach-Zehnder interferometer biosensor, some basic theory is necessary. The fundamental Maxwell's equations, together with boundary conditions and solutions, describing the behavior and propagation of electromagnetic waves, and the time-harmonic Maxwell's equations for source-free media, are provided in Appendix A. Starting with the introduction of dielectric waveguides, moving through the explanation of a Mach-Zehnder interferometer, and finishing off with principles of the commonest biofunctionalization techniques, the following sections will provide a theoretical basis. Most of the theory is taken from the project thesis.

2.1 Dielectric Waveguides

An optical waveguide is based on confinement of light. A medium with a certain refractive index surrounded by media with lower refractive indices, acts as a light trap under certain conditions through the phenomena of total internal reflection (TIR). TIR confines light and can be utilized in waveguides to transport light to and from desired locations [9, Ch. 1.7].

The waveguides ability to confine the light is defined as the ratio between the optical power in the core and the total power [10, Ch. 8.2]. Defining the

propagation direction to be in the z-direction gives the confinement factor

$$\Gamma = \frac{\underset{core}{\iint} |\langle S_z(x,y)\rangle|\ \mathrm{d}x\,\mathrm{d}y}{\overset{\infty}{\underset{-\infty}{\iint}} |\langle S_z(x,y)\rangle|\ \mathrm{d}x\,\mathrm{d}y} \tag{2.1}$$

where $\mathbf{S}$ is the complex Poynting vector describing the electromagnetic power flux [10, Ch 5.3]

$$\mathbf{S} = \frac{1}{2}\mathbf{E}\times\mathbf{H}^*. \tag{2.2}$$

The real part of the Poynting vector is given by [10, Ch 5.1]

$$\begin{aligned}
\mathscr{P} &= \mathbf{E}\times\mathbf{H} \\
&= \frac{1}{2}\,\mathrm{Re}\{\mathbf{E}\times\mathbf{H}^*\} \\
&= \mathrm{Re}\{\mathbf{S}\}.
\end{aligned} \tag{2.3}$$

The confinement factor can also be expressed in terms of the electric field intensity, which is commonly used in simulation software, and is given by [11]

$$\Gamma = \frac{\underset{core}{\iint} |E(x,y)|^2\ \mathrm{d}x\,\mathrm{d}y}{\overset{\infty}{\underset{-\infty}{\iint}} |E(x,y)|^2\ \mathrm{d}x\,\mathrm{d}y}. \tag{2.4}$$

2.1.1   Planar Waveguides

Dielectric waveguides can be obtained with a variety of geometries, but the most common are shown in Figure 2.1.1.

In planar waveguides (Figure 2.1.1a) the light is confined by TIR in one dimension only. The basic geometry is a three-layer structure consisting of materials with different refractive indices. The core interlayer having the highest refractive index is covered above and below by a cover layer and a substrate layer, respectively, with lower refractive indices.
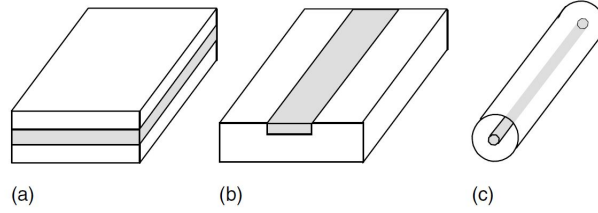
Figure 2.1.1: Main types of dielectric waveguides: (a) 1D planar waveguide; (b) 2D channel waveguide; (c) optical fibre [9].

2.1.2 Channel Waveguides

In 2D channel waveguides (Figure 2.1.1b), the light is confined in two dimensions by TIR since the core region has a higher refractive index than the surrounding media. There are several types of channel waveguides and some of the most common forms are illustrated in figure 2.1.2. Strip waveg-
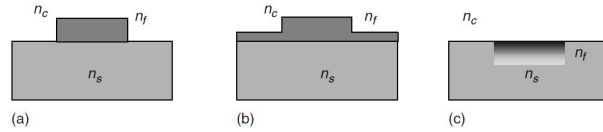
Figure 2.1.2: Main types of channel waveguides (2D waveguides): (a) stripe or strip waveguide; (b) rib or ridge waveguide; (c) buried waveguide. The letters n_f, n_c and n_s indicate the refractive indices of the film, cover layer and substrate, respectively [9].

uides (Figure 2.1.2a) are made either by depositing a high refractive index material on top of a lower refractive index substrate, or by etching a previously deposited high refractive index layer. If the high refractive index layer is not completely etched, a rib waveguide forms (Figure 2.1.2b). By diffusion methods, a local increase of the refractive index in the substrate can be induced, resulting in a buried channel waveguide (2.1.2c). The diffusion process results often in a graded index profile of the buried waveguide. All the common channel waveguides can be manufactured using standard lithographic techniques [9, Ch. 3.1].

Propagation losses due to surface roughness on top and lateral walls are the main challenges regarding strip and rib waveguides. The relative high optical losses ($\sim$ dB/cm) can be reduced by depositing a cladding layer covering the channel. This layer also serves as a protection against the outside

environment that could degrade the waveguide [9, p. 84].

2.1.3   Optical Modes in Dielectric Waveguides

Optical modes are spatial distributions of optical energy in one or more dimensions [12, p. 17]. Electromagnetic modes consist of electric and magnetic field polarizations with the main types: transverse electro-magnetic (TEM), transverse electric (TE) and transverse magnetic (TM). TEM modes can only propagate in an unbounded medium characterized by ϵ and μ, e.g. vacuum free space, and contain neither an E_z nor a H_z component. TM modes do not have a magnetic field component in the propagation direction, i.e. $H_z = 0$, and TE modes do not have an electric field component in the propagation direction, i.e. $E_z = 0$ [9].

Determining modes in slab waveguides are straightforward since the problem can be simplified to a one-dimensional system and is extensively explained in the literature [13, Ch. 10.6][12, Ch. 2]. Consider the planar waveguide in Figure 2.1.3 with the layers assumed to be infinite in the y-
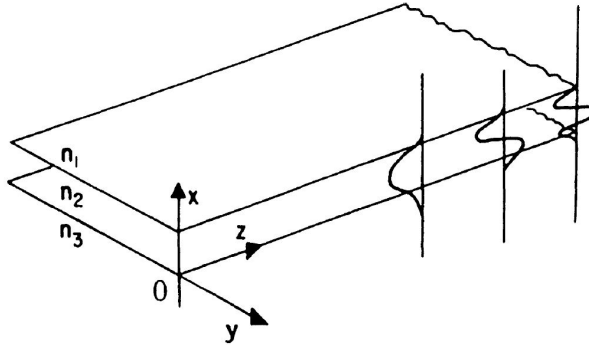
Figure 2.1.3: Illustration of the basic three-layer planar waveguide structure. Three modes are shown, representing the distribution of electric field in the x direction [12].

and z directions. With the light assumed to propagate in the z direction, the electromagnetic fields in each of the three layers are found by eliminating the y component in (A.21a), since the layers are said to be infinite in the y

direction, yielding [12, p. 18]

$$\text{Region 1} \quad \frac{\partial^2 E(x,y)}{\partial x^2} + \left[k_0^2 n_1^2 - \beta^2 \right] E(x,y) = 0$$

$$\text{Region 2} \quad \frac{\partial^2 E(x,y)}{\partial x^2} + \left[k_0^2 n_2^2 - \beta^2 \right] E(x,y) = 0 \qquad (2.5)$$

$$\text{Region 3} \quad \frac{\partial^2 E(x,y)}{\partial x^2} + \left[k_0^2 n_3^2 - \beta^2 \right] E(x,y) = 0.$$

The solutions of (2.5) are either sinusoidal or exponential decaying functions of x in each region, depending on whether $k_0 n_i^2 - \beta^2$, $(i = 1, 2, 3)$ is less or greater than zero. Due to the boundary conditions, the components of $\mathbf{E}(x,y)$ and its derivative must be continuous at the layer interfaces, hence limiting the allowed modes to those illustrated in Figure 2.1.3. Assume a
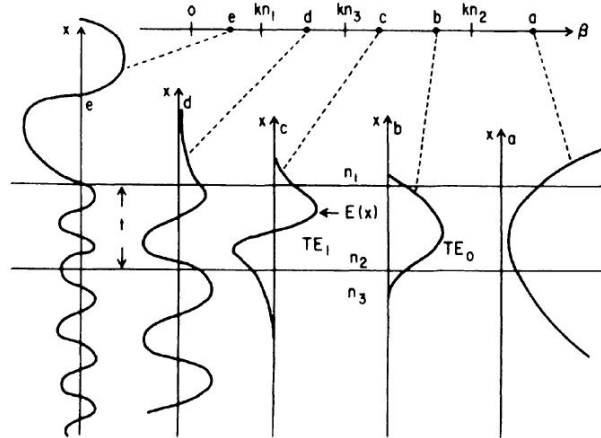
Figure 2.1.4: Possible modes in a planar wavegiude [12].

high refractive index waveguide on a substrate, surrounded by air, giving e.g. $n_2 > n_3 > n_1$. With $\beta > n_2$ (Figure 2.1.4(a)), $E(x,y)$, is exponential in all regions. This nonphysical mode is not realizable due to the requirements of infinite energy to fulfill the conditions. For $k_0 n_3 < \beta < k_0 n_2$, the well confined guided TE modes TE_0 and TE_1 (Figure 2.1.4 (b) and (c)) exist with an exponentially decaying evanescent field extending into the substrate and air. If $k_0 n_1 < \beta < k_0 n_3$ (d), a substrate radiation mode confined on the air interface exists and is useful for optical coupling applications due to poor confinement [12, Ch. 6]. If β is less than $k_0 n_1$ (e), the mode is not guided but oscillates in all three regions, spreading out of the waveguide [12, p. 19].

7

The cutoff conditions for the desired TE modes depend on the wavelength λ, the thickness t of the waveguide layer and on the refractive indices of the layers. Assuming a symmetric waveguide with $n_1 = n_3$, the conditions for the refractive index difference Δn for guided modes is given by [12, p. 20]

$$\Delta n = n_2 - n_1 > \frac{(2m+1)^2 \lambda_0^2}{32 n_2 t^2} \qquad (2.6)$$

where m is the integer mode number.

For the situation regarding two-dimensional photonic waveguides, i.e. where light is confined in both x- and y directions, the mode calculations become more challenging as the field components in the x- and y directions are not independent. Several methods exist for the mode calculations, e.g. Maarcatili's method and the effective index method [9, p. 83-84]. The effective index method (EIM) is chosen as it is used in the FEM simulation software COMSOL Multiphysics.

The effective index method is one of the simplest approximate methods used to obtain the modal fields and the propagation constant in channel waveguides. It is suitable for waveguides having arbitrary geometry and index profiles. The problem is first solved for one dimension, described by the x coordinate, in such a way that the y coordinate acts as a parameter. In this step one obtains a y-dependent effective index profile which is treated once again as a one-dimensional problem to finally obtain the effective index of the propagating mode [9, Ch. 3.6.2].

The propagation constants supported by a two-dimensional waveguide with refractive index depending on the coordinates $n = n(x, y)$ are then calculated by solving the propagation modes for two one-dimensional waveguides. The waveguide is treated as a superposition of two 1D planar waveguides, I and II, illustrated in figure 2.1.5. The planar waveguide I confines the light in the x direction, and for propagating modes mainly polarized along x, the major field components are E_x, H_y and E_z, i.e. TM polarized. Waveguide II confines light in the y direction, with major field components E_x, H_y and H_z, i.e. TE polarized.

Using the reduced wave equation defined by the refractive index function gives

$$\frac{\partial^2 E(x,y)}{\partial x^2} + \frac{\partial^2 E(x,y)}{\partial y^2} + [k_0^2 n^2(x,y) - \beta^2]E(x,y) = 0 \qquad (2.7)$$

where $k = 2\pi/\lambda$ and β is the propagation constant of the mode related to the effective refractive index N by $\beta = k_0 N$ [9, Ch. 3.6].
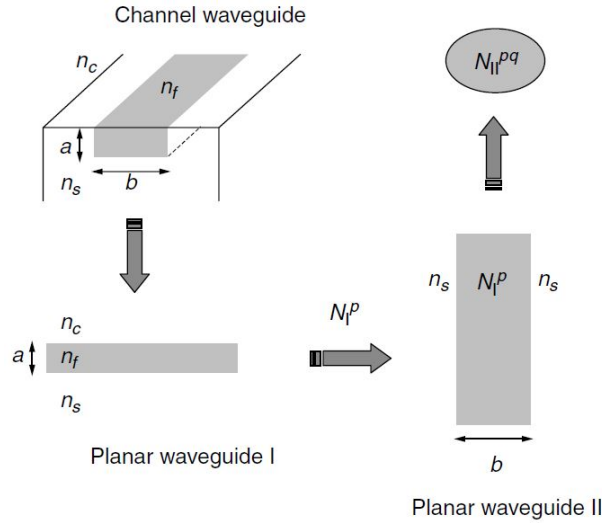
Figure 2.1.5: The figure illustrates how the effective index method splits the 2D waveguide problem into two step-index planar waveguides [9].

The EIM assumes that the function describing the optical field can be factorized:

$$E(x, y) = \Theta(x, y)\Phi(y). \tag{2.8}$$

Substituting the solution into the wave equation for channel waveguides (2.7), gives a system of two coupled differential equations

$$\frac{\partial^2 \Theta(x, y)}{\partial x^2} + \left[k_0^2 n^2(x, y) - k_0^2 N(y)^2 \right] \Theta(x, y) = 0 \tag{2.9a}$$

$$\frac{\partial^2 \Phi}{\partial y^2} - \left(\frac{2}{\Theta} \frac{\partial \Theta}{\partial y} \right) \frac{\partial \Phi}{\partial y} + \left(k_0^2 N^2(y) + \frac{1}{\Theta} \frac{\partial^2 \Theta}{\partial y^2} - \beta^2 \right) \Phi = 0. \tag{2.9b}$$

The first step in the EIM is to solve the differential equation (2.9a) using the y coordinate as a parameter. This equation is similar to that of planar waveguides

$$\frac{\partial^2 E_y}{\partial x^2} + \left(k_0^2 n^2 - \beta^2 \right) E_y = 0 \tag{2.10}$$

and the eigenvalue solution of (2.9a) gives the effective index profile $N(y)$. The second step involves the introduction of the now known $N(y)$ to the second differential equation (2.9b).

The approximation used by the EIM utilizes the assumption that $\Theta(x, y)$ has a slow variation with respect to the parameter y. The partial derivatives of $\Theta(x, y)$ with respect to y can now be ignored as they are close to zero. This leads to the simplification of (2.9b)

$$\frac{\partial^2 \Theta}{\partial y^2} + \left[k_0^2 N^2(y) - \beta^2\right] \Theta = 0. \tag{2.11}$$

From equation (2.9b), a decoupled differential equation is obtained, similar to that for planar waveguides. The solution of (2.11) provides the effective index of the propagating mode in the channel waveguide. The effective index N is defined by two integer numbers p and q, representing the pth and q^{th} order solution of equations (2.9a) and (2.11), respectively.

2.2 Mach-Zehnder Interferometer

The MZI is an interferometric device that can detect changes in the phase of propagating light. A waveguide MZI biosensor is illustrated in figure 2.2.1 and consists of an input- and output waveguide, a beam- splitter and
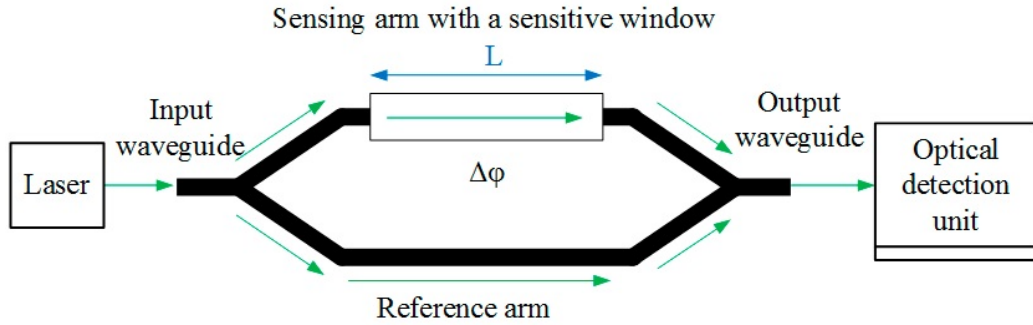
Figure 2.2.1: The figure illustrates the setup of a MZI biosensor. The cladding is removed on the sensing arm, exposing the evanescent field to the media of interest [11].

combiner, a sensing arm and a reference arm. The sensing window is created by exposing the waveguide core.

The coupling factor of the beam splitter should be $3\,\mathrm{dB}$, i.e. the input light is divided equally in each interferometer branch, in order to obtain maximum visibility. The visibility factor gives the contrast between maximum

and minimum intensity, and in addition to the coupling factor dependence, it also depends upon the propagation loss of the optical mode [14]. The visibility factor $\mathscr{V}$ is given by [10]

$$\mathscr{V} = \frac{I_{max} - I_{min}}{I_{max} + I_{min}} \tag{2.12}$$

where I_{max} and I_{min} are the maxium and minimum values of the intensity as the phase ϕ of the light in the sensing arm varies. A MZI biosensor utilizes the evanescent field around the waveguide in the sensing arm in order to detect e.g. protein adsorption. The evanescent field is sensitive to optical changes in the volume surrounding the waveguide surface. When the index of refraction is altered, the effective index of the propagating light changes accordingly, resulting in an additional phase of the light. In biosensing applications, the processes altering the refractive index are the chemical reactions during bioconjugation events, e.g. a binding of one protein to another. In order to detect the phase change gained in the sensing arm, which directly correlates to the alteration in refractive index, the light from the sensing arm is combined with the reference light creating interference. Depending on the difference in phase, the interference could be more or less destructive or constructive, leading to a change in the electric field intensity [15, Ch.9].

2.2.1   Interference

When two monochromatic waves are superposed, the resulting wave is also monochromatic with the same frequency and a complex amplitude [10, p. 63]

$$U = U_1 + U_2. \tag{2.13}$$

The intensity of a monochromatic, plane wave is $I = |U|^2$ and the intensity of the total wave after interference is then

$$I = |U|^2 = |U_1 + U_2|^2 = |U_1|^2 + |U_2|^2| + U_1^* U_2 + U_1 U_2^*. \tag{2.14}$$

With $U_1 = \sqrt{I_1} e^{i\phi_1}$ and $U_2 = \sqrt{I_2} e^{i\phi_2}$, where ϕ_1 and ϕ_2 are the phase of wave 1 and 2, respectively, the total intensity can be expressed as

$$I = I_1 + I_2 + 2\sqrt{I_1 I_2} \cos(\phi) \tag{2.15}$$

with $\phi = \phi_2 - \phi_1$.

The optical intensity that results after combining the two arms of the MZI can be simplified if one assumes that the total intensity is split equally between the reference arm and the sensing arm, i.e. $I_1 = I_2 = I_0$, and the phase in the reference arm is constant, yielding

$$I_T = 2\left|I_0 + \cos(\phi_S)\right| \tag{2.16}$$

with I_T being the total intensity at the output of the MZI, and ϕ_S the phase acquired in the sensing arm.

The optical power, $P(t)$, is the total amount of optical intensity propagating through an area A and is given by [10, p. 44]

$$P(t) = \int_A I(x, y, t)\mathrm{d}A. \tag{2.17}$$

The phase shift is defined in terms of the change in effective index ΔN, over a length L and is given by [15, p. 169]

$$\phi = \frac{2\pi}{\lambda}L\Delta N. \tag{2.18}$$

The equation shows that a linearly change in ΔN will give a sinusoidal optical intensity output after the sensing light has interfered with the reference light. When the evanescent field interacts with e.g. a continuously increasing formation of proteins, an alteration of the refractive index is observed as a change in the output of the MZI.

2.2.2   Sensitivity

Equation (2.18) illustrates that the MZI sensitivity is linearly dependent on the length L of the sensing arm and also dependent on ΔN. ΔN results from the surface reactions and are difficult to enhance directly. The length however is a manufacturing parameter that can be determined. Increasing the length of the arms of the MZI by a factor of two, doubles the sensitivity for the same ΔN [15, Ch. 9.1]. The size of the evanescent field determines the distance from the surface a refractive index change could be detected. A waveguide with a well confined mode, and consequently a small evanescent field, is less sensitive to alterations of bulk refractive index compared to a waveguide with poor confinement [15, Ch. 9.2].

The surface sensitivity for processes involving molecule adsorption from a liquid phase, is defined as the rate of change of the effective index of the mode, N, by the change in thickness of an adsorbed layer of molecules d_l. Assuming an homogeneous adlayer, the surface sensitivity, S_s, can be expressed as a power fraction in the evanescent field [14]

$$S_s \equiv \frac{\partial N}{\partial d_l} = \frac{\gamma_o}{N} \left[\left(\frac{n_l}{n_o} \right)^{2\rho} \gamma_o^2 - \left(\frac{n_o}{n_l} \right)^{2\rho} \gamma_l^2 \right] \frac{P_o}{P_T} \qquad (2.19)$$

with $\gamma_i = k_o \sqrt{N^2 - n_i^2} (i = o, l)$, n_o being the refractive index of the outer medium, n_l the refractive index for the adsorbed molecule layer, P_o/P_T the power fraction of the mode in the cover medium, $\rho = 0$ for TE modes and $\rho = 1$ for TM modes.

2.3 Biofunctionalization

The purpose of biofunctionalizaion is to capture and immobilize the target analyte, e.g. a protein, to a surface in order to detect its presence or concentration. Immobilizing the target is a challenging task. A lot of research is done on the sensor technology, but the most critical limitations regarding biosensing lies within the field of target immobilization [6]. The performance of a protein biochip depends strongly on the immobilization process itself. The chemical and physical properties of the surface influences both specific and non-specific binding of target and non-target proteins. The distance between immobilized proteins and the chip surface determines the sensitivity. Orientation of immobilized proteins might impair binding to large analytes, e,g, other proteins, and the density of proteins on the surface determines chip sensitivity and limit of detection [16]. A flowchart and protocols illustrating the different process steps reviewed below are available in Appendix D.

2.3.1 Surface Activation

Considering the fact that silicon and silicon nitride surfaces oxidize spontaneously in air, producing an amorphous layer of silica complicates the chemical functionalization. In order to get a formation of covalent silicon-carbon bonds, both removal of the oxide layer, and activating the surface for subsequent reaction with organic moieties, are required. The suitable surface activation method depends upon the material to be functionalized. For silicon

and silicon nitride surfaces, treatment with hydrogen fluoride (HF) to generate a hydrogen-terminated surface is common. The surface can then further react with functionalized alkenes. An other alternative is the oxidation of the surface by the use of oxygen plasma, which allows functionalization with organosilanes [16]. For the silicon nitride, an oxynitride layer forms between the silicon nitride and the resulting silicon oxide [17]. Silane compounds are monomeric silicon-based molecules with four constituents. Silanes containing at least one bonded carbon atom are called organosilanes [6, Ch. 13].

Functional silane compounds that contain an organo-functional or organo-reactive arm can be used to conjugate biomolecules to inorganic substrates as shown in Figure 2.3.1. The first step illustrated involves a functional silane
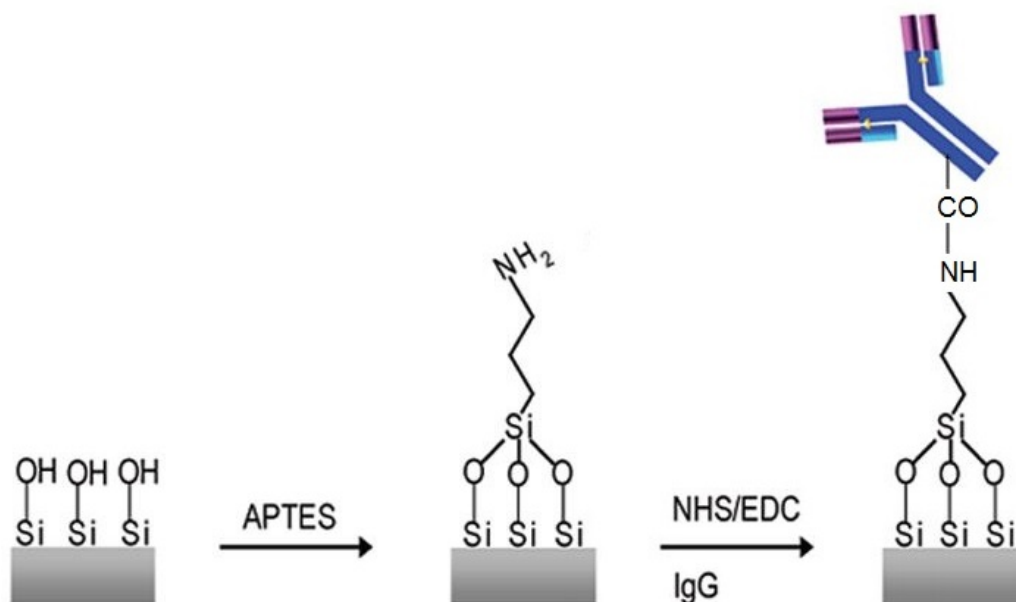
Figure 2.3.1: An IgG antibody is immobilized on a Si surface using APTES and NHS/EDC chemistry. Edited from [18].

agent, APTES (3-Aminopropyl-triethoxy-silane) and is used for the further immobilization af a capture antibody. The general structure of a silane coupling agent is illustrated in figure 2.3.2. The organic arm typically terminates in a functional group or reactive component which facilitates covalent linkage to another organic molecule. The rest consists of silane-reactive groups directly attached to the Si atom and can be of several types. Silicon hydrides comprise simply a hydrogen atom; chlorosilanes are halogen-silicon
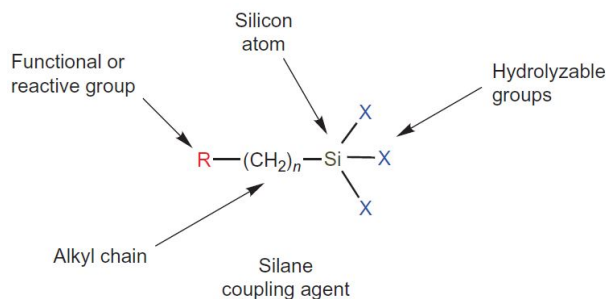
Figure 2.3.2: The general structure of a silane coupling agent. It includes a functional group or reactive group, R, at the end of an organic spacer. The alkyl chain is attached to to the central Si atom which includes up to three hydrolysable groups [6, p. 535].

derivatives; silanols comprise an $-OH$ group; and methoxy- or ethoxysilanes contain methyl ether or ethyl ester, respectively [6, Ch. 13].

The silane coupling agents condensate on the inorganic surface, forming a polymer matrix linked together by $-Si-O-Si-$ bonds. The growing silane network interacts with the inorganic substrate through formation of hydrogen bonding network due to the $-OH$ groups on the surface. The following condensation reaction, that is activated due to heat or vacuum in order to remove water, leads to the formation of covalently linked organosilane polymer on the surface. The thickness of the organo-siloxane layer depends upon the concentration of silane coupling agents and the amount of water in the solution but could be down to three to five silanes thick [6, p. 535-536].

In order to achieve a thinner layer of organosilanes, chlorosilanes and meth-oxysilanes can be reacted in an organic solvent without water present. In water free reactions, no polymer network forms due to the absence of hydrolysis that can form silanols on the silane coupling agents. Additionally, a monolayer forms where each organosilane is coupled directly to the substrate through a siloxane bond. This procedure will however not work for ethoxysilanes as these compounds are not reactive enough without hydrolysis [6, p. 537-538].

The most popular organosilanes for creating a functional group on an inorganic surface are the two silane coupling agents APTES and APTMS (3-Aminopropyl-trimethoxy-silane). The different silane-reactive parts display difference in reactivity toward $-OH$ groups on the substrate surface. The trimethoxy compound is more reactive than the triethoxy compound and can

15

be deposited on substrates using pure organic solvent without the presence of water, as priorly mentioned [6, Ch. 13.2.1]. Surface activation using the aminosilane APTES, in both vapor- and liquid-phase, was recommended by professor in nanomedicine at NTNU, Ø.Halaas.

When using the triethoxy version APTES, the reaction must occur in a partially aqueous environment since the ethoxy groups are not sufficiently reactive to connect spontaneously with the −OH groups on the substrate surface without prior hydrolysis forming silanols. Figure 2.3.3 illustrates the chemical processes involved in APTES deposition. The thicker organosilane
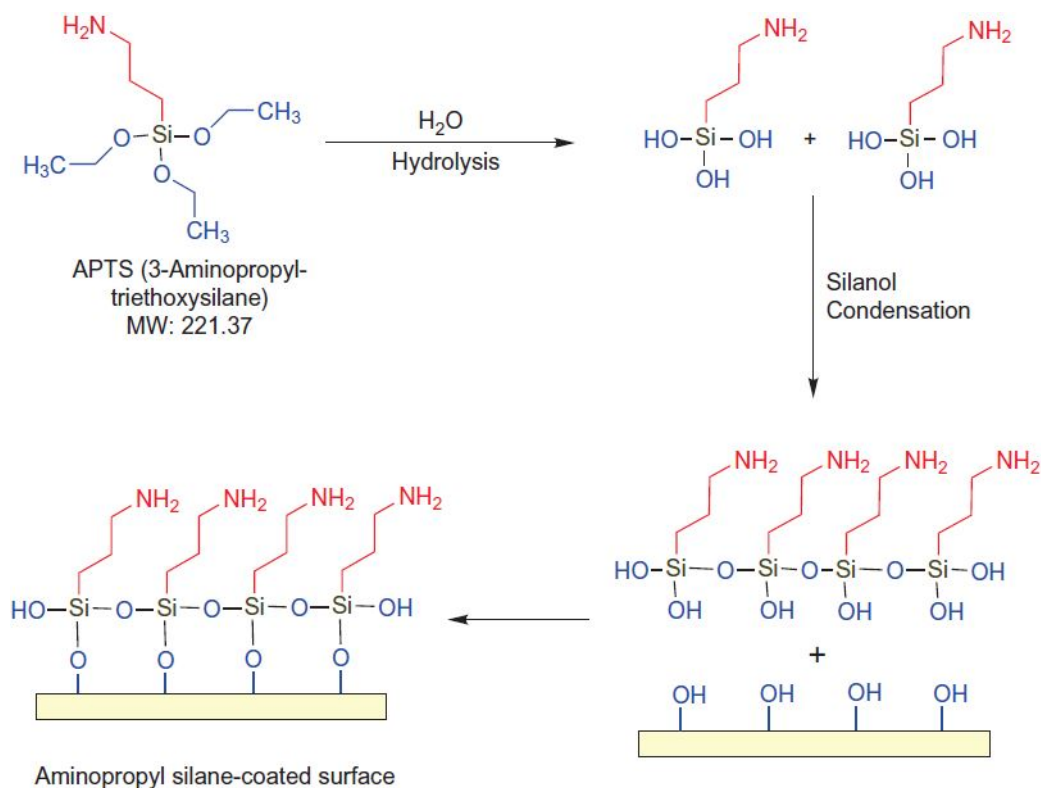
Figure 2.3.3: APTES deposition on an inorganic substrate results in a layer of amine groups that are suitable for subsequent conjugation [6, p. 540].

layer formed, which is around 3 to 8 silanes thick, masks the inorganic substrate with aminopropyl functionalities. Once deposited, the alkoxy groups form a polymer coating with the primary amine groups protruding from the surface, available for subsequent conjugation [6, Ch. 13.2.1].

2.3.2 Bioconjugation

Fundamentally, bioconjugation involves the attachment of one molecule to another in order to create a complex of the linked molecules. Most commonly, at least one of the molecules is of biological origin, whether it is complete, a fragment, or derivative of a biomolecule. The conjugate can also be completely synthetic in some cases, but its use is directed toward biological or life science applications. Designing a bioconjugate suitable for both the target of interest, the method of sensing and the materials chosen in the sensor has a multitude of options. For this reason it is useful to gain knowledge of bioconjugates and methods that others have used successfully, before embarking on a new design [6, Ch. 1].

Carbodiimides are the most popular type of zero-length crosslinkers, i.e. the smallest available reagent systems for bioconjugation, being efficient in forming conjugates between a selection of small molecules, e.g. between two protein molecules, or between a biomolecule and a surface or particle. There are two groups of carbodiimides, water soluble and water insoluble, with the former being the most common choice for biochemical conjugation as biomolecules are soluble in aqueous solutions [6, p. 259].

EDC, 1-ethyl-3-carbodiimide hydrochloride, is a very popular water soluble carbodiimide used for bioconjugation, and perhaps the most frequently used crosslinking agent overall. Along with NHS, N-hydroxysulfosuccinimide, the application in surface conjugation procedures is almost universal [6, p. 259]. The chemical reaction processes involving EDC are described in detail in [6, Ch. 4.1.1], and are suitable to readers that wish to immerse themselves in the topic. Only the most common techniques and reactions regarding EDC are dealt with in the following sections.

Even if EDC is water soluble and very suitable for bioconjugation, it can undergo a number of potential complex side reactions that can complicate the processes and make reproducibility difficult. Figure 2.3.4 illustrates the reactions involved in EDC chemistry. The preferred reaction results in the formation of an intermediate carbocation on the central carbon atom. The modified carbodiimide can itself hydrolyze, forming an inactive isourea that can no longer participate in the process. It can also react with an available ionized carboxylate group to form the desired O-acylisourea reactive ester intermediate. This ester can accept another proton to form a second carbocation on the central C atom, and it is this form of the ester that can react with amine, creating an amide bond. This intermediate can however undergo

a hydrolysis to yield the same undesired isourea derivative which inactivates the compound [6, p. 260-261].
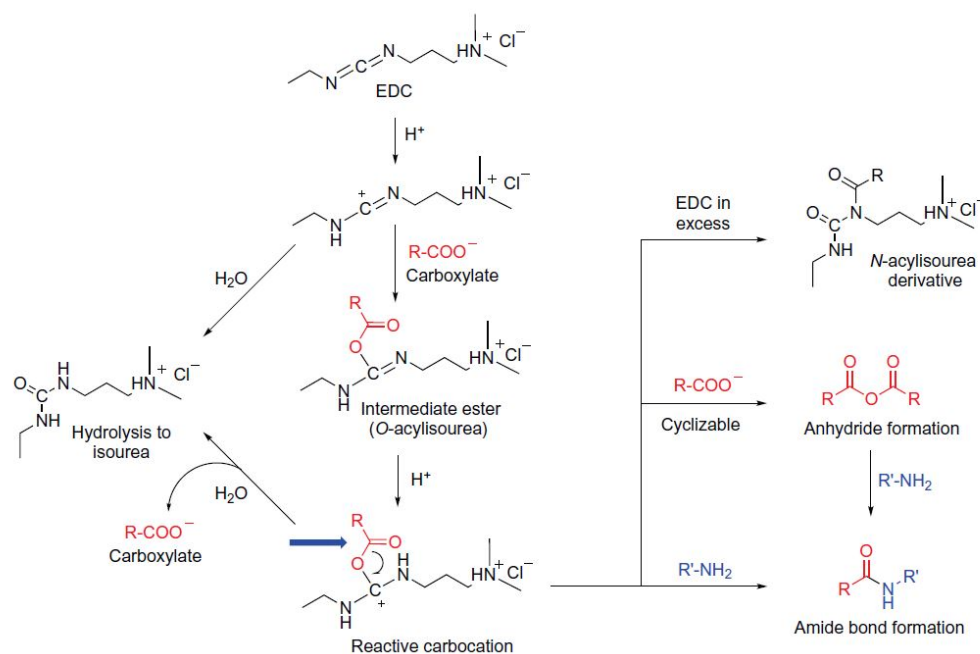
Figure 2.3.4: The number of potential side reactions EDC can undergo, competes with amide bond formations. Hydrolysis may occur in aqueuos solutions, decreasing the yield of the desired conjugate in addition to the possible formation of a permanent EDC complex creating an N-acylisourea derivative [6, p. 261].

In order to make the process more stable, allowing more control of the reactions and higher yield of desired amide bond formations, the addition of NHS or sulfo-NHS is used [6, p. 263]. The addition of NHS or sulfo-NHS in a two-step reaction results in formation of secondary intermediate reactive groups, i.e. NHS esters or sulfo-NHS esters, respectively. This formation of esters results in a more stable intermediate in aqueous solutions than the one formed with EDC only. As a result, the subsequent coupling reaction with proteins proceeds typically with higher yield than with using EDC alone [6, p. 560].

2.3.3 Catcher Immobilization

A catcher is the molecule immobilized on the sensor surface which function is to capture the target analyte. The immobilized catchers yield an affinity layer towards the analyte of interest. In order to capture proteins, e.g. C-reactive protein (CRP), an anti-CRP antibody (Ab) is used. The Ab is commonly an anti-immunoglobulin isotype G2a (anti-IgG2a) and a possible process of immobilizing it to a substrate is illustrated in Figure 2.3.5. The
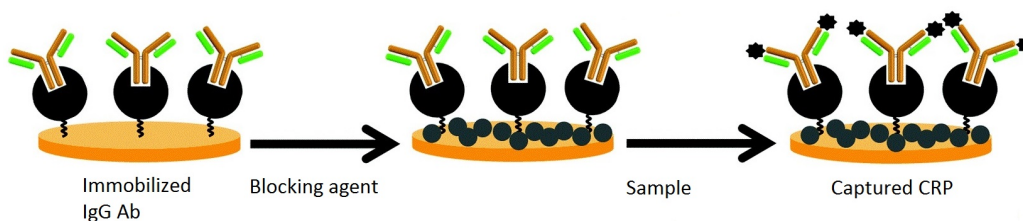
Figure 2.3.5: Immobilization of an antibody (Ab) and capture of C-reactive protein (CRP) on a Si substrate. The process involves blocking of non-specific binding by BSA. Edited from [19].

image illustrates the capture step of a protein. Due to the major challenge of specific binding, several types of proteins such as bovine serum albumin (BSA), casein, serum and others have been used extensively as blockers for non-specific binding sites [6, p. 33-34].

2.3.4 IgG Antibody

Antibodies (Ab) are complex Y-shaped proteins that play an important role in the immune system. For the purpose of this project, only fundamental theory is covered here.

A simplified illustration and a 3D structure of an Ab is shown in Figure 2.3.6. The immunoglobulins (Ig) are built up by four polypeptide chains consisting of two identical heavy (H) chains and light (L) chains [20, Ch. 3]. The first amino acids of the H and L chains are extremely variable among different Ab molecules, and hence named variable (V) region. The reminding carboxyl-terminal region displays less variation and are hence named constant (C). The light chains are each bound to a heavy chain by a disulfide bond as well as by non-covalent interactions between the V_H (variable, heavy) and V_L (variable, light) domains, and the C_H1 (constant, heavy) and

19

C_L (constant, light) domains. The two heavy chains are linked together by multiple disulfide bonds. The antigen-binding regions are made up of amino acids from both the heavy and light chain amino-terminal domains. The Ig base consists of C-terminal domains of the Ab heavy chain. By the use of carbodiimide crosslinker, e.g. EDC, the carboxyl groups found on the carboxy-terminal end can be conjugated to primary amines [21].
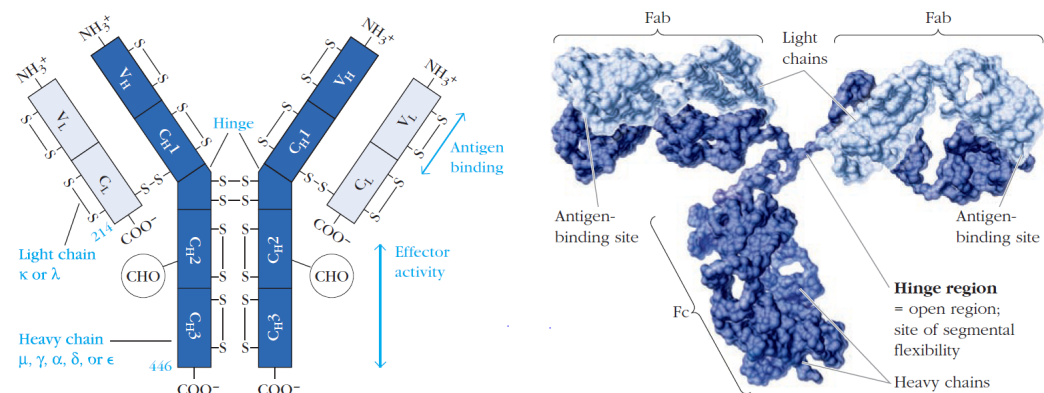
Figure 2.3.6: Simplified illustration of an antibody (left) indicating the different regions and binding events an antibody comprises of, with the amino-groups (NH_3^+) and carboxyl functional groups (COO-) indicated. A 3D representation (right) of an IgG antibody illustrates the 110 amino acid immunoglobulin domains of which the molecule is constructed. IgG antibodies consist of γ heavy chains and κ or λ light chains. The Fab (fragment antigen binding) regions are the antigen binding sites, and the Fc (fragment crystallizable) is a non-antigen binding region [20].

Anti-mouse IgG2a H+L antibodies react with both the heavy and light chain of the IgG antibody, making them suggested for all general immunodetection procedures [22]. The anti-isotype defines that it is specific to the heavy chain class of antibodies [20].

Chapter 3

Methods

Courses necessary to perform the tasks needed at NTNU NanoLab are listed in Appendix B.

The Mach-Zehnder Interferometer (MZI) biosensor processing follows standard lithography techniques and a biofunctionalization protocol adapted to suit the sensor function. Both processing of a waveguide MZI and biofunctionalization are investigated in this project. Due to the limited time, the lithography processes are kept to basics and the biofunctionalization protocols are standard methods where advanced steps involving e.g. blocking agents are omitted. It is still important to mention that the basic lithography processes possible to perform at the NTNU NanoLab are highly advanced.

3.1 The Sensor

An illustration of a possible MZI design is shown in Figure 3.1.1. The CAD drawing illustrates the three material layers the sensor comprises of, i.e. the bottom silicon dioxide (SiO_2) cladding, silicon nitride (Si_3N_4) core and upper SiO_2 cladding. The wafer substrate layer is excluded in the figure. The sensing window is where the upper cladding layer is etched away, exposing the waveguide core which is further functionalized with capture agents.
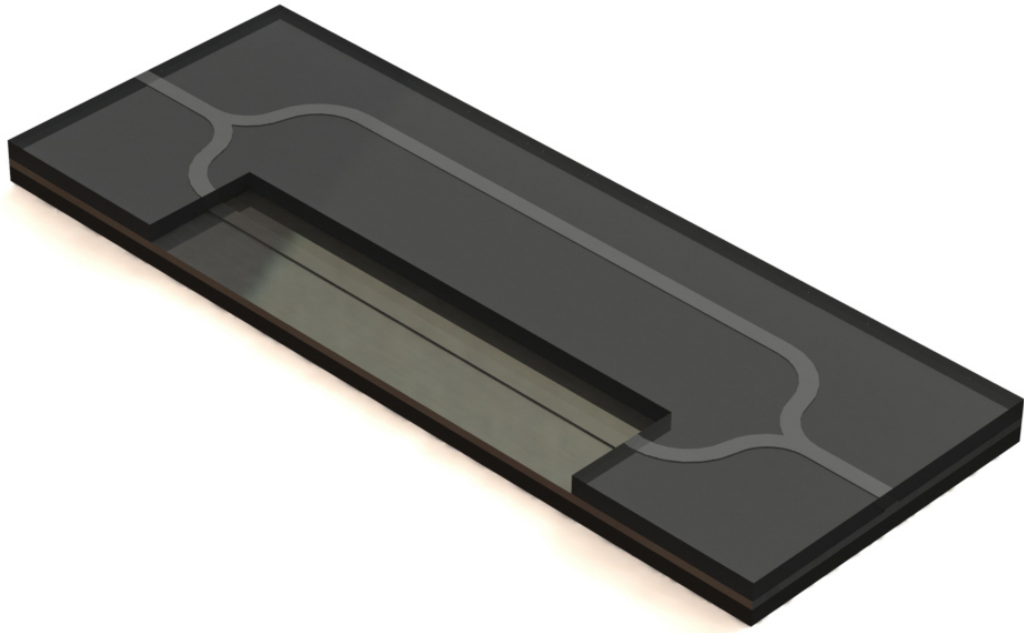
Figure 3.1.1: CAD drawing of a rib waveguide MZI biosensor. The rib is visible through the transparent top silicon dioxide cladding layer. The rectangular area is the sensing window where the cladding layer is etched away, exposing the silicon nitride rib. The lower layer is the bottom silicon dioxide cladding layer. Waveguide dimensions are not to scale.

3.2   Lithography Process

The 8 common steps of photolithography are: [23]

1. Wafer priming

2. Spin coating

3. Soft baking

4. Alignment and exposure

5. Post-exposure baking (PEB)

6. Development

7. Hard baking

8. Develop inspection

The wafer priming consists of cleaning processes in order to remove contaminants, and to promote adhesion of the resist. If needed, the wafer is primed with hexamethyldisilazane (HMDS) to increase adhesion further. For CSAR 62, an alternative to HMDS is available, i.e. AR 300-80 [24]. Priming was not found necessary on silicon nitride, and hence omitted.

3.2.1 Sample Preparation (Scribing)

In order to utilize the wafer material properly, the Dynatex DX-III scriber was used to cut wafers into dies. 4 inch wafers were cut into $15\,\text{mm}\times15\,\text{mm}$ dies for the lithography procedures, and $10\,\text{mm}\times10\,\text{mm}$ dies for the functionalization trials.

The auto-function on the Dynatex DX-III enabled fast and accurate scribing and breaking of a whole wafer. The parameters used for the scribing are listed in table 3.2.1.

Table 3.2.1: Scribe and break parameters used on Dynatex DX-III for whole wafer scribe and sample edge-scribe. (* - edge scribe values)

Scribe Parameter	Value	
Scribe Force	1800 cnts	
Scribe Extension	90 µm	
Scribe Angle	36°	
Approach Speed	9 mm/s	*3.0 mm/s
Scribe Speed	6 mm/s	*2.4 mm/s

Break Parameter	Value
Pressure	65.0 kPa
Anvil Height	0.700 mm
Anvil Gap	0.650 mm
Dwell Time	0.10 sec
Cycle Time	0.20 sec

After deposition of hard ceramics such as Si_3N_4 (Silicon Nitride), the surface becomes more challenging to scribe. Additionally, the scriber tip wear increases radically as silicon nitride is a hard ceramic. By performing

the scribe indent on the back of the wafer, this issue is omitted. Thorough cleaning of the surface is needed afterwards due to the glue residue on the sample surface caused by the glue on the holder film.

3.2.2   Sample Cleaning

In order to remove the silicon dust from the scribing process, ultrasonic cleaning was performed in acetone, ethanol and isopropanol (IPA), each for 2 min.

Up to the step involving photoresist spin coating, the samples were flushed with acetone, ethanol and IPA using squirt bottles, dried with nitrogen and baked at 150 °C for 5 min to remove any solvents prior to each lithographic process step. After the photoresist spin coating, the samples could only be cleaned using deionized water (DIW) and nitrogen until the photoresist was removed.

3.2.3   Material Deposition by PECVD

Plasma-enhanced chemical vapor deposition (PECVD) is used to deposit thin films at lower temperatures compared to regular chemical vapor deposition CVD, at a pressure around 0.5 to 2 Torr. The PECVD process chamber, illustrated in Figure 3.2.1, consists of two electrodes, a gas inlet and exhaust. The PECVD instrument has two power supplies, one RF source (13.56 MHz) and one LF source (50 − 460 kHz). These can be applied to the top electrode either one at a time or simultaneously. The grounded bottom electrode, i.e. the sample stage, is heated to a maximum temperature of 700°C. Gas molecules from an array of nozzles are ionized by the oscillating electric field, and plasma is struck. Electrons are absorbed at the bottom electrode creating a DC voltage of approximately 10-20 V. Ionized gas and radicals react with the substrate creating a deposition process [25].

Silicon dioxide (SiO_2) and silicon nitride (Si_3N_4) were deposited using the Oxford Instruments PlasmaLab System 100 PECVD. Preprogrammed recipes were loaded, and only the deposition time could be adjusted without an engineer present.

The parameters for the SiO_2 and Si_3N_4 deposition are given in Table 3.2.2 and Table 3.2.3, respectively.

In order to prevent undesired chemical reactions from gases used by other users earlier, the desired recipe was run, depositing approximately 200 nm on
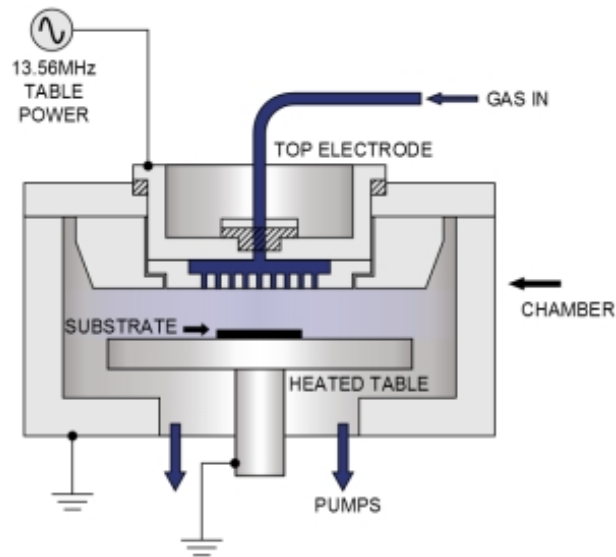
Figure 3.2.1: Sketch of a PECVD machine illustrating the mechanical setup and the positioning of the electrodes, gas inlet and exhaust outlet (PUMPS) [25].

Table 3.2.2: Parameter list for SiO_2 PECVD.

Parameter	Value
SiH_4 gas flow	20.0 sccm
NH_3 gas flow	20.0 sccm
N_2 gas flow	980 sccm
Pressure	650 mTorr
Temperature	300 °C
RF power	20 W @ 13.56 MHz

a dummy wafer to clean the system. Additionally, carrier wafers used were marked and only used for one process recipe, i.e. one carrier wafer for the Si_3N_4 and one for the SiO_2 process.

Table 3.2.3: Parameter list for Si_3N_4 PECVD.

Parameter	Value
SiH_4 gas flow	20 sccm
NH_3 gas flow	20 sccm
N_2 gas flow	980 sccm
Pressure	650 mTorr
Temperature	300 °C
RF power	20 W @ 13.56 MHz
RF automatch capacitor 1	70 %
RF automatch capacitor 2	30 %

3.2.4   Photoresist Spin Coating

The photoresist used is the CSAR 62 (AR-P 6200.13), a positive electron beam lithography (EBL) resist. The samples were mounted onto a vacuum chuck and applied CSAR 62 using a pipette. The sample was then spun for 60 s at 4000 rpm after accelerating at 500 rpms^{-1}. The resulting film thickness was measured to 207 nm, consistent with the 0.20 µm in the given spin-curve [24]. Spinning at 3000 rpm for the same amount of time gave a thickness of 255 nm The latter was used throughout the project since the etch selectivity was unknown. After spin coating, the photoresist was softbaked for 60 s at 150 °C to remove solvents from the resist, polymerizing it.

3.2.5   Mask Design

Digital masks for use with the Elionix EBL were designed using CleWin4. CleWin4 enables easy mask design with .GDSII file output.

The designed masks included straight waveguides with different widths for single mode determination, waveguide bends with a range of bend radii for bending loss determination and Mach-Zehnder Interferometers (MZI) with a selection of waveguide widths, as illustrated in Figure 3.2.2. The green areas are a second mask layer for the later exposure and following etch of the sensing window on the MZI.

Due to the positive photoresist used, the masks had to be inverted. Close-up view of a waveguide splitter, see Figure 3.2.3, illustrates the mask after inversion. The purple areas are exposed and further etched. The white lines
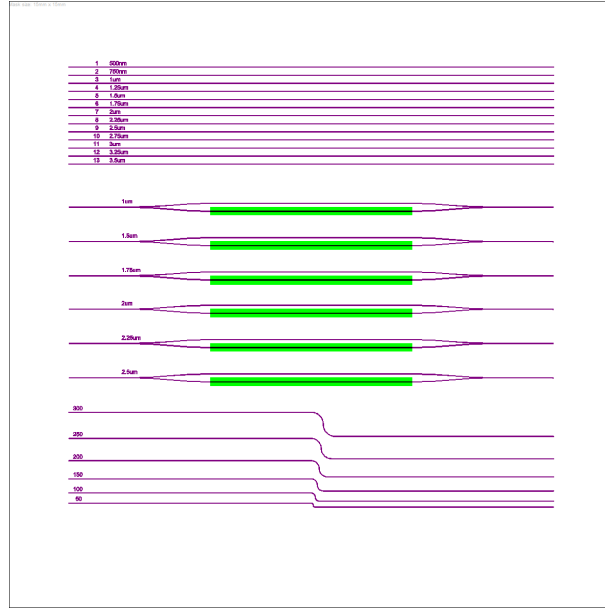
Figure 3.2.2: EBL mask designed in CleWin4. The mask outline fits the dimension of the samples used, i.e. 15 mm × 15 mm. The first layer of the mask is purple and contains the waveguides to be etched in silicon nitride. The second mask layer is green and contains the sensing windows to be etched in the silicon dioxide cladding.

illustrate the waveguide ribs with different dimensions. Selecting the width of the area to be etched so that no light couples to the surrounding material is important. For short waveguides, the separation distance was set to 8 µm. The separation distance between the branches of the MZI was set to 100 µm, commonly used in the literature, to prevent light coupling.

When designing a second layer of the mask, alignment marks need to be generated in order to properly align the second mask, i.e. the mask for the sensing window, on the MZI waveguides. Due to the limited time and wide scope of the project, this second etch step in the silicon dioxide was omitted.

Figure 3.2.3: Magnified image illustrating an inverted mask in CleWin4. The purple areas are to be exposed and further etched, resulting in light-confining ribs (white lines).

3.2.6   Photoreist Exposure by EBL

Elionix ELS-G100 1150 was used to pattern the samples. The Elionix ELS is a 100 kV electron beam lithography (EBL) system with a 100 MHz pattern generator with ZrO/W thermal field emitter. The beam current can be adjusted from 20 pA to 100 nA depending on the exposure dose and photoresist, and the electron beam diameter is 1.8 nm at 100 pA. The EBL can be fully controlled using the computers integrated in the system as illustrated in Figure 3.2.4, but at NTNU NanoLab a separate computer with two monitors is installed to give an enhanced user experience.

The course given by NTNU NanoLab on the Elionix EBL gives the user an introduction to the EBL system. Further self training and exam provides some fundamental knowledge and confidence regarding the system. The following is taken from the EBL short user guide [26] and describes operating procedures for the Elionix EBL used for the electron beam exposure and patterning of the applied photoresist.

Preparations

The photoresist-coated die is mounted on a sample holder (stage) and loaded into the EBL using the exchange chamber. When mounting the sample, care should be taken to ensure that the sample is leveled with the holder surface. If any photoresist residue or contaminants are present under the sample, the sample can be tilted, resulting in reduced exposure precision.

Figure 3.2.4: Elionix EBL with the EBL system (left) with computer controlling units (right). [26]

The exposure dose for the desired photoresist needs to be determined, and initially the dose was set to $300\,\mu C/cm^2$ for the photoresist CESAR 62.

Selecting Beam Memory

Preprogrammed beam memories, which include beam current and aperture size, can be selected. A high beam current results in short exposure time but a following larger electron beam diameter yields coarser lithography resolution. The aperture size follows the beam current chosen, i.e. $120\,\mu m$ aperture for beam currents in the range $100\,pA$ to $10\,nA$ and $240\,\mu m$ aperture for beam currents in the range $10\,nA$ to $100\,nA$. When the beam current is changed, the system will need some time for the beam current to stabilize. Doing this step before loading the sample can be time saving.

Beam Adjustments

In order to achieve optimal results, the beam needs to be adjusted. Moving stage to *Faraday Cup* enables the pico ammeter which measures the beam current. If the value does not match the predefined value from the beam

memory, adjusting the current is possible using the control panel. By moving the stage to *Reference* a SEM image will appear and the focus and stigma of the electron beam can be corrected.

Beam Step Size and Write Field Size

The exposure resolution is determined by the size of the electron beam and the number of times the beam is moved (beam steps), i.e. the number of dots exposed. A write field is the area in which the electron beam exposes the sample before the stage need to move. Large write fields give shorter write time as the stage need to move fewer times, but could result in reduced resolution as the electron beam gets more elliptical when it is deflected. The number of dots indicates the amount of areas within the write field that the electron beam exposes. Large amount of dots give high resolution, but increases the write time drastically. Table 3.2.4 illustrates the exposure resolution as a function of write field size and number of dots. Two additional

Table 3.2.4: Number of dots vs write field size and the resulting resolution. All units in nm [26].

		Write Field		
Dots	100 µm	250 µm	500 µm	1000 µm
50 000	2	5	10	20
200 000	0.5	1.25	2.5	5
500 000	0.2	0.5	1	2
1 000 000	0.1	0.25	0.5	1

larger write fields exists, i.e. 1500 µm and 3000 µm, but these are omitted here as they require lower acceleration voltage of 75 kV and 25 kV, respectively.

Loading Design File

The previous designed mask saved as a .GDSII file is first loaded into WE-CAS, the mask controller window for the Elionix EBL. All circles are treated as polygons in the .GDSII files. By using *Polygon to Circles* the polygons are converted into circular shaped objects. After completed conversion, a .CELL file is generated and a new window *Place CELL* is opened. In the *Place Cell* window, the coordinates for the desired mask position can be added, and the

color of mask appearance can be selected. When finished, the mask position is shown relative to the sample holder.

Assigning Write Fields and Dose

Selecting *Place Writefield* and the desired choice of writing order, i.e. the direction in which the write fields are moved, the write fields are displayed on top of the mask. Selecting the patterning direction such that it follows the geometrical shape of the mask minimizes the chances of stitching error.

The *Dose Calculator* calculates the dose time, i.e. the amount of time the electron beam exposes one dot to achieve the required dose. The calculator is shown in Figure 3.2.5. Dose time is calculated based on the number of dots, write field size, area dose, beam current and pitch. The area dose is photoresist dependent and the number of dots and write field size are already selected. By entering the desired area dose and measured beam current, the dose time is computed. The value should be in the range $0.01\,\mu s/dot$ to $1300\,\mu s/dot$. If the value is too low, the beam current or number of dots should be reduced, or alternatively the pitch could be increased. If the pitch is set to e.g. 2, the beam will only expose every second dot hence increasing the dose time needed in order to obtain the correct area dose. If the value is too high, the beam current or number of dots should be increased, or the pitch could be decreased. When the dose time is acceptable, the dose time
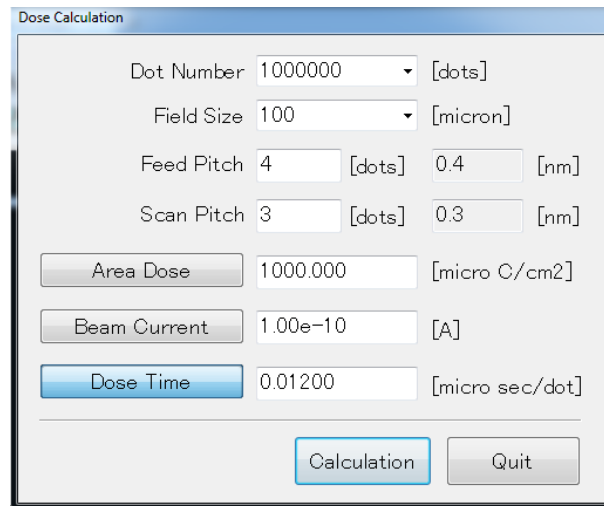
Figure 3.2.5: Dose calculator used in order to calculate the dose time.

value and pitch is entered in the *Set Color/Pitch/Dose* menu. A .CON file should be saved before further processing.

Edit Schedule Execution

With *Exit Schedule Execution*, the saved .CON file could be loaded. Using *Matrix .CON file* the mask can be copied into a matrix and the different copies can be assigned individual area dose values if desired.

The main option of concern in the *Set Options* menu is the height sensor. A laser measures the sample height continuously and the stage is corrected if the height deviates from the tolerance. The *Z Preset* should be set to $6.4 - T$ with T being the sample thickness. For regular 4 inch wafers, the value is set to 5.8. To avoid exposure abortion if height measurement fails, the *HS Error Process* is set to *Cont.* instead of *Abort*. When finished press next. and the CAD window appears.

In the CAD window, selection of sample holder enables the display of different sample holders. The sample holder *Multi-piece Cassette* was chosen and the size was set to $15\,\text{mm} \times 15\,\text{mm}$ to fit the mounted die.

To measure sample inclination, the stage is first moved to the bottom left corner, ideally close to the exposure position, of the sample by selecting *Move Stage* and clicking on the desired point on the sample. When *Measure Sample Inclination* is selected, the window illustrated in Figure 3.2.6 appears. The points A, i.e. where the stage is, B and D must be within the sample area. Dx and Dy is used to adjust the position of B and D with respect to A.

Resulting inclination values should all be $<1\,\text{mrad}$ for small dies. If one or more of the tilt angles exceed this value, the sample might be removed and cleaned underneath. High tilt might result in low exposure precision.

Field Correction

In order to reduce stitching error, i.e. nonalignment of structures at write field boundaries, *Field Correction* should be run before exposure is executed. The field correction utilizes prefabricated features on the stage to calibrate stage movement reducing stitching error.

Start Exposure

Before starting the exposure, calculating the write time should be done in order to display this and be able to illustrate exposure progress.
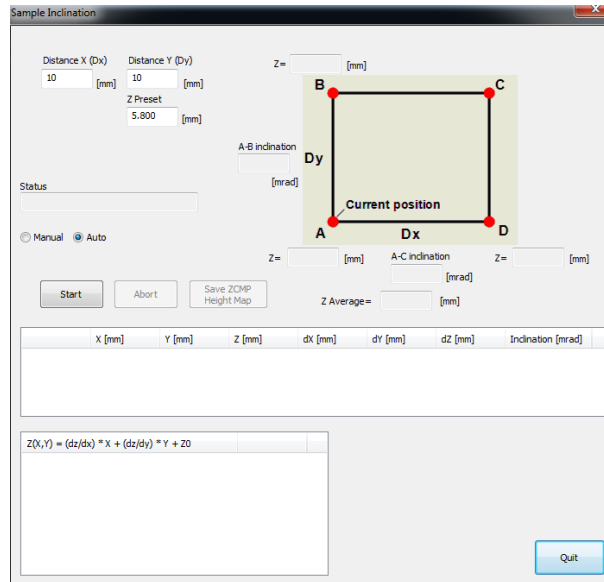
Figure 3.2.6: Sample Inclination menu for sample tilt measurement. The resulting tilt should be <1 mrad for small dies.

The exposure starts when *Exposure* is selected and the checklist is accepted.

3.2.7 Photoreist Development

The exposed photoresist was removed using developer CSAR 546 (AR 600-546). The patterned samples were immersed in a beaker containing the developer for 60 s while the beaker was gently stirred. To terminate the developing process, the sample was immersed in IPA for 30 s and rinsed thoroughly in DIW.

3.2.8 Material Etch by ICP-RIE

Inductively coupled plasma reactive ion etch (ICP-RIE) is an anisotropic dry-etching process used to remove material with the use of chemically reactive plasma under low pressure, approximately 1 mTorr to 100 mTorr. The ICP-RIE contains two separate RF generators, providing individual control over ion energy and ion density, one to strike plasma and one to generate a DC bias to accelerate the plasma ions from the plasma towards the sample surface.

The two RF sources are in the following labeled ICP generator and RIE generator, respectively. The setup is illustrated in Figure 3.2.7 [27].
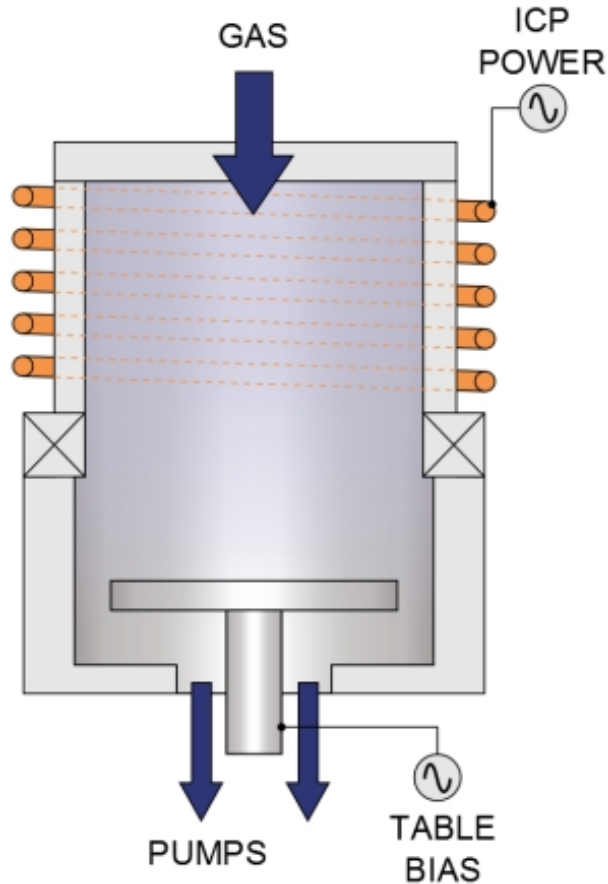
Figure 3.2.7: Sketch of an ICP-RIE machine illustrating the mechanical setup and the positioning of the electrodes and gas- inlet and outlet. The top ICP electrode generates plasma, while the bottom (substrate) electrode creates a table bias to accelerate the ions [27].

Silicon nitride was etched using Oxford Instruments Plasmalab System 100 ICP-RIE 180 [28]. The etch rates on silicon nitride were especially important to investigate in order to achieve uniform shallow etch for the rib waveguides. Preprogrammed recipes were loaded, and only the deposition time could be adjusted without an engineer present.

Parameters used in the etch recipe for silicon nitride are listed in Table 3.2.5. The two recipes differ only in the etch principle, i.e. ICP and RIE.

34

Table 3.2.5: Parameter list for ICP-RIE silicon nitride etch. Two recipes are listed, one ICP-RIE and one RIE etch.

ICP-RIE Etch Parameter	Value
O_2 gas flow	5.0 sccm
CF_4 gas flow	5.0 sccm
CHF_3 gas flow	30.0 sccm
Pressure	22 mTorr
Chiller temperature	20 °C
ICP power	100 W @ 13.56 MHz
RIE power	100 W @ 13.56 MHz

RIE Etch Parameter	Value
O_2 gas flow	7.0 sccm
CF_4 gas flow	10.0 sccm
CHF_3 gas flow	50.0 sccm
Pressure	22 mTorr
Chiller temperature	20 °C
ICP power	0 W @ 13.56 MHz
RIE power	175 W @ 13.56 MHz

The gas flows for the RIE etch are initially higher, but the system available is limited at 50.0 sccm on CHF_3, and the rest of the gases are then downscaled to maintain the ratio.

The heavy fluorine (F) ions are the main component for material sputtering. Together with carbon (C), polymerizing fluorocarbon films are generated that decreases the etch rate and can hence be used for etch control. The added oxygen (O_2) binds to carbon and reduces the fluorocarbon film formation [29].

A new etch recipe was requested from Oxford Instruments. This should yield a slower and more controllable etch rate for silicon nitride, and the parameters are listed in Table 3.2.6.

Table 3.2.6: Parameter list for the Si_3N_4 etch recipe requested from Oxford Instruments. The etch rate is given and not verified for the PECVD silicon nitride used in this project.

ICP-RIE Etch Parameter	Value
CHF_3 gas flow	32 sccm
SF_6 gas flow	8 sccm
Pressure	3 mTorr
Chiller temperature	20 °C
ICP power	600 W @ 13.56 MHz
RIE power	6 W @ 13.56 MHz
DC Bias	−120 V
Etch Rate	47 nm/min

3.2.9   Photoresist Strip

To strip the photoresist CSAR 62, the samples were rinsed in remover CSAR 600-71 for a minimum of 30 s. Ultrasonic bath was used to increase the rinsing efficiency ensuring that no photoresist residue was left. The samples were further rinsed in acetone and dried with nitrogen gas to remove stripper residues. To ensure totally clean samples, plasma oxidation was performed using the Diener Electronics Femto Plasma Cleaner for 1 min, at 100 % power and O_2 gas flow.

3.3 Biofunctionalization Process

In order to investigate immobilization protocols, biofunctionalization was performed on clean PECVD Si_3N_4, characterizing each process step along the way.

Biofunctionalization of silicon nitride surfaces is pioneer work at the NTNU NanoLab, as few projects have covered protein immobilization.

The main steps involved in the conducted biofunctionalization are listed below.

1. Oxygen plasma treatment

2. Surface silanization

3. Immobilization of catcher antibodies

4. Characterization

3.3.1 Materials

Anti-mouse immunoglobulin G (anti-IgG H+L), APTES (3-aminopropyl-triethoxysilane $NH_2(CH_2)_3Si(OC_2H_5)_3$, 99 %), EDC (N-(3-dimethylamino-propyl)-N'-ethylcarbodiimide hydrochloride), NHS (N-hydroxysuccinimide, 98 %), acetic acid (99 %) and acetone (99.9 %) were bought from Sigma-Aldrich. Mouse IgG2a Alexa Fluor$^®$ 488 conjugate was bought from Thermo Fisher. Phosphate-buffered saline pH 7.4 (PBS 1X: 10 mM phosphate, 2.7 mM potassium chloride, 137 mM sodium chloride, and 2.7 mM potassium phosphate) was prepared in sterile water using Dulbecco A Tablets. 2-(N-morpholi-no) ethanesulfonic acid buffer (0.1 M MES) was prepared in sterile water, the pH was adjusted to 5.5 using sodium hydroxide, and the solution was filtered through 0.2 µm sterile filter for storage. A detailed listing of the chemicals used are given in Appendix D, Table D.3.1.

3.3.2 Surface Oxidation

The silicon nitride surface on the samples was oxidized using a Diener Electronics Femto Plasma Cleaner for 60 s, at 50 % power and O_2 gas flow, to remove organic contaminants and grow an oxide layer making the surface more hydrophilic. The effect of the plasma cleaning was characterized using contact angle measurements, see 3.4.5.

Thoroughly cleaning of the surface is commonly achieved using either piranha solution [30], diluted hydrofluoric acid (HF) [31] or both [32]. These methods remove native oxide layers and organic contaminants and is of great importance. However, the silicon nitride was deposited shortly prior to the functionalization and stored in the clean-room facility at all times. Due to this and the fact that both piranha and HF are aggressive chemicals which use should be minimized, this cleaning step was omitted in this study using only oxygen plasma.

3.3.3   Silanization

The aminosilane (APTES) was used for the surface silanization. Both liquid phase and vapor phase silanization methods were investigated.

For the liquid phase protocol 2 % APTES was dissolved in ethanol containing 4 % water and the solution was incubated for 5 min at RT to form silanols by hydrolysis. According to Hermanson [6], acetic acid should be used to lower the pH of the solution to 4.5-5.5 to increase the rate of amine formation and improve the ability of antibody conjugation. The pH was adjusted to approximately 5. The oxygen plasma treated samples were immersed in the APTES solution for 1-15 min. Sonication for 2 min in ethanol following the silanization was done in order to remove excess, unreacted APTES. Different volumetric concentrations and pH values were tested and the resulting silane layer was characterized using atomic force microscopy (AFM) and contact angle measurements.

Vapor phase silanization was performed at RT using a desiccator. The samples were placed in the desiccator and vacuum was applied for 10 min to remove humidity. APTES (500 µL) was added to an Eppendorf tube, and the tube was placed next to the samples. When the vacuum was applied again, some of the APTES evaporated resulting in silane-vapor being deposited on the samples. The vacuum valve was cycled every hour to ensure vacuum pressure at all times.

3.3.4   Immobilization of Catcher Antibody

The following protocols regarding immobilization of the catcher antibody are adapted from Hermanson [6, Ch. 4.1.1] and Vashist [33, 34], and are illustrated in the flowcharts D.1.1 and D.1.2 in Appendix D.

Solutions containing EDC and NHS was freshly prepared in 0.1 M MES pH 5.5 and PBS (1X) pH 7.4, respectively. The primary antibody, i.e. anti-mouse IgG, was diluted in 0.1 M MES pH 5.5.

Method I

Anti-mouse IgG antibody, 990 µL and 500 µL of 100 µg/mL, was incubated for 15 min at RT with 10 µL and 500 µL, respectively, of the crosslinking solution, i.e 5 µL of EDC (0.25 mg/mL) + 5 µL of NHS (0.6 mg/mL); 5 µL of EDC (2.5 mg/mL) + 5 µL of NHS (6.0 mg/mL); 450 µL of EDC (21.3 mg/mL) + 50 µL of NHS (11.5 mg/mL). In all three chemistries the final volume was 1000 µL. The molar excess of EDC over the amount of IgG was 10-fold, 100-fold and for the latter the final concentration of EDC was 50 mM. The EDC/NHS molar ratio was 1:4, 1:4 and 1:10 for the three chemistries, respectively. This approach is later referred to as method I.

Stepwise adding of EDC was conducted in the third chemistry due to the high EDC concentration and the risk of hydrolysis and EDC deactivation. This was done by adding 150 µL of the 21.3 mg/mL first simultaneously with the 50 µL NHS, and thereafter every 5 min for 15 min. Stepwise adding of EDC might be necessary to avoid hydrolysis and EDC deactivation.

This led to the activation of carboxyl groups on anti-IgG antibodies. Thereafter, the EDC-NHS-activated anti-IgG antibodies were immobilized on the APTES-functionalized surfaces by adding 30 µL droplets and incubate at RT for 2 h before the samples were thoroughly cleaned with PBS and stored in the refrigerator upon characterization.

Method II

A second approach was also investigated, later referred to as method II. The incubation of antibodies (Ab) together with the EDC/NHS solution could lead to the formation of aggregates as the proteins bind to each other. Activating the amino-silanized surface prior to the adding of antibodies prevents this Ab-Ab bonding because they have not been activated by the carbodiimide crosslinker (EDC). The following protocol is adapted from Kim et al. [35] and Didar et al. [36], and is illustrated in the flowchart D.1.2 in Appendix D. The concentration of anti-mouse IgG, EDC and NHS are identical to those in method I. EDC and NHS were dissolved in MES due to the desired pH for the EDC and the fact that these were to be mixed at equal volumes.

The EDC and NHS were mixed at ratio 1:1 and added as 10 µL droplets on the amino-silanized samples and incubated for 2 h at RT.

This lead to the activation of primary amines on the silanized surface. After thoroughly cleaning in PBS, 10 µL droplets of anti-mouse IgG antibody 100 µg/mL was applied and further incubated over night at 4 °C.

3.3.5 Secondary Antibody

Mouse IgG2a isotype control mouse IgG Alexa Fluor® 488 conjugate [37] was used as secondary antibody with fluorescent markers. The Alexa Fluor® 488 is effectively excited by the 488 nm laser line and has emission maximum at wavelengths above 525 nm.

3.4 Characterization

The characterization steps are of utmost importance as it is the only indication on the process quality prior to the finished product.

3.4.1 Atomic Force Microscopy

The atomic force microscopy (AFM) Veeco Metrology Multimode V [38] was used to measure surface roughness and characterize changes given by process steps in the functionalization. Bruker ScanAsyst AIR tip with 2 nm (nom) radius mounted on an aluminum coated silicon nitride cantilever was used [39]. Scanning stage E gave a maximum scan area of approximately $12 \times 12 \, \mu m^2$ and high resolution. The scan parameters used in tapping mode are listed in Table 3.4.1.

Table 3.4.1: Parameter list for AFM measurements.

Parameter	Value
Scan size	0.1 µm to 10 µm
Scan rate	0.8 Hz
Scan resolution	256/512 samles/line
Scan mode	ScanAsyst/PeakForce QNM
Aspect ratio	1 (square image)

Image Processing

Both Nanoscope Analysis v1.50 and the free software Gwyddion v2.44 were used in order to process the raw data images obtained from the AFM scans. Flattening algorithms were applied in order to correct for some AFM artifacts. The most common error is line errors where profiles in the fast scanning axis is mutually shifted. This results in curved or creased images as illustrated in Figure 3.4.1(a).

After performing *Align Rows* in Gwyddion, or *Flattening* (3D) in Nanoscope Analysis, the resulting image is as illustrated in Figure 3.4.1(b). Care should be taken when flattening AFM images with profiles, e.g. waveguides, as some flattening algorithms could make the data distorted.

a   b
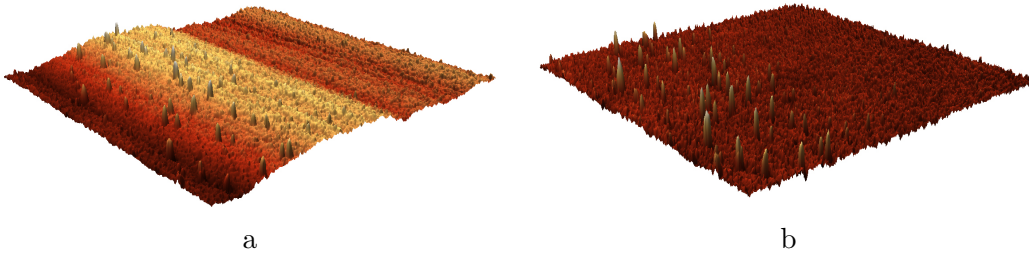
Figure 3.4.1: AFM image (3D) before (a) and after (b) applied flattening algorithm.

Surface Roughness

Surface roughness is an effective parameter when it comes to comparing film structures and surface characteristics. The two parameters used are the average roughness (R_a) and the Root Mean Square (RMS) roughness (R_q), illustrated in Figure 3.4.2 [40]. The average roughness expresses the arithmetical mean of the absolute values of Z(x) along the sampling length. When applied on a 2D surface, the resulting R_a is the average of all sampled lines. This method minimizes the influence of a single injury on the measurement.
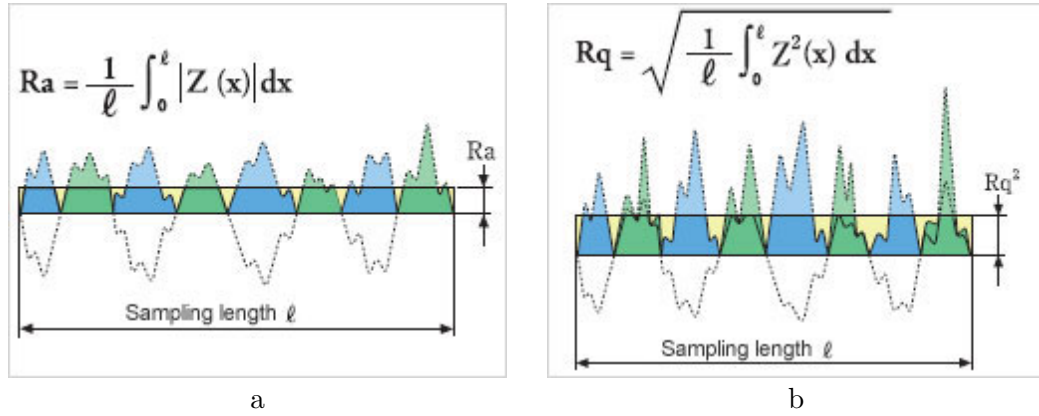
Figure 3.4.2: (a) Average roughness; (b) Root Mean Square (RMS) roughness. The sampling is done along the x-axis with z(x) being the height at each sample point x [41].

3.4.2   Refractometer

The Filmetrics F20 works in the wavelength range $380\,nm$ to $1050\,nm$ and measures optically smooth films with thickness in the range $15\,nm$ to $70\,nm$ [42]. Precautions were taken when multiple films were measured, e.g. Si_3N_4 on SiO_2 due to inaccuracies in their respective refractive indices. Increasing the dynamic range for the refractive index in the materials could give better goodness of fit but care should be taken when working with multiple layers of film.

3.4.3   Scanning Electron Microscopy

Hitachi S-5500 scanning (transmission) electron microscope (S(T)EM) [43] is an in-lens cold field emission electron microscope with acceleration voltage 0.5-30 kV, beam current $0.1\,\mu A$ to $20\,\mu A$ and detectors for secondary electrons (SE); low- and high-angle back scattered electrons (BS); bright-field and dark-field transmission measurements; and Bruker XFlash EDX detector for classification. Of the previous mentioned, mainly SE was used to characterize the structures.

Isolating samples, e.g silicon nitride on silicon dioxide, is challenging to view in SEM and low current should be used to avoid charge build-up and following charging effects. Alternatively, characterization of deposition thick-

ness and etch recipes of silicon nitride could be performed using thin layers of silicon nitride on mono-crystalline silicon, without the silicon dioxide.

Sample size restriction of $9\,mm \times 5\,mm$ and $7\,mm \times 3.5\,mm$ for the surface and cross section stage, respectively, required dividing the dies into smaller samples.

3.4.4   Fluorescence Microscopy

Carl Zeiss Axio Scope.A1 430035-9120-000 is a combined epi- and transfluorescence microscope which was used to characterize the uniformity of adsorbed secondary antibodies. Due to the opaque samples, only the epifluorescence setup was used. Filter kit 38 HE was used for the Alexa Fluor® fluorescent dye, with excitation filter 470/40 and emission filter 525/50 [44]. The filter transmission along with the excitation and emission band of the dye is illustrated in Figure 3.4.3.

All fluorescence images were captured using a Carl Zeiss 40x LD Plan-NEOFLUAR high-resolution objective and Carl Zeizz AxioCam MRc firewire camera with 1388×1040 pixel sensor. This resulted in an area coverage of $35\,\mu m \times 25\,\mu m$.
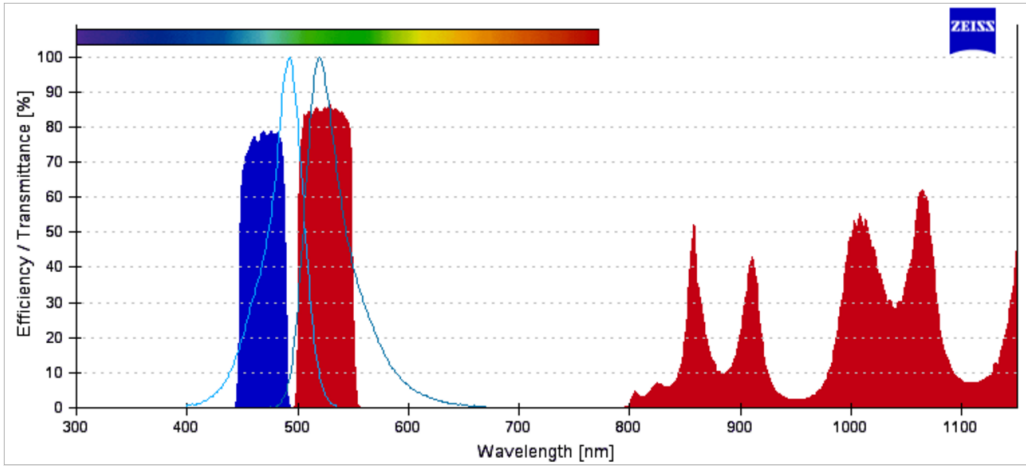
Figure 3.4.3: The graphs illustrate the excitation band (left) and emission band (right) for the Alexa Fluor® 488 dye. The blue and red areas indicate the excitation and emission filter, respectively [44].

3.4.5   Contact Angle Measurement

Using a HOT 50-500X USB microscope, contact angle measurements were performed in order to characterize processing methods regarding the biofunctionalization. Micro-pipettes were used to apply $5\,\mu L$ droplets of de-ionized water (DIW) and a high contrast image of the droplet was captured within $30\,s$. Limiting the time between droplet application and image capture is important in order to minimize the effect of evaporation. When the water evaporates, the droplet volume decreases whereas the contact area stays approximately unchanged [45]. This results in a continuously decrease in measured contact angle.

This static measurement method for determining contact angle is better known as the sessile drop method.

The contact angle of the droplet was measured using ImageJ software with DropSnake and (LB-ADSA) drop analysis plugin. The setup is illustrated in Figure 3.4.4.

In order to get a setup with reproducibility, the camera angle was set to $3°$ [46] by using a printed ellipse which at $3°$ appears as a circle.

Figure 3.4.4: Contact angle measurement setup with the HOT USB microscope to the left, adjustable sample stage with a $10 \times 10\,mm^2$ sample, and a primitive halogen light source to the right. A plastic box was used as a light diffuser.

The DropSnake plugin utilizes the drop's reflection to get a more accurate measurement of the triphase points, i.e. the surface endpoints indicating the interface between the drop and its reflection [47]. This plugin is ideal for measuring asymmetric drops since no shape assumptions are used, and is especially useful if the drop is on a tilted surface or is skewed. The Drop-Snake places knots on the interface between the drop and background using gradient-based edge detection and draws a curve between them determined by a smoothing radius. The angle is calculated and given in the image directly as illustrated in Figure 3.4.5.
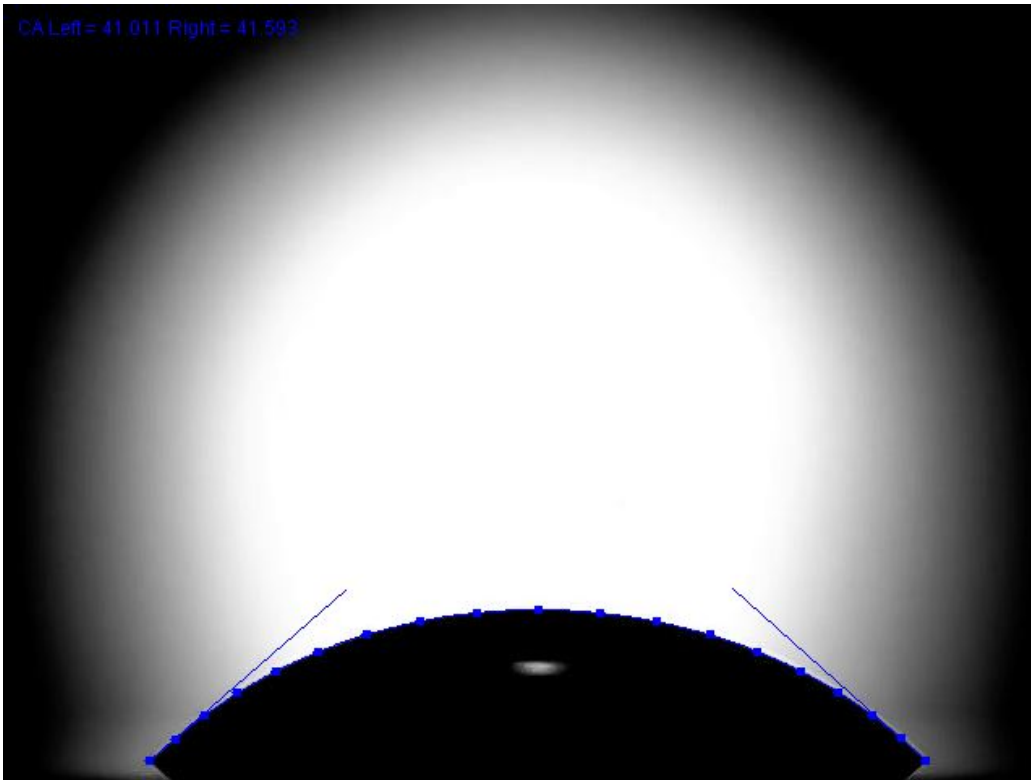
Figure 3.4.5: Contact angle measurement illustrating the DropSnake method. The angles are calculated at both sides as illustrated.

The Low Bond Axisymmetric Drop Shape Analysis (LB-ADSA) plugin uses five variables to manipulate a green Young-Laplace drop shape that is superimposed upon the drop image [47]. Similar to DropSnake this plugin uses the gradient-based edge detection that locates the point of greatest

contrast along the drop edge as illustrated in Figure 3.4.6.

The parameters calculated by this method are b, x, y, h and d, i.e. the droplet width, x- and y position, droplet height and height of droplet reflection, respectively. The parameter c is the liquids capillary constant which allows for accurate gravitational correction of the drop. This last parameter is set to 0 as the low water volume used makes the gravitational effects negligible.
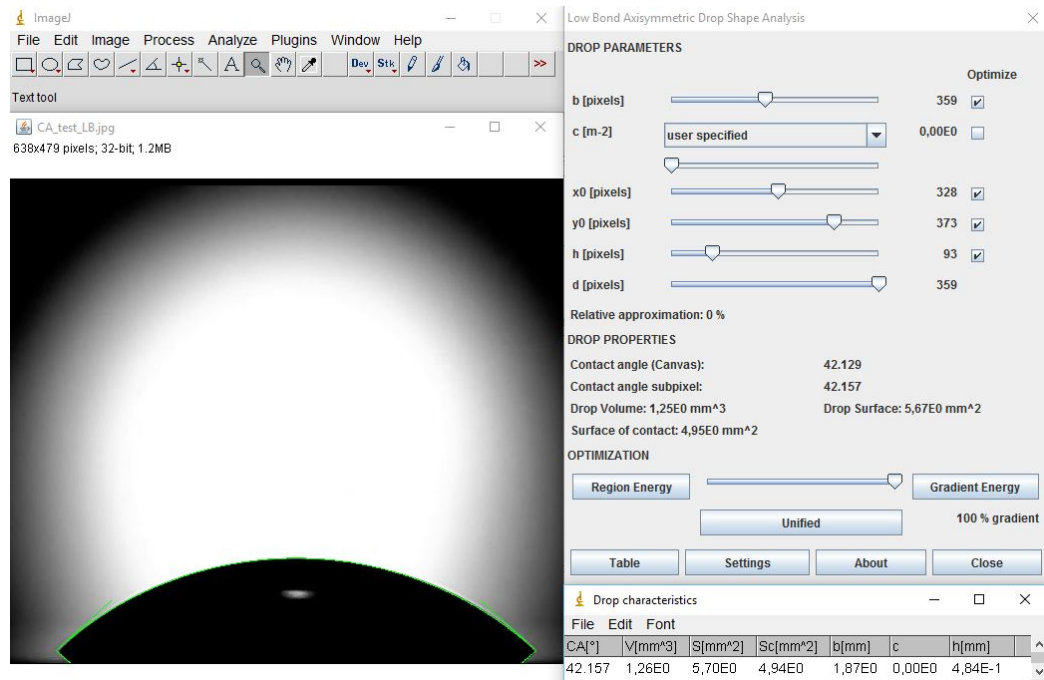
Figure 3.4.6: Contact angle measurement illustrating the LB-ADSA method. A green loop from the gradient detection encloses the drop (left). The dialog box (upper right) contains the parameters which can be adjusted manually to a approximate fit before pressing *Gradient energy*, which fits the curve along the sharp gradient. The resulting contact angle is give in the tabe (bottom right).

The CAM results should be interpreted with caution as the measurement setup is of more primitive nature than those used in the literature. However, all measurements in the literature are performed using different methods and only trends should be compared. When using the two aforementioned methods, a small deviation in the contact angle can be observed. In this project, the average results of these methods were used.

Chapter 4

Geometry Estimation

Matlab was used to calculate and plot single mode conditions based on the chosen wavelength (633 nm) and geometry using the effective index method (EIM). Additionally, a literature study on the effect of geometry dimensions on propagation loss have been conducted.

4.1 Single-mode Conditions

During this relatively short project period, waveguide dimensions achieved by e.g. Prieto et al. [14] are hard to reproduce. Single mode propagation in silicon nitride rib waveguides, with rib width of 4 μm, was processed by managing shallow rib etch of only 4 nm on a 250 nm silicon nitride core layer. Increasing the core thickness, and hence the single mode limit, might be a good starting point in order to achieve single mode waveguides at NTNU NanoLab.

Matlab was used to determine waveguide geometries yielding single-mode conditions based on the effective index method (EIM). The EIM reduces to a simple relation between the transversal sizes of the optical rib waveguide for single-mode propagation [48]

$$t < \frac{r}{\sqrt{1 - r^2}} \tag{4.1}$$

where $t = \frac{w_{eff}}{H_{eff}}$, $r = \frac{h_{eff}}{H_{eff}}$, $h_{eff} = h + q$, $H_{eff} = H + q$, $w_{eff} = w + \frac{2\gamma_c}{k(n_f^2 - n_c^2)^{1/2}}$, $q = \frac{\gamma_c}{k(n_f^2 - n_c^2)^{1/2}} + \frac{\gamma_s}{k(n_f^2 - n_s^2)^{1/2}}$, n_f, n_s and n_c are the refractive indices of the core, substrate and cover layer, respectively as illustrated in Figure 4.1.1. $\gamma_{c,s} = 1$

for TE modes and $(n_{c,s}/n_f)^2$ for TM modes. The Matlab implementation
of (4.1) is given in Appendix C. The calculations using the EIM given by
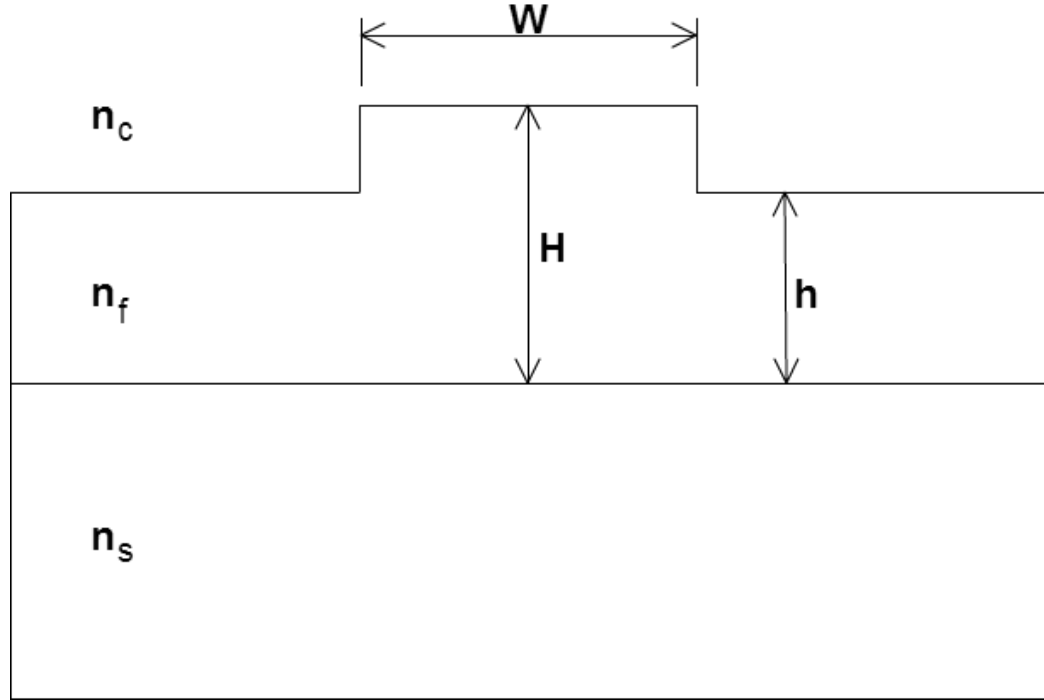
Figure 4.1.1: Sketch illustrating the cross section of a rib waveguide with the
dimensions and materials used in the effective index method. The symbols n_c,
n_f and n_s represent the refractive index of the cover layer, core and substrate,
respectively.

Pogossian et al. [48] is consistent with the findings of Dullo et al. [49].

In order to benefit from the use of rib waveguides, the rib width needs
to exceed that of single-mode strip waveguides, i.e. 350 nm and 630 nm for
wavelengths 532 nm and 780 nm, respectively, as found by Subramanian et
al. [50].

Plots illustrating the relation between rib height and rib width for TE-
and TM-modes for 200 nm and 550 nm core thickness are shown in Figure
4.1.2 and Figure 4.1.3, respectively.

If 200 nm Si_3N_4 is used, extreme good etch control is needed as the rib
height then has to be 4.5 nm or lower for a width of 2 μm and wavelength
633 nm.
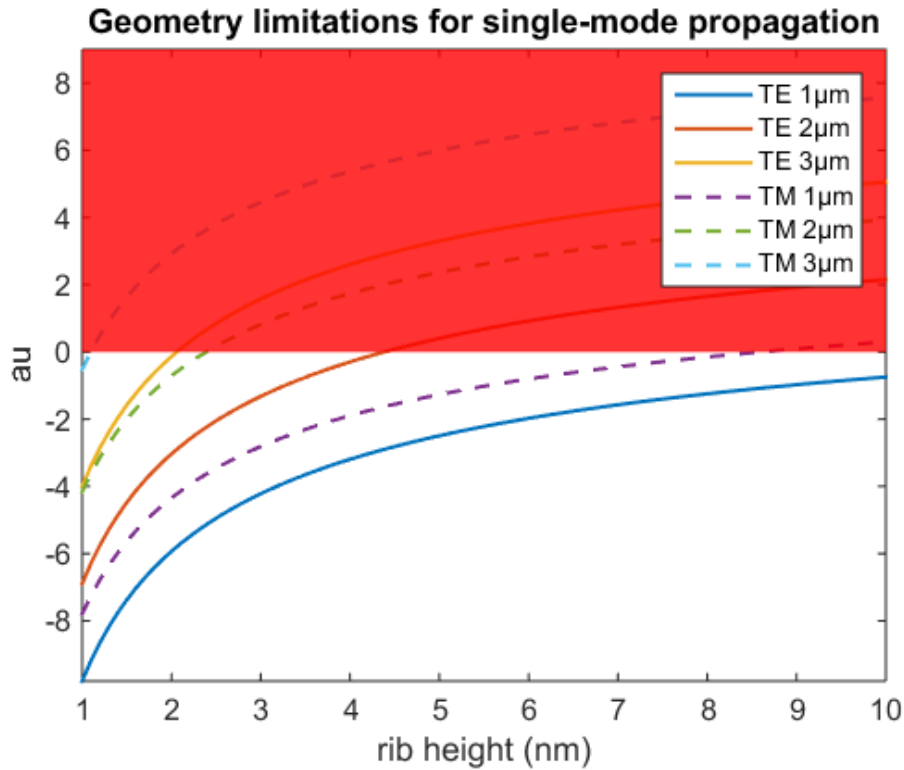
Figure 4.1.2: The plot illustrates the geometrical restrictions yielding single-mode propagation for TE- and TM-modes. The silicon nitride core thickness is 200 nm and rib widths are 1 µm, 2 µm and 3 µm. The red area indicates multi-mode propagation, whereas the white area indicates single-mode propagation.

By increasing the thickness of the Si_3N_4, a deeper etch could still lead to single-mode propagation, as seen in Figure 4.1.3. If a rib width of e.g. 2 µm is desired, a rib etch of 35 nm or lower should suffice.
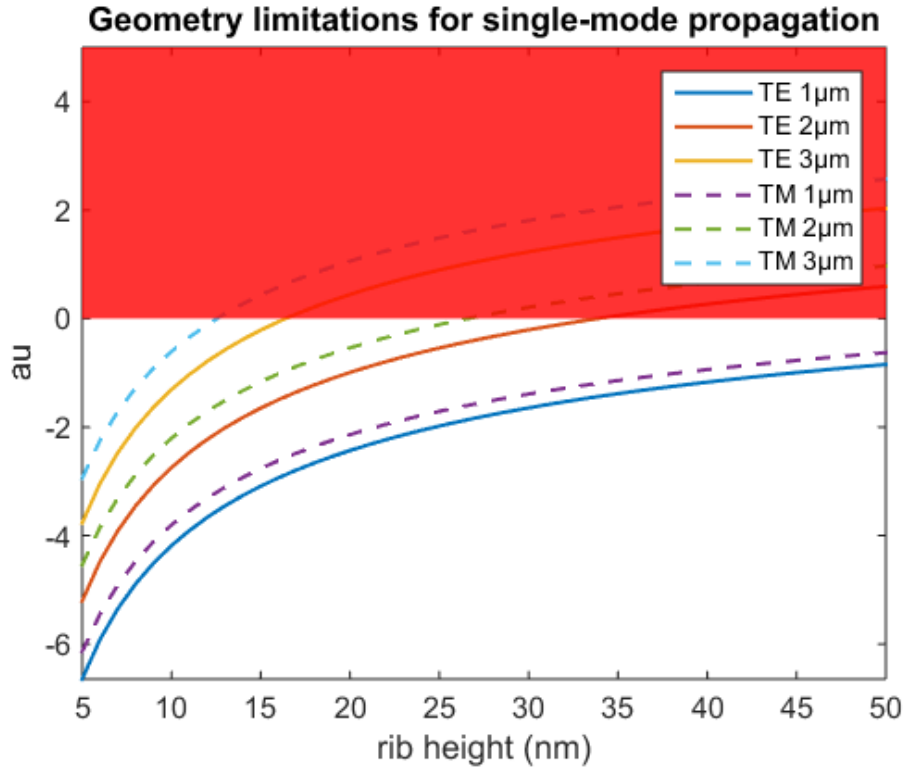
Figure 4.1.3: The plot illustrates the geometrical restrictions yielding single-mode propagation for TE- and TM-modes. The silicon nitride core thickness is 550 nm and rib widths are 1 µm, 2 µm and 3 µm.   The red area indicates multi-mode propagation, whereas the white area indicates single-mode propagation.

4.2   Propagation Loss

Dullo et al. [49] investigated silicon nitride rib waveguides by simulation. The results showed increasing propagation losses with larger rib heights. With very shallow ribs, the mode is confined mostly in the bulk core below the rib and as the rib height increases, the mode is more confined in the rib. Additionally, propagation losses for TM-polarization were found to be dependent on the rib width. This is due to an interference effect for the minority field component that cancels the leakage, as illustrated in Figure 4.2.1.

The influence of core thickness on the bending loss was found to be more complicated, and for a fixed rib height the losses had a maximum for core thickness of 90 nm and 180 nm for TE- and TM-polarization, respectively.
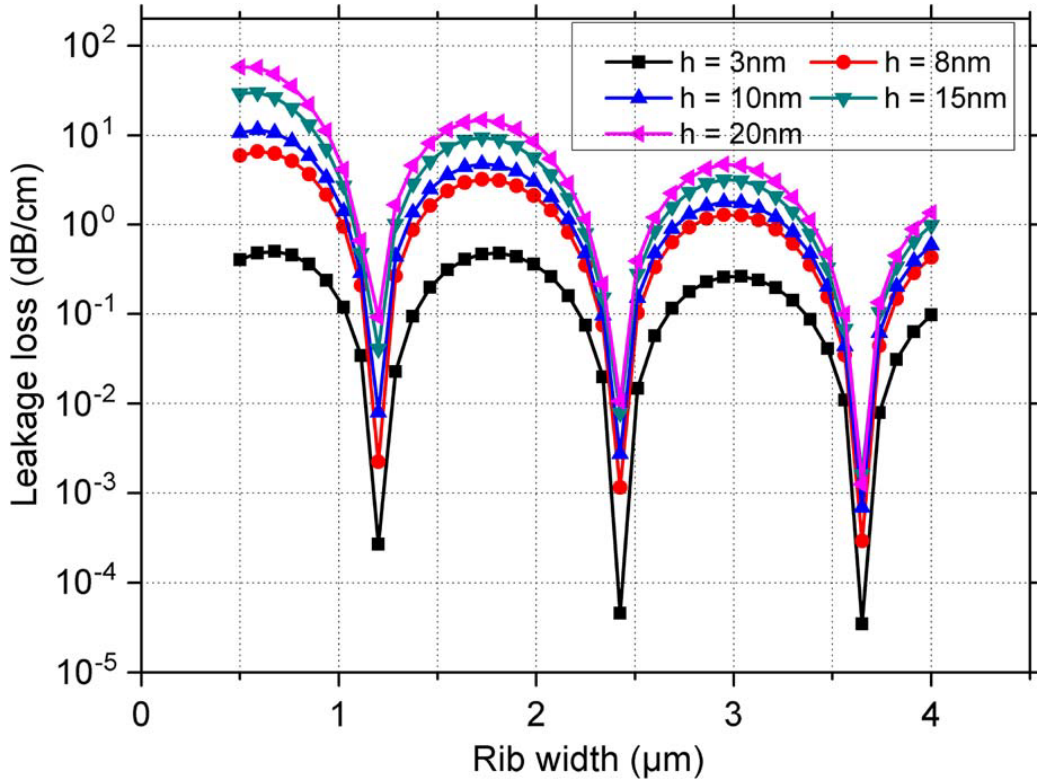
Figure 4.2.1: Plot illustrating propagation loss for TM-modes for different rib widths and heights [49].

By increasing the rib height to the single-mode limit, the bending losses were relatively low. The simulations by Dullo et al. were conducted using wavelength of 785 nm and hence the results of the present project will most likely deviate from these. However, the trends should be similar, making it important to investigate many geometry parameters in order to achieve low-loss waveguides.

4.3   Selected Dimensions

In this project, a core thickness of 550 nm has been selected for the MZI as a starting point based on EIM calculations. Further, based on the same calculations, determining single-mode limits with rib heights from 30 nm to 50 nm for rib widths around 2 μm is found to be a good place to start. Regard-

ing the waveguide bends, large bend radii might be necessary to minimize losses when using shallow rib waveguides. Larger radii result in overall longer waveguides in order to reach the set separation distance between the MZI branches. An initial value of 10 mm has been chosen after studying the work of Prieto et al. [14].

Chapter 5

Processing

The processing of a silicon nitride strip waveguide Mach-Zehnder interferometer (MZI) begins with the investigation of different process parameters.

Utilizing PECVD recipes yielding good deposition control and low surface roughness is important in order to achieve satisfying results regarding the SiO_2 cladding layers and the Si_3N_4 core. Uniform deposition thickness and low surface roughness are critical factors. Investigating etch recipes that enable shallow rib etch with good depth control and anisotropy is crucial in order to meet the requirements for low-loss single mode propagation.

The aforementioned is investigated and discussed in the following sections.

5.1   PECVD Material Deposition

The PECVD recipes used are given in Table 3.2.2 and Table 3.2.3 for the silicon dioxide and silicon nitride, respectively. The deposition rates were measured using the refractometer and verified with the S(T)EM, and the resulting surface roughness was measured using AFM. The results are presented in Table 5.1.1.

As can be seen from the surface roughness measurements for the PECVD SiO_2, the roughness is quite large compared to that of the mono-crystalline Si and the PECVD Si_3N_4, and is consistent with findings by Amirzada et al. [51]. Large surface roughness could lead to optical losses due to scattering effects at the interface between the silicon dioxide cladding and the silicon nitride core. By using thermally grown oxide on the silicon wafer, this problem could be reduced as the surface roughness of thermally grown oxide is

much lower. Other deposition methods could also be investigated, such as E-beam evaporator or ion beam deposition (IBD), although these methods have very low deposition rates compared to PECVD.

Table 5.1.1: PECVD deposition rates for SiO_2 and Si_3N_4.

	Deposition rate	Surface roughness	
Material	(nm/min)	R_a (nm)	R_q (nm)
Si wafer	-	0.17	0.21
SiO_2	88	3.09	3.88
Si_3N_4	15	0.43	0.55

The optical properties of the PECVD Si_3N_4 have not been determined at NTNU NanoLab as the primary use is mechanical applications, e.g. MEMS. Gorin et al. investigated the effect of plasma frequency and NH_3/SiH_4 ratio on optical properties of silicon nitride. Two frequencies were tested, one high frequency (HF), 13.56 MHz and one low frequency (LF), 380 kHz. With NH_3/SiH_4 ratio of 1, the refractive index was found to be approximately 2 and 1.9 by using HF-PECVD and LF-PECVD, respectively. The main difference regarding the two plasma frequencies was found in the transmission measurements yielding very low absorption coefficient for the HF-PECVD whereas approximately $1300\,cm^{-1}$ for the LF-PECVD. However, due to more stability in the refractive index, easier reproducibility of optical waveguides was highlighted for the high-frequency plasma. This, together with the very short propagation distance needed would indicate that the present used HF-PECVD recipe would yield satisfying results.

The PECVD machine had several issues and was out-of-order for a significant time during the project. Testing of different recipes for the Si_3N_4 was not possible due to this.

5.2   ICP-RIE Etch

The etch recipes with parameters given in Table 3.2.5 were tested. The etch was first performed on 550 nm Si_3N_4 on 2 µm SiO_2. The highly isolating sample was not successfully characterized using the S(T)EM due to major charge build-up resulting in only overexposed images. The etch tests were then performed on 220 nm PECVD Si_3N_4 on mono-Si wafer, and the resulting

rates for the two recipes are listed in Table 5.2.1. Running the tests directly on silicon wafers also improves the refractometer accuracy as fewer layers are involved.

Table 5.2.1: ICP-RIE etch rates on silicon nitride and photoresist for the two recipes given in 3.2.5.

Material	ICP-RIE (nm/min)	RIE (nm/min)
Si_3N_4	100	53
CSAR 62	19	21

The ICP-RIE etch has 89 % higher etch rate compared to the RIE etch for Si_3N_4. The selectivity towards the CSAR photoresist is found to be high for both recipes, with values of 5.2:1 and 2.5:1 for the ICP-RIE and RIE etch, respectively.

Low etch rates for silicon nitride are preferred due to the shallow rib needed. The RIE etch seems promising regarding the etch rate, but reveals some more edge roughness compared to the ICP-RIE, as illustrated in Figure 5.2.1. The RIE etch gives a more rounded edge compared to the ICP-RIE. Low EBL exposure dose was used on the sample for the ICP-RIE etch, resulting in some edge roughness probably caused by photoresist residue.
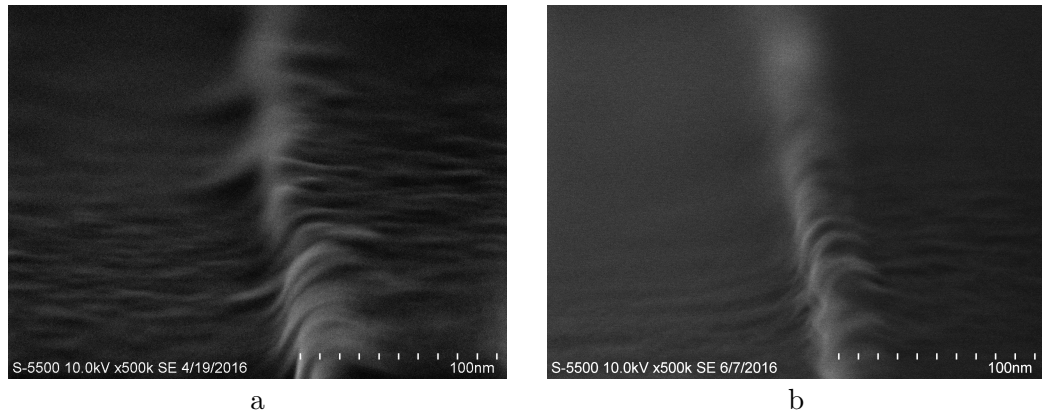
Figure 5.2.1: SEM images illustrating the results of (a) ICP-RIE etch and (b) RIE etch. The ICP-RIE etch is more uniformly etched at the edges where the RIE etch shows a more rounded ridge. However, some roughness is seen at the edge of the ICP-RIE etched rib that may indicate photoresist underdevelopment. The etch depth is approximately 30 nm for both ribs.

5.2.1   Under Developed

The surface roughness is evident in the AFM measurements illustrated as a height profile in Figure 5.2.2 and as a surface plot in Figure 5.2.3.

The etch dose on the left of the profile was $300\,\mu C/cm^2$ and contains unetched regions caused by photoresist residue. To the right of the profile the exposure dose was $600\,\mu C/cm^2$ and hence no photoresist residue. The high area dose was caused by an overlap of lithography masks in CleWin4 resulting in a double exposure of this region. There are no evident signs of overexposure either, as the etched profile has the same width as the mask, i.e. $1\,\mu m$.

Master student Holmen performed dose tests on CSAR 62 using the Elionix EBL revealing that the initial $300\,\mu C/cm^2$ was slightly too low. Increasing the dose to $350\,\mu C/cm^2$ showed promising results without signs of underdevelopment [52].

The ICP-RIE etch recipe requested from Oxford, see Table 3.2.6, was not fully implemented. However, a similar etch recipe with the same gases and ICP power was tested. The etch rate was too high for this purpose, approximately 300 nm/min. The higher etch rate was probably caused by the different CHF_3 gas flow (50 sccm) and ICP power (40 W).
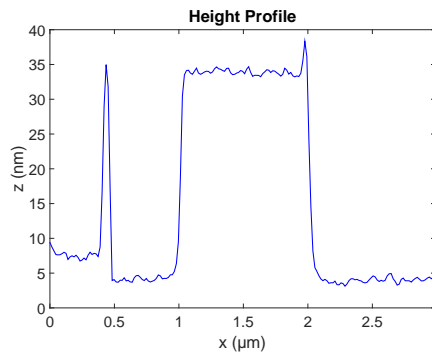
Figure 5.2.2: AFM measurements indicate underdevelopment caused by underexposure. The etched profile to the left of the rib, where the exposure dose was $300\,\mu C/cm^2$, contains unetched regions caused by photoresist residue. To the right of the rib the exposure dose was $600\,\mu C/cm^2$ and hence no photoresist residue.
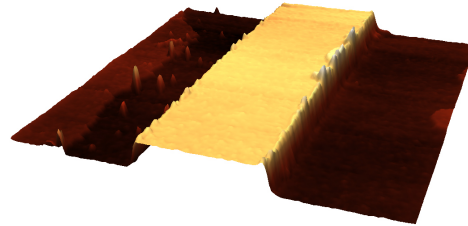
Figure 5.2.3: The AFM image illustrates the results of underdevelopement causing high surface roughness. Left hand side of the rib: exposure dose $300\,\mu C/cm^2$ with resulting unetched spots. Right hand side of the rib: $600\,\mu C/cm^2$ resulting in uniform etch. The rib height is $30\,nm$.

5.2.2 Over-etched

A mistake was made in the etch setup, interpreting seconds as minutes in the software, resulting in 60 times longer etch than intended. The intension was to etch approximately $50\,nm$ in the Si_3N_4 ending up etching far into the $2\,\mu m$ SiO_2. The result from SEM imaging is illustrated in Figure 5.2.4.

Considering the extensive etch time and the fact that no photoresist was left, the RIE etch used is highly anisotropic. The etch depth ended up at being approximately $320\,nm$.
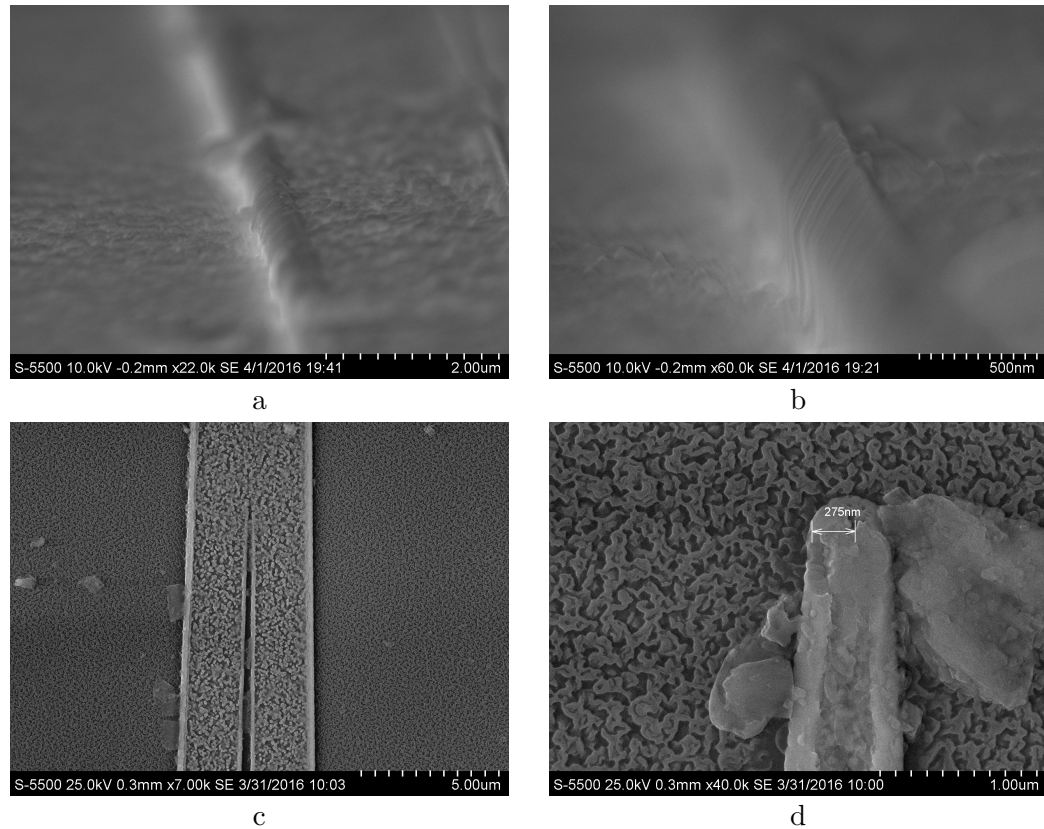
Figure 5.2.4: SEM images illustrating the results of etching 60 times longer, i.e. 16 min instead of 16 s. The Si_3N_4 is totally removed and the structures are all in the SiO_2 layer. (a) and (b) rib edge at different magnifications; (c) top view of MZI waveguide splitter; (d) close-up of waveguide splitter in (c).

5.2.3   Deep Etch

In order to investigate the edge roughness of the silicon nitride etch, 220 nm Si_3N_4 on Si was etched through using both recipes, yielding higher contrast on the SEM compared to a shallow etch due to the now exposed silicon and hence less charge build-up.

   The ICP-RIE etch, described in Table 5.2.1, gave the results illustrated in Figure 5.2.5. The SEM images reveal a tendency towards conic shape of the strip waveguide, resulting from slightly faster polymerization of the sidewalls compared to the sputtering rate. However, the edge roughness is quite low and for the purpose of the project, i.e. shallow rib etch, the conic shape will

probably have little to no impact on light propagation.

No investigation of the actual width of photoresist mask after development has been performed in this project. Over-development or over-exposure of the photoresist causes the structure width to decrease as more resist is removed when developed.

a

b

c

d
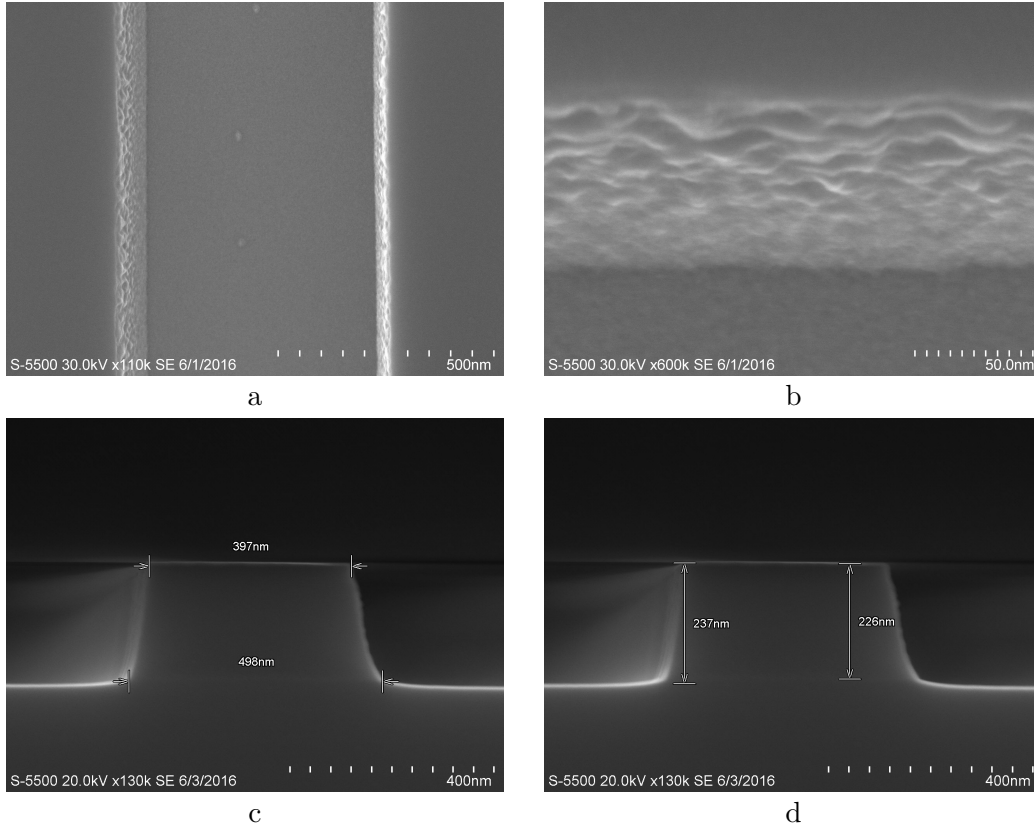
Figure 5.2.5: SEM images of 220 nm Si_3N_4 ICP-RIE etch-through illustrating (a) top-view; (b) edge roughness; (c) and (d) cross-section images with width and height labels, respectively. The width of the photoresist mask was 500 nm.

The RIE etch, described in Table 5.2.1, gave the results illustrated in Figure 5.2.6. The SEM images reveal more edge roughness from the RIE etch compared to that of the ICP-RIE etch. The RIE etch is slightly more uniform, i.e. the strip waveguide structure has less tendency of conic shape when observing the cross section.

A comparison of the wall roughness is seen in Figure 5.2.7. The side-wall
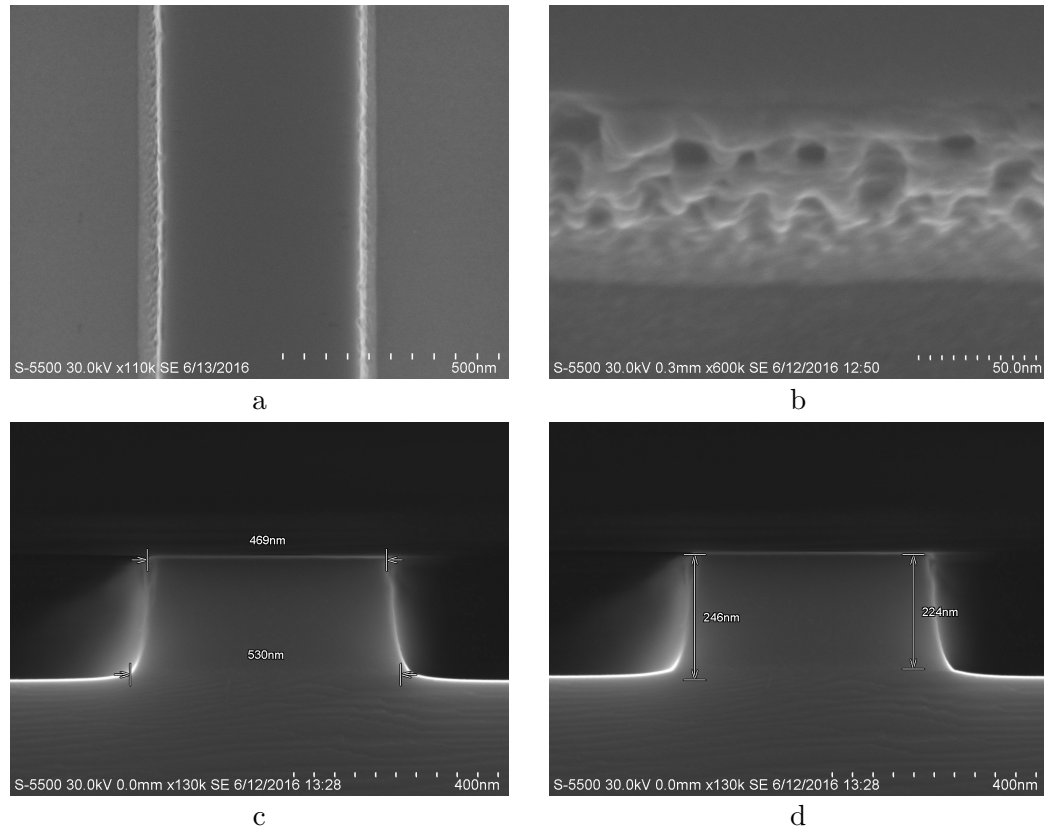
Figure 5.2.6: SEM images of 220 nm Si_3N_4 RIE etch-through illustrating (a) top-view; (b) edge roughness; (c) and (d) cross-section images with width and height labels, respectively. The width of the photoresist mask was 500 nm.

average roughness is approximately 5 nm from the ICP-RIE etch and around 8 nm for the RIE etch. Due to the extensive edge roughness, the RIE etch is less promising for deep etched, strip waveguides compared to the ICP-RIE. The roughness is largest where the Si_3N_4 have been subjected to the reactive etch for the longest time, hence the roughness is less evident at the edge bottom for both recipes which is promising for shallow rib etch.
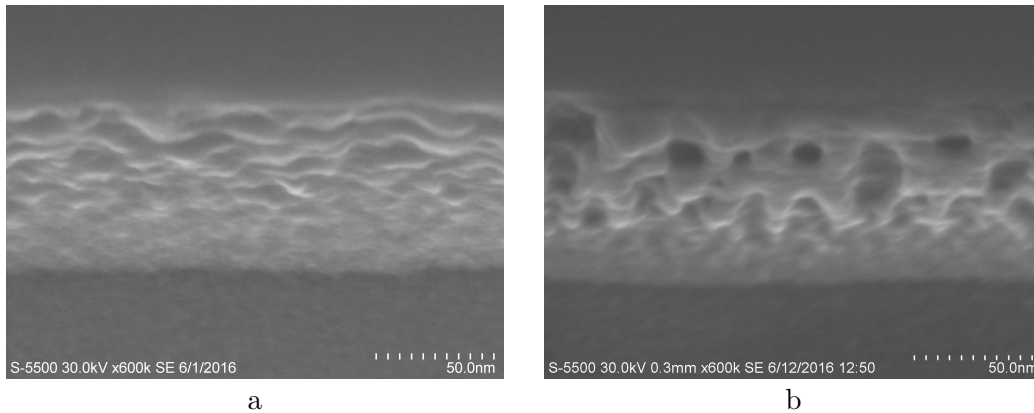
Figure 5.2.7: SEM images of Si_3N_4 edge roughness illustrating (a) ICP-RIE etch; (b) RIE etch.

5.3 Summary

Silicon dioxide was deposited using a well established recipe. The resulting average roughness was found to be 3.1 nm which is high compared to thermally grown oxide. Silicon nitride was deposited using high-frequency plasma resulting in a deposition rate of 15 nm/min and average roughness of 0.4 nm.

Etch tests were performed on 220 nm Si_3N_4 on mono-Si, resulting in good SEM images. The edge roughness is difficult to measure quantitatively. However, the ICP-RIE etch was found to yield less edge roughness compared to the RIE etch. The etch rates were found to be 100 nm/min and 53 nm/min for the ICP-RIE and RIE etch, respectively. This makes the RIE etch more suitable for shallow etches as the etch time increases. Short etch times (few seconds) may give results with low reproducibility due to unstable plasma at the etch initiation. 30 nm rib waveguides were successfully processed with both recipes.

Chapter 6

Biofunctionalization

Some methods of biofunctionalization are investigated with the purpose of gaining a fundamental understanding of this complex and challenging part of the biosensor system.

Organo-silane (APTES) is used to achieve surface amine groups on which antibodies, activated with carbodiimide crosslinker (EDC) chemistry, can be covalently immobilized by amide linkage.

The following presents results from the surface silanization and the immobilization of catcher antibodies. All processes are characterized, using different methods, in order to investigate and verify changes after each process step.

6.1 Silanization

The silanization was conducted using two different approaches, i.e. liquid phase (LP) and vapor phase (VP) deposition. The protocols are described in-detail in 3.3.3. Most silanization protocols in the literature include use of nitrogen glove boxes that provides a humid-free environment. The glove boxes at NTNU NanoLab were unfortunately out of order at the time, hence all silanization was performed at 26 % humidity.

For LP silanization, the concentration of APTES used, i.e. 2 %, was chosen due to findings of Thakurta et al. [31] showing that 2 % (v/v) APTES gave a higher density of NH_2 moieties compared to 5 % concentration, and that the surface density of immobilized IgG was shown to correlate with the availability of terminal NH_2 groups.

Characterization was performed using contact angle measurements (CAM) and atomic force microscopy (AFM) with the results given in Table 6.1.1. LP silanization both with and without pH regulation using acetic acid was performed with no significant difference in the contact angle measurements.

Table 6.1.1: Tabulated silanization results from CAM and AFM.

Silicon nitride	Contact angle (° ± SD)	Surface roughness R_a (nm)	R_q (nm)
Si_3N_4 reference	46.7 ± 3.2	0.43 ± 0.04	0.55 ± 0.06
1 min LP	40.8 ± 0.6	0.36 ± 0.06	0.47 ± 0.09
5 min LP	41.7 ± 1.9	0.35 ± 0.06	0.46 ± 0.08
15 min LP	44.7 ± 2.2	0.39 ± 0.07	0.50 ± 0.10
4 h VP	57.7 ± 1.7	0.43 ± 0.06	0.54 ± 0.08
Silicon			
Si reference	44.1 ± 0.8	0.17 ± 0.02	0.21 ± 0.03
1 min LP	41.4 ± 0.5	0.22 ± 0.04	0.29 ± 0.07
15 min LP	51.7 ± 0.1	0.22 ± 0.04	0.31 ± 0.09
5 h VP	80.0 ± 0.2	0.22 ± 0.02	0.28 ± 0.03

Silanization of Silicon Nitride

The results from the silanization performed on silicon nitride are shown in Figure 6.1.1 and illustrate the difference in hydrophilicity obtained from different silanization protocols. A clean, untreated silicon nitride sample is included as reference at each measurement. The results from the O_2 plasma treatment are omitted due to the unmeasurable low contact angle, $<10°$.

The contact angle decreased from 46.7 ± 3.2 to $<10°$ after plasma oxidation, indicating increased surface hydrophilicity and good wettability. This is consistent with a high surface density of silanol groups [53].

The results show trends indicating a positive correlation between silanization time and CA, with VP silanization yielding the most hydrophobic surface. All LP silanization times in this experiment resulted in more hydrophilic surfaces compared to clean silicon nitride. However, longer reaction times can lead to less hydrophilic surfaces, as shown by e.g. Diao et al. [53]. The increase in hydrophobicity is likely to be due to the amine groups and
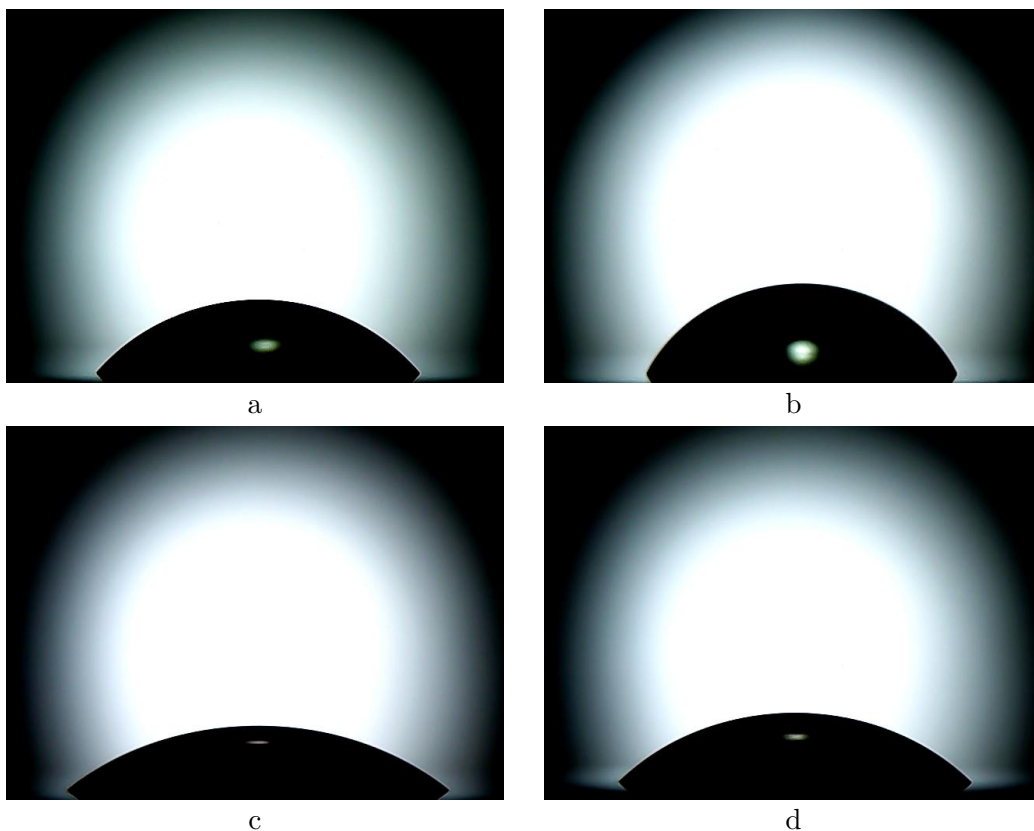
Figure 6.1.1: Contact angle measurement results of aminosilane on silicon surfaces. (a) Initial silicon nitride surface for reference (51.1 ± 0.7)°; (b) 4 h vapor phase (VP) APTES deposition (57.7 ± 0.1)°; (c) 1 min liquid phase (LP) APTES deposition (38.3 ± 2.9)°; (d) 15 min LP APTES deposition (43.1 ± 1.5)°.

the carbon backbone of APTES, which both are more hydrophobic than the silanol groups formed after oxygen plasma treatment.

Figure 6.1.2 shows the AFM height measurements of the same samples. The AFM images reveal an issue regarding the surface roughness of the PECVD silicon nitride. Even though the surface roughness of the silicon nitride surface is low, it competes with the roughness formed by the aminosilane clusters. However, a trend indicating decrease in surface roughness after silanization is seen. This could be due to aminosilane cluster formation in valleys of the initial silicon nitride surface, lowering the average and RMS roughness. Additionally, a trend indicating slight increase in surface rough-

ness for longer reaction times is seen, consistent with findings of Thakurta et al. [31].
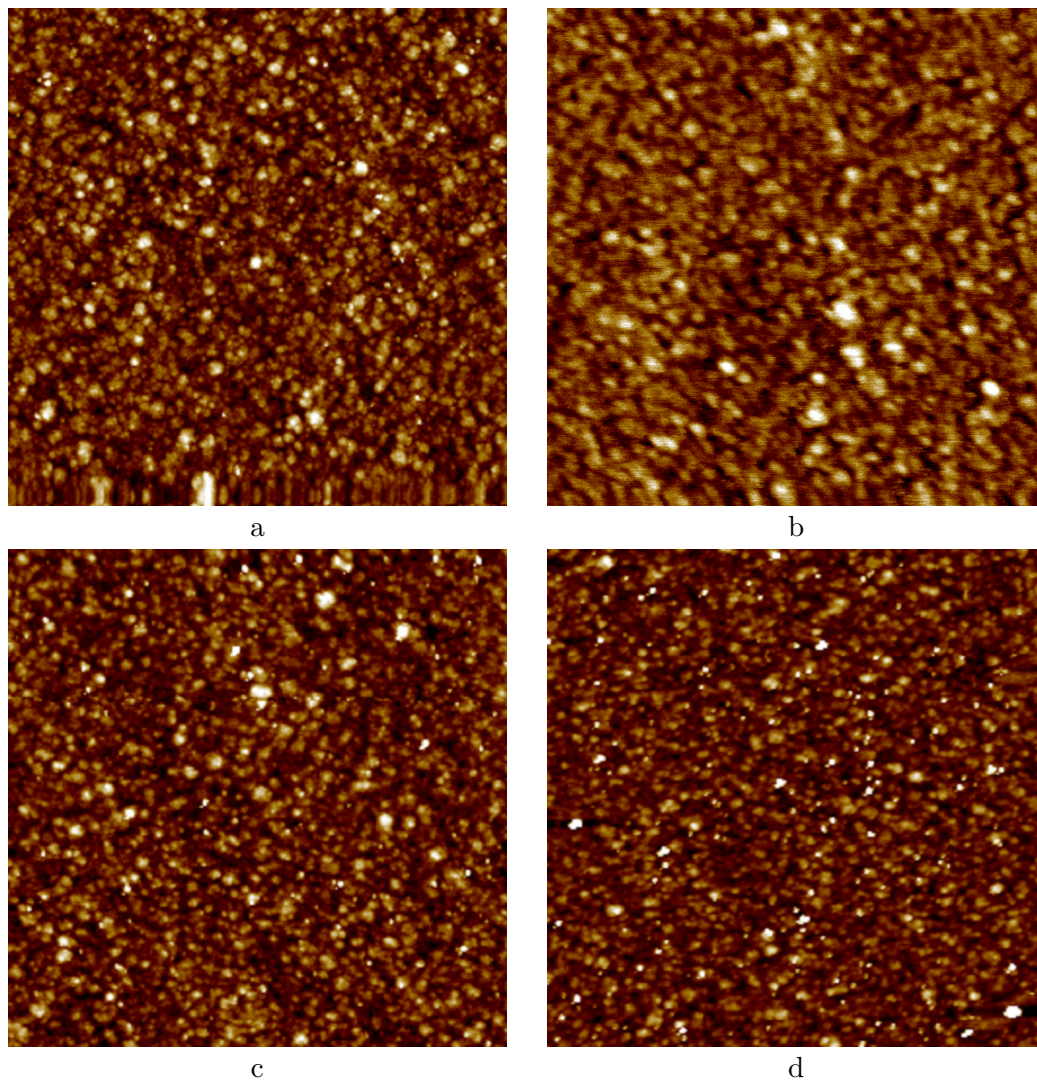
Figure 6.1.2: AFM scans of a 1 µm×1 µm area on the aminosilane on silicon nitride surfaces. (a) Initial silicon nitride surface for reference; (b) 4 h vapor phase (VP) APTES deposition; (c) 1 min liquid phase (LP) APTES deposition; (d) 15 min LP APTES deposition.

Silanization of Silicon

In order to circumvent the surface roughness challenge, mono-crystalline silicon wafer dies were treated equally as the ones coated with silicon nitride. After the deposition of APTES, the silicon samples were characterized using CAM and AFM with the results illustrated in Figure 6.1.3 and Figure 6.1.4, and summarized in Table 6.1.1. Compared to the results for the sili-
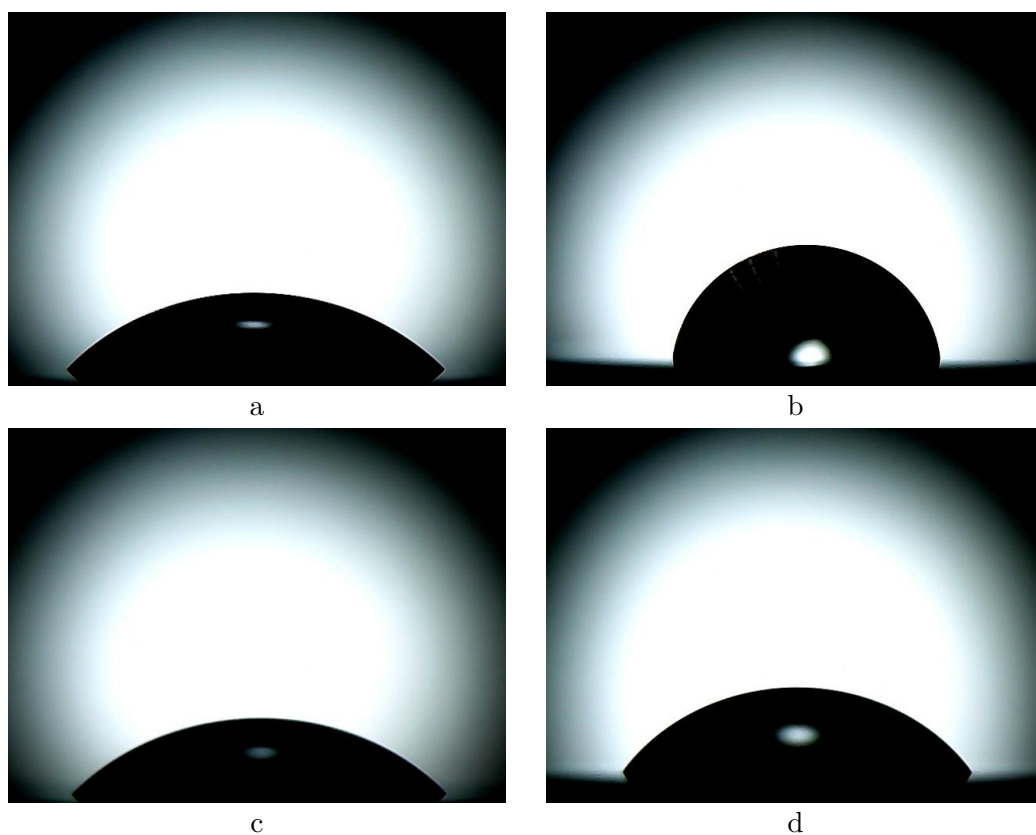
Figure 6.1.3: Contact angle measurement results of aminosilane on silicon surfaces. (a) Initial monocrystalline silicon surface for reference $(44.1 \pm 0.8)°$; (b) 5 h vapor phase (VP) APTES deposition $(80.0 \pm 0.2)°$; (c) 1 min liquid phase (LP) APTES deposition $(41.4 \pm 0.5)°$; (d) 15 min LP APTES deposition $(51.7 \pm 0.1)°$.

con nitride, the mono-crystalline silicon is more hydrophilic, but apart from this the trends are similar. The hydrophobicity is proportional with the LP deposition time, and the VP deposition results in a relatively hydrophobic surface.

From the AFM images, Figure 6.1.4, it is evident that the surface rough-
ness of the mono-crystalline silicon is sufficiently low to locate the aminosilane
clusters, clearly seen in Figure 6.1.4 (b), (c) and (d). VP silanization resulted

Figure 6.1.4: AFM scans of a $500\,\mathrm{nm}\times500\,\mathrm{nm}$ area on the aminosilane on silicon
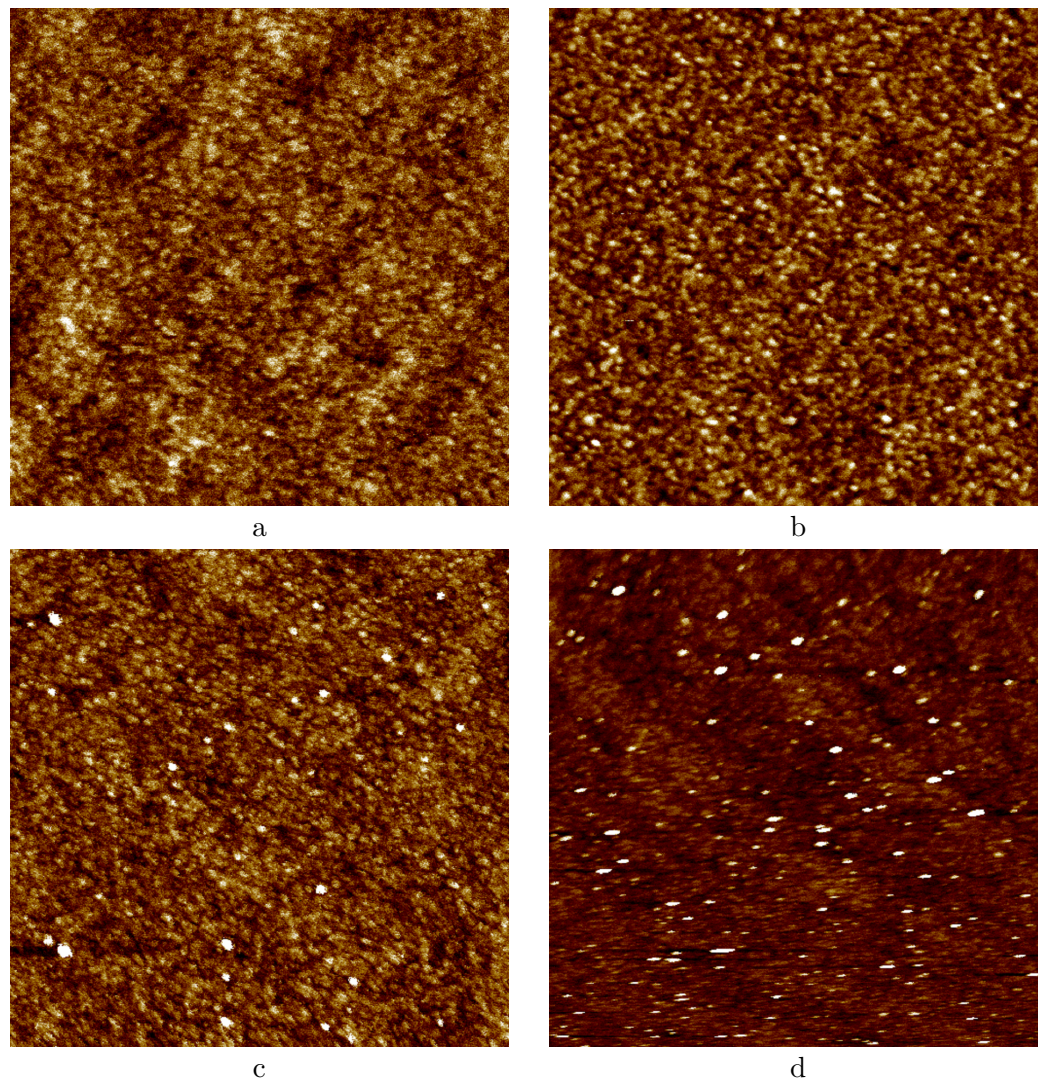surfaces. (a) Initial monocrystalline silicon surface for reference; (b) $5\,\mathrm{h}$ vapor
phase (VP) APTES deposition; (c) $1\,\mathrm{min}$ liquid phase (LP) APTES deposition;
(d) $15\,\mathrm{min}$ LP APTES deposition.

in uniform aminosilane clusters closely packed on the surface with heights and

widths of approximately $2\,\mathrm{nm}$ and $3\,\mathrm{nm}$, respectively. Long time LP silanization resulted in larger and more spread agglomerates with heights and widths of, approximately $2\,\mathrm{nm}$ to $5\,\mathrm{nm}$ and $5\,\mathrm{nm}$ to $15\,\mathrm{nm}$, respectively. However, fewer polymeric structures are observed in the LP deposition, supporting that pre-hydrolysis does stabilize hydrolyzed APTES monomers, which are subsequently deposited on the surface. For VP deposition, the condensed APTES results in more agglomerates. Yadav et al. [54] showed that VP silanization gave a more uniform aminosilane layer compared to the aqueous LP silanization, and that both methods resulted in a little less than a monolayer thickness of aminosilane between the clusters.

Extending the time of the LP silanization could lead to visible cluster formations on silicon nitride, and increasing the APTES concentration could lead to a more densely silanized surface, as shown by Terracciano et al. [55]. This was omitted in this project due to time limitations.

The stability of the aminosilane in aqueous environments is important as most biosensor applications depend on analytes in aqueous buffer solutions. The stability of APTES deposition is not included in this study, but comprehensive evaluations are carried out by Zhu et al. [56] revealing that monolayer aminosilane layers, i.e. $7\,\mathrm{nm}$ [57], reduced to $3\,\mathrm{nm}$ after $24\,\mathrm{h}$ hydrolysis in $40\,^{\circ}\mathrm{C}$ water. This indicates that sensor functionalization needs to be performed shortly after silanization, and that the storage is sensitive to ambient humidity.

The use of VP silanization is beneficial in that the necessary amount of aminosilane is lower than that used in LP silanization. Additionally, in VP silanization, no other chemicals are used which makes this method environmentally favorable.

Stine et al. [58] showed that it is possible to achieve primary amines on silicon nitride surfaces by using only oxygen plasma in humid air. This method is unavailable at the NTNU NanoLab but could potentially eliminate the need for aminosilanes.

6.2 Catcher Immobilization

Immobilization of the anti-mouse IgG catcher antibodies was performed using two different approaches, as described in 3.3.4, and several crosslinker concentrations and incubation times.

The concentrations of the primary antibody and the fluorescent conjugate

antibody were kept constant during the entire experiment, limiting adjustable parameters. Uniformly distributed primary antibodies resulting in a uniform fluorescence, together with minimal non-specific binding was the main goal of this experiment.

Method I was first tested using three different EDC concentrations and constant incubation time in order to investigate the effect of crosslinker concentration on the immobilization process. Later on, method II was investigated on identically prepared samples.

Functionalization of silicon surfaces was also tried in the same experiment, resulting in difficult fluorescence read-out probably caused by fluorescence quenching effect of the silicon [59, 60] and is omitted in this report.

Crosslinker Concentrations

The first functionalization was performed using the two lowest EDC/NHS concentrations described in 3.3.4 and method I. Limitations regarding the result were caused by delay in use of the fluorescent microscope. A confocal microscope was borrowed for the image analysis, but almost no fluorescence was found, illustrated in Figure 6.2.1. The lack of fluorescence could be a

a   b
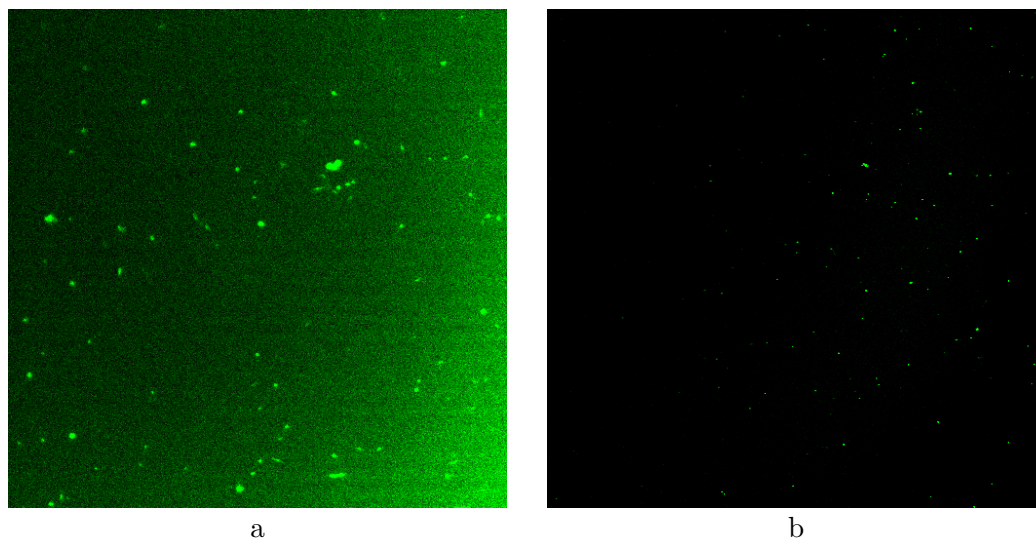
Figure 6.2.1: Fluorescence microscopy images of a $3\,\mu m \times 3\,\mu m$ area. The fluorescence is non-uniform and located in separated clusters. (a) Initial image before background filtering; (b) Image after background filtering.

result of the delay in which the samples were stored immersed in PBS buffer for more than 24 h after the fluorescent conjugates were added. Hydrolysis of the aminosilane may be a reason in addition to light exposure, reducing the fluorescence intensity of the conjugated labels.

Functionalization using the two highest EDC/NHS chemistries described in 3.3.4, resulted in mixed results, some which were dominated by aggregation of antibodies as illustrated in Figure 6.2.2. Aggregates are formed by adducts, i.e. the result of a chemical reaction where two or more molecules are added together forming a new, larger molecule. High EDC concentration resulted in a higher number of large clusters compared to the low EDC concentration. Additionally, the VP silanization resulted in a more uniform fluorescence when low EDC is used.

High concentration of primary Ab could generate clusters which later could bind to a high number of secondary Ab, increasing the fluorescence intensity at the site. Rapid centrifuging the Ab and using only the supernatant could minimize the amount of aggregate. The drawback of centrifuging is that the resulting concentration is unknown, and one could risk wasting an entire batch of antibodies.

Incubating the primary Ab together with the EDC/NHS could lead to protein cross-binding, a binding event between the antibody carboxyl groups and amino groups that are activated and conjugated by the NHS esters. Omitting the incubation step for the EDC/NHS/Ab solution by first applying the EDC/NHS solution to the aminosilanized surface and incubating prior to the addition or primary Ab could minimize the Ab-Ab conjugation prior to and during the desired binding event.

In the third experiment, two concentrations of EDC and NHS were tested using two different approaches (I and II) as described in 3.3.4. The results from the third experiment are shown in Figures 6.2.3-6.2.5.

The results of the two methods are most evident with the 15 min silanization in Figure 6.2.4 where the differences are clearly visible. Although method Ia (6.2.4(Ia)) shows less cluster formations, the fluorescence is slightly more uniform in Ib (6.2.4(Ib)) hence Ib is used as the basis for the next experiment.

Incubation Times

Method I was further used with EDC and NHS concentrations of 2.5 mg/mL and 6.0 mg/mL, respectively, investigating the effect of incubation times on the aggregate formations and fluorescence uniformity.
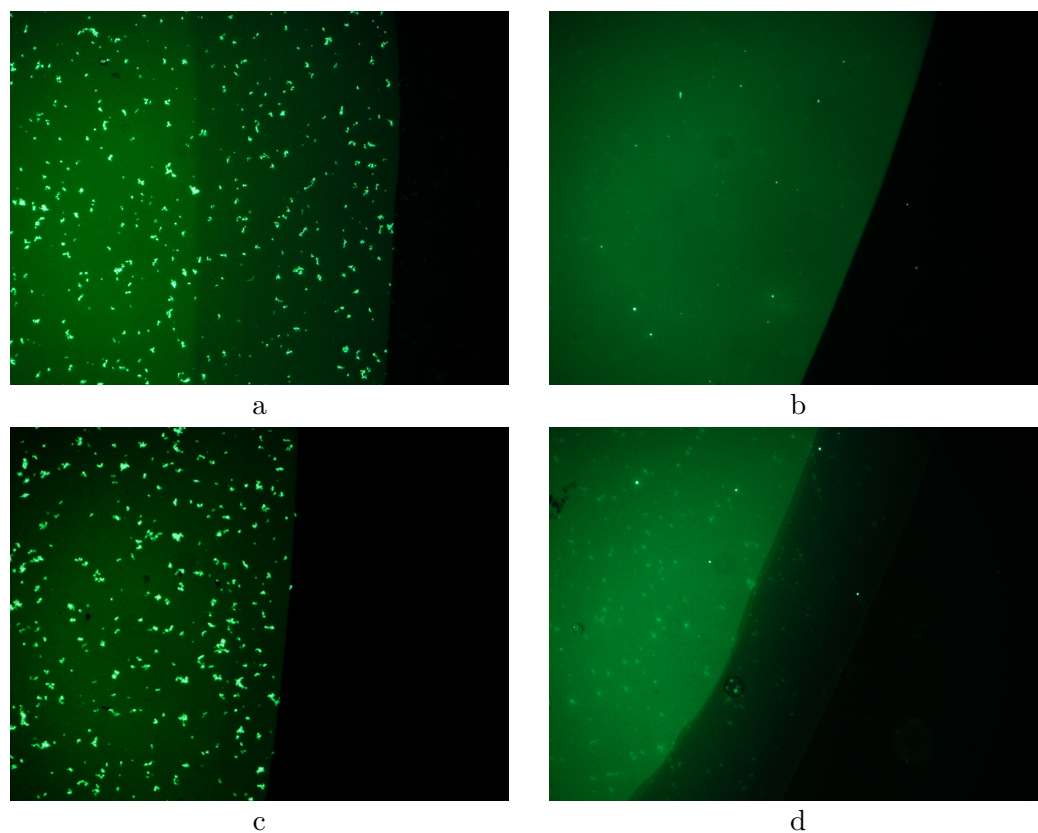
Figure 6.2.2: Fluorescence microscopy images of functionalized surfaces where Alexa Fluor® 488 antibody (Ab) conjugate has bonded to the primary antibodies. (a) 5 h vapor phase (VP), 50 mM EDC; (b) 5 hour VP silanization, 100-fold molar excess of EDC over primary Ab (65 µM); (c) 15 min liquid phase (LP) silanization, 50 mM EDC; (d) 15 min LP silanization, 100-fold molar excess of EDC over primary Ab (65 µM). The aggregates resulting in sharp fluorescent clusters are clearly visible where high EDC concentration have been used and less present at lower EDC concentration.

The samples used were LP silanized for 15 min. The EDC/NHS/anti-IgG solution was incubated for 15 min at RT before applied on six batches of silanized surfaces and incubated for 1 min, 5 min, 15 min and 30 min, 1 h, 2 h and 5 h, respectively. Some of the results are illustrated in Figure 6.2.6. Less aggregate formation is evident overall since also the 2 h incubation time shows less amount of fluorescent clusters compared to last time. This could be due

Ia   IIa

Ib   IIb

Figure 6.2.3: Fluorescence microscopy images of the 1 min LP amino-silanized surfaces functionalized using method I and II with two different EDC and NHS concentrations. (I) and (II) indicate method I and II, respectively; (a) and (b) indicate the respective concentrations of EDC: 0.25 mg/mL and 2.5 mg/mL, and NHS: 0.60 mg/mL and 6.0 mg/mL.

to the sonication of the diluted antibody solutions, proposed by professor in nanomedicine at NTNU, Øyvind Halaas. The solutions were immersed in ultrasonic bath for approximately 10 s in order to see whether this had an effect on the aggregates. However, a trend indicating increased cluster formation with longer incubation is seen. Assuming covalent binding, the binding strength should be equal for all incubation times such that 1 min is sufficient. This will probably depend upon antibody concentration as it will take some time to get full surface coverage with very low concentrations.

Figure 6.2.4: Fluorescence microscopy images of the 15 min LP amino-silanized surfaces functionalized using method I and II with two different EDC and NHS concentrations. (I) and (II) indicate method I and II, respectively; (a) and (b) indicate the respective concentrations of EDC: 0.25 mg/mL and 2.5 mg/mL, and NHS: 0.60 mg/mL and 6.0 mg/mL.

Non-Specific Binding

A droplet of mouse IgG Alexa Fluor® (5 µg/mL) was applied on a silanized surface and incubated for 30 min at RT. The result is illustrated in Figure 6.2.7(a), together with an illustration of reflection artifacts discovered outside the area with fluorescent antibodies applied. It is evident that there is no non-specific binding reaction between the silanized surface and the mouse IgG conjugate. The apparently fluorescent edge may be caused by either adhesion of fluorescent antibodies when the droplet edge dries, or fluorescence from crystallized PBS buffer. The PBS buffer consists of salts that form crystals
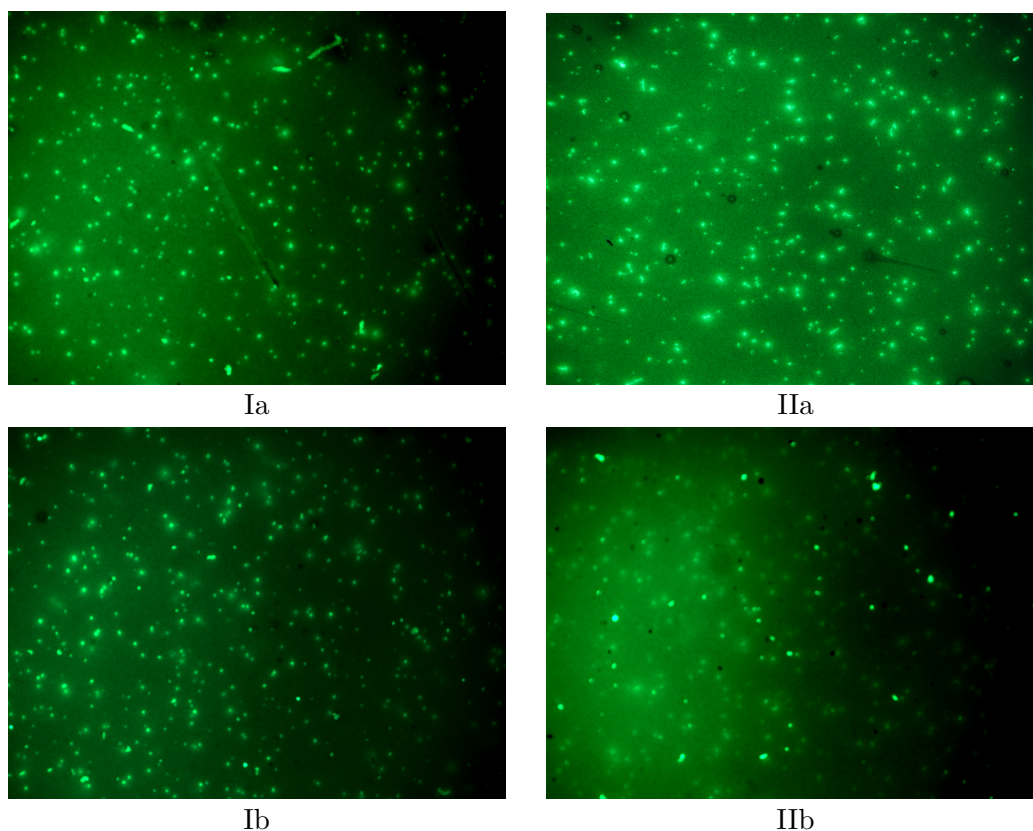
Ia

IIa

Ib

IIb
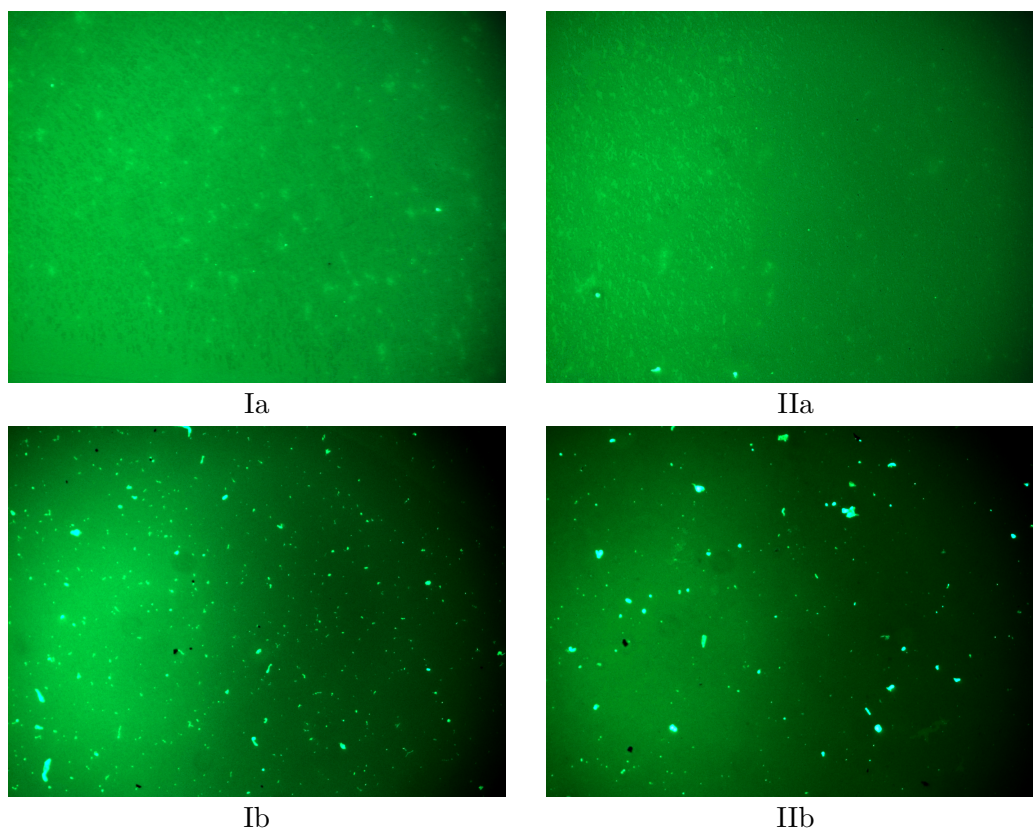
Figure 6.2.5: Fluorescence microscopy images of the 5 h VP amino-silanized surfaces functionalized using method I and II with two different EDC and NHS concentrations. (I) and (II) indicate method I and II, respectively; (a) and (b) indicate the respective concentrations of EDC: 0.25 mg/mL and 2.5 mg/mL, and NHS: 0.60 mg/mL and 6.0 mg/mL.

when dried. These crystals can be difficult to dissolve rapidly, and can trap fluorescent antibodies. Characterizing the fluorescence closer to the droplet center circumvents this problem.

Large clusters are shown possible to remove by aqueous sonication as illustrated in Figure 6.2.8. The samples were immersed in 20 °C DIW and sonicated for 1 min. The resulting surface was free from fluorescent clusters, but contained bare areas where the clusters had been. This indicates that the amount of aggregate formation needs to be controlled prior to the cleaning as the areas without adsorbed antibodies are of no use.

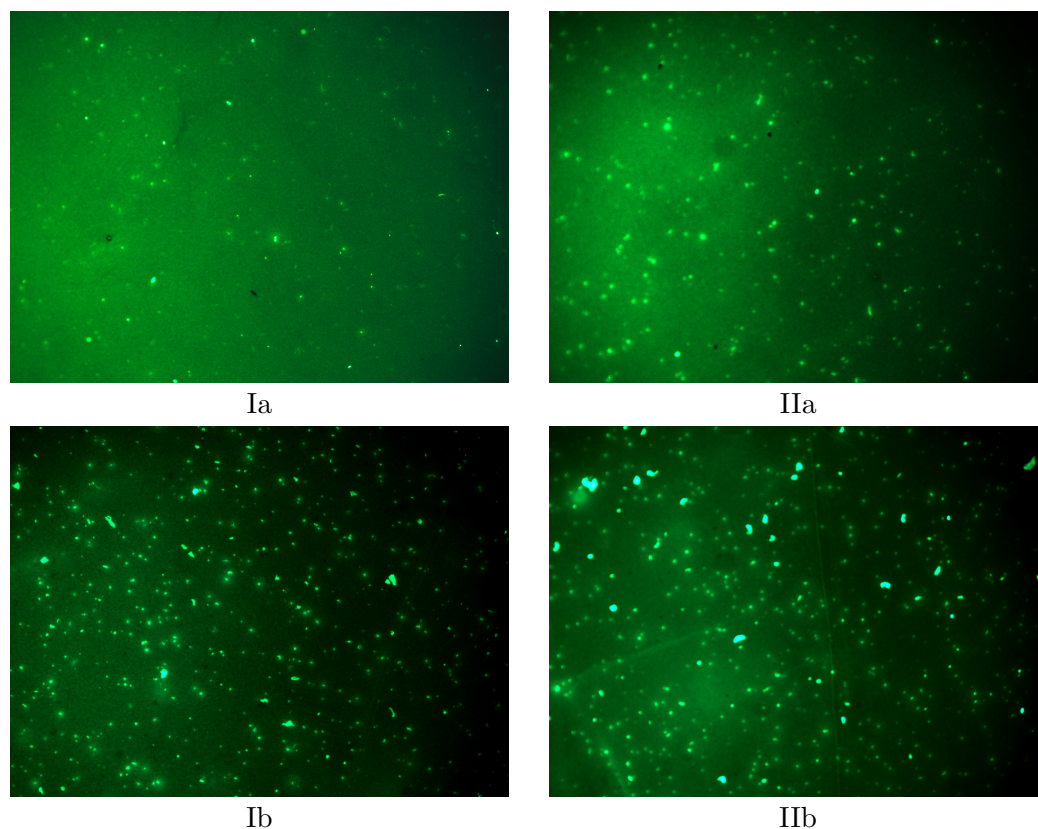|	
1 min	30 min
2 h	5 h
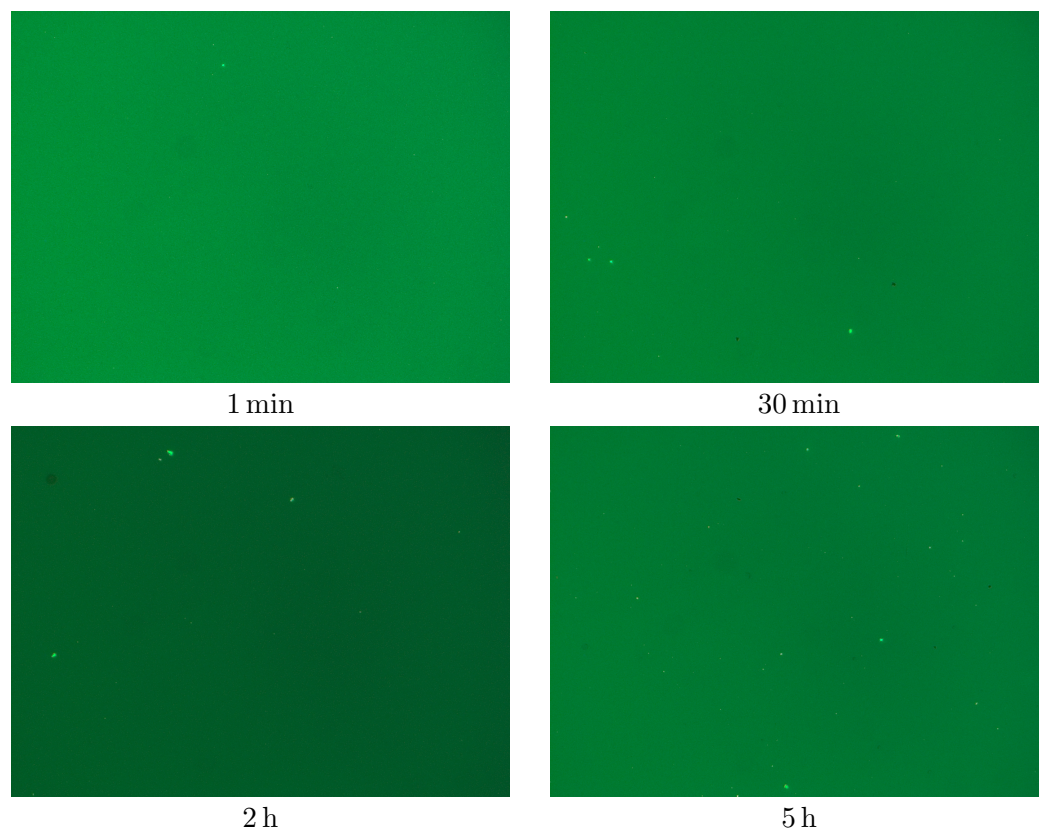
Figure 6.2.6: Fluorescence microscopy images of the 15 min LP amino-silanized surfaces functionalized using method I and EDC and NHS concentrations of 2.5 mg/mL and 6.0 mg/mL, respectively. The different incubation times are given below their respective image.

Surface Wettability

Samples biofunctionalized using 15 min LP silanization and method I for catcher immobilization were tested using CAM. The results are illustrated in Table 6.2.1 along with reference measurements.

The IgG functionalized surface is slightly more hydrophilic compared to the silanized surface but the difference is not significant, leaving this as a non-suitable method for immobilization characterization with the used equipment. Measuring CA after catcher immobilization is not common in the literature. The relatively hydrophilic surface makes for good wettability and hence easy coverage of analyte solution.
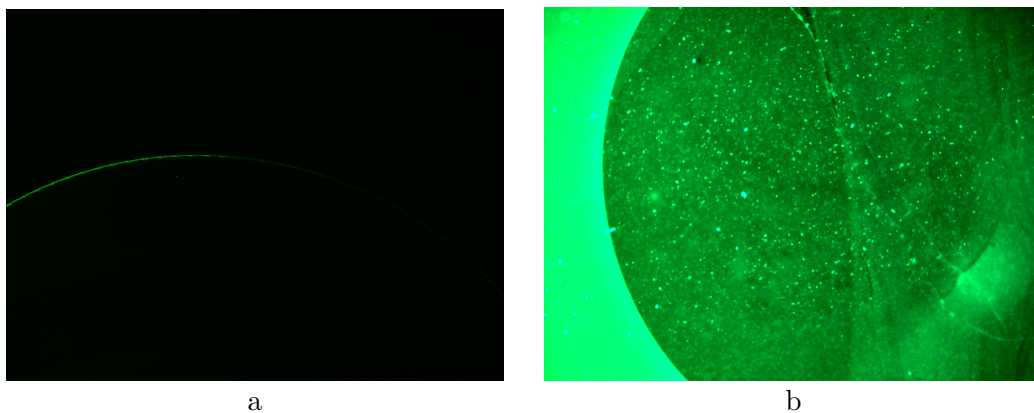
Figure 6.2.7: (a) Non-specific binding of the mouse IgG conjugate on silanized surface; (b) Fluorescence artifact. The circular area is where the fluorescent labeled Ab is applied.
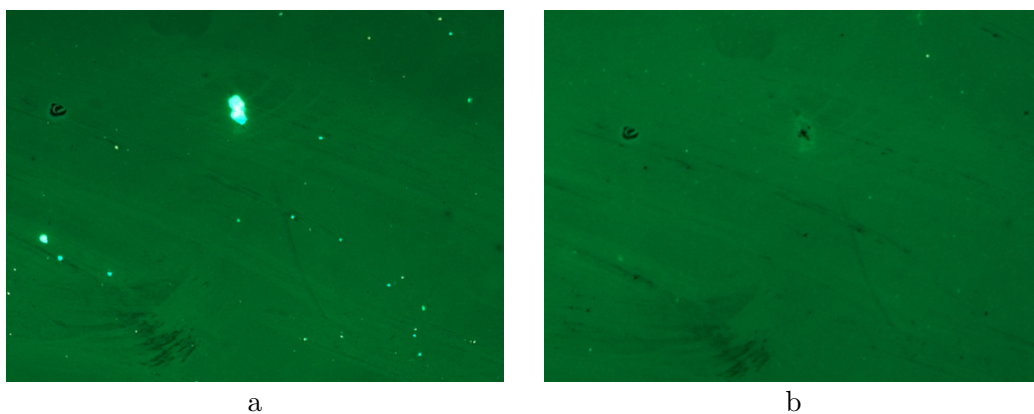
Figure 6.2.8: (a) Sample showing an amount of fluorescent clusters are sonicated in DIW resulting in (b) a cluster-free surface. Bare areas are left where the clusters were.

Table 6.2.1: Tabulated functionalization results from the CAM.

Sample	Contact angle ($° \pm$ SD)
Si_3N_4 reference	46.7 ± 3.2
Plasma oxidized	< 10
$15\,min$ LP silanization	44.7 ± 2.2
IgG functionalized	39.0 ± 1.4

6.3   Summary

Anti-mouse IgG capture antibodies were covalently immobilized to amino-silanized silicon nitride surfaces using carbodiimide crosslinking chemistry. Two protocols were tested, one where the capture antibodies were activated, i.e. method I, and one where the silanized surface was activated, i.e. method II. The immobilization step was characterized using fluorescence microscopy and fluorescent antibody conjugates.

Silanization using the aminosilane APTES was performed using both liquid phase (LP) and vapor phase method. The VP method resulted in more hydrophobic surfaces compared to the LP method, probably due to a more densely aminosilane layer formation. VP silanization resulted in more even fluorescence most of the times, and less cluster formation was seen overall with this method.

Immobilization of IgG capture antibodies was tested using different concentrations of EDC and NHS. Method I on VP silanized surfaces using the lowest concentration, i.e. 10-fold molar excess of EDC over the amount of IgG and NHS/EDC ratio of 4, resulted in the most uniform fluorescence although with traces of fluorescent clusters.

In order to investigate the mechanism behind antibody aggregation leading to large cluster formations, 15 min LP silanized surfaces were functionalized using different incubation times. The antibody solutions were sonicated for 10 s in order to dissolve present aggregates. The results showed that sonication of antibody solutions may be a quick and effective method for aggregate removal. The resulting surfaces showed signs of increasing cluster formation with increasing incubation time. Additionally, very high fluorescence uniformity was found using this method.

Chapter 7

Conclusion

The data obtained during the work of this thesis may contribute to a better understanding of necessary lithography techniques for developing micro- and nano-scale waveguide biosensors. The study of biofunctionalization protocols may provide increased knowledge regarding conjugation techniques suited for use in silicon nitride biosensors.

7.1 Material Deposition

Plasma enhanced chemical vapor deposition (PECVD) at $300\,°C$ was used to deposit silicon dioxide and silicon nitride with deposition rates of approximately $88\,nm/min$ and $15\,nm/min$, respectively, and resulting average surface roughness of $3.1\,nm$ and $0.4\,nm$, respectively. Although the SiO_2 recipe was well established the surface roughness is extensive, leading to possible large optical losses. Switching to thermally grown oxide is one measure to overcome this issue.

7.2 Silicon Nitride Etch

Two dry-etch recipes were tested using inductively coupled plasma reactive ion etch (ICP-RIE), one combined ICP-RIE and one RIE. The etch rates were found to be approximately $100\,nm/min$ and $53\,nm/min$, respectively. The low etch rate on the RIE etch enables more control when shallow rib waveguides are to be etched. However, a rib of height $30\,nm$ was easily achieved with both recipes. The resulting edge roughness was found to be

lower for the ICP-RIE etch but optical transmission measurements have to be performed in order to verify whether this has a significant impact on the optical losses as the mode is confined below the rib in these waveguides.

7.3   Biofunctionalization

Silanization with (3-Aminopropyl)triethoxysilane (APTES) was performed using both liquid phase (LP) and vapor phase (VP) protocols. The VP silanization yielded a more densely packed aminosilane layer with smaller agglomerates compared to the LP method and further a more uniformly distribution of immobilized capture antibodies. The VP protocol resulted in a more hydrophobic surface (CA = 58°) compared to the LP protocol (CA of 38° to 43°) which could result in more difficult wetting.

Carbodiimide crosslinking chemistry using N-(3-Dimethylaminopropyl)-N'-ethylcarbodiimide hydrochloride (EDC) and N-Hydroxysuccinimide (NHS) was performed with the aim of immobilizing anti-mouse IgG antibodies (Ab) to the primary amines on silanized surfaces. Two protocols were investigated, one where the EDC/NHS was used to activate the anti-IgG Ab prior to contact, and one where the amino-silanized surface was activated prior to contact. The latter should prevent Ab-Ab cross-binding but no significant difference was found. However, the results were dominated by aggregate formation, either in the primary Ab solution or in the secondary Ab solution, leading to large fluorescent clusters. Further experiments revealed that rapid sonication (10 s) of the Ab solutions reduced the aggregate formation and resulted in uniform fluorescence. An experiment investigating the effect of incubation time on the aggregate formation was performed indicating increased cluster formation with long incubation times. The shortest time used, i.e. 1 min seemed sufficient and yielded uniform fluorescence, however more experiments need to be performed in order to investigate whether covalent bonds have been formed this rapidly.

7.4   Future Work

Optical transmission measurement for determining propagation loss and coupling loss is essential and can further enable tuning of parameters for PECVD Si_3N_4 deposition and investigating bending losses in the MZI branch.

Developing a selective etch for the sensing window is necessary. The silicon dioxide cladding needs to be fully etched down to the silicon nitride core without damaging the rib waveguide. Further, the sensing window needs to be shaped such that it matches the properties of e.g. microfluidic channels, or other mechanisms used for analyte delivery.

Ellipsometry measurements can be performed in order to determine the thickness of deposited materials, including the aminosilane.

More thorough cleaning in order to break non-covalent bindings using e.g. $1\,M$ NaCl and $10\,\mathrm{m}M$ Tris buffer, alternatively combined with Tween80 could reveal whether short incubation times are sufficient.

The use of IgG whole molecule control with gold nano particles, attached using biotin and avidin or streptavidin, enables the use of SEM for the characterization of catcher distribution.

The immobilization of other catcher agents, specific towards desired analytes to investigate, might need other crosslinking chemistries than those investigated in this project. The field of bioconjugation is immense and requires vast experience and knowledge to even begin mastering. In-depth literature study and collaboration with experienced biochemists is crucial for processing a functional sensor.

Bibliography

[1] Katrien De Vos, Irene Bartolozzi, Etienne Schacht, Peter Bienstman, and Roel Baets. Silicon-on-insulator microring resonator for sensitive and label-free biosensing. *Optics express*, 15(12):7610–7615, 2007.

[2] Peihu Fan, Xiaojun Li, Weiheng Su, Wei Kong, Xianggui Kong, Zhenxin Wang, Youchun Wang, Chunlai Jiang, and Feng Gao. Enhanced sensitivity for detection of hiv-1 p24 antigen by a novel nuclease-linked fluorescence oligonucleotide assay. 2015.

[3] Mikael Kubista, José Manuel Andrade, Martin Bengtsson, Amin Forootan, Jiri Jonák, Kristina Lind, Radek Sindelka, Robert Sjöback, Björn Sjögreen, Linda Strömbom, et al. The real-time polymerase chain reaction. *Molecular aspects of medicine*, 27(2):95–125, 2006.

[4] Sino Biological Inc. ELISA Principle - Basis and Extension. `http://www.elisa-antibody.com/ELISA-Introduction/ELISA-Principle`, 2015.

[5] David Erickson, Sudeep Mandal, Allen HJ Yang, and Bernardo Cordovez. Nanobiosensors: optofluidic, electrical and mechanical approaches to biomolecular detection at the nanoscale. *Microfluidics and nanofluidics*, 4(1-2):33–52, 2008.

[6] Greg T. Hermanson. *Bioconjugate Techniques*. Academic Press, third edition edition, 2013.

[7] Ch Stamm, R Dangel, and W Lukosz. Biosensing with the integrated-optical difference interferometer: dual-wavelength operation. *Optics communications*, 153(4):347–359, 1998.

[8] Morten Hage. *Protein Detection Using a Mach-Zehnder Interferometer Biosensor - Investigation by Simulation.* Project thesis, Norwegian University of Science and Technology.

[9] Ginés Lifante. *Integrated Photonics: Fundamentals.* John Wiley & Sons, Ltd, 2005.

[10] Bahaa EA Saleh and Malvin Carl Teich. *Fundamentals of photonics*, volume 22. 1991.

[11] Dengpeng Yuan, Ying Dong, Yujin Liu, and Tianjian Li. Mach-zehnder interferometer biochemical sensor based on silicon-on-insulator rib waveguide with large cross section. *Sensors*, 15(9):21500–21517, 2015.

[12] Robert G Hunsperger. *Integrated optics: theory and technology*, volume 2. Springer, 1984.

[13] D.K. Cheng. *Field and Wave Electromagnetics.* Pearson Education Limited, 2014.

[14] Francisco Prieto, B Sepulveda, A Calle, Andreu Llobera, Carlos Domínguez, Antonio Abad, A Montoya, and Laura M Lechuga. An integrated optical interferometric nanodevice based on silicon technology for biosensor applications. *Nanotechnology*, 14(8):907, 2003.

[15] Mohammed Zourob, Sauna Elwary, and Anthony PF Turner. *Principles of Bacterial Detection: Biosensors, Recognition Receptors and Microsystems: Biosensors, Recognition Receptors, and Microsystems.* Springer Science & Business Media, 2008.

[16] Pascal Jonkheijm, Dirk Weinrich, Hendrik Schröder, Christof M Niemeyer, and Herbert Waldmann. Chemical strategies for generating protein biochips. *Angewandte Chemie International Edition*, 47(50):9618–9647, 2008.

[17] C Jime, J Perriere, I Vickridge, JP Enard, JM Albella, et al. Transformation of silicon nitride in oxygen plasma. *Surface and Coatings Technology*, 45(1):147–154, 1991.

[18] Joonyeong Kim, Joungmo Cho, Paul M Seidler, Nicholas E Kurland, and Vamsi K Yadavalli. Investigations of chemical modifications of amino-terminated organic films on silicon substrates and controlled protein immobilization. *Langmuir*, 26(4):2599–2608, 2010.

[19] Sandeep K Vashist, E Marion Schneider, and John HT Luong. Surface plasmon resonance-based immunoassay for human c-reactive protein. *Analyst*, 2015.

[20] Judith A Owen, Jenni Punt, Sharon A Stranford, and Patricia P Jones. *Kuby Immunology*. WH Freeman New York, 2013.

[21] Thermo Fisher Scientific Inc. Biotinylation. `https://www.thermofisher.com/no/en/home/life-science/protein-biology/protein-biology-learning-center/protein-biology-resource-library/pierce-protein-methods/biotinylation.html`, 2016.

[22] Jackson ImmunoResearch Inc. Selection of Secondary Antibodies. `https://www.jacksonimmuno.com/technical/products/antibody-selection`.

[23] Michael Quirk and Julian Serda. *Semiconductor manufacturing technology*, volume 1. Prentice Hall Upper Saddle River, NJ, 2001.

[24] AllResist GmbH. Positive E-Beam Resists AR-P 6200 (CSAR 62). `http://www.allresist.com/wp-content/uploads/sites/2/2015/12/allresist_produktinfos_ar-p6200_englisch.pdf`, 2015.

[25] Oxford Instruments plc. Plasma Enhanced Chemical Vapour Deposition. `http://www.oxford-instruments.com/products/etching-deposition-and-growth/plasma-etch-deposition/pecvd`, 2016.

[26] Mark Chiappa at NTNU NanoLab. *Elionix ELS-G100 - Short user guide*.

[27] Oxford Instruments plc. Inductively Coupled Plasma (ICP) Etching. `http://www.oxford-instruments.com/products/etching-deposition-and-growth/plasma-etch-deposition/icp-etch`, 2016.

[28] NorFab. ICP-RIE Chiller. `http://ntnu.norfab.no/WebForms/Equipment/EquipmentView.aspx?toolId=39`.

[29] TEFM Standaert, C Hedlund, EA Joseph, GS Oehrlein, and TJ Dalton. Role of fluorocarbon film formation in the etching of silicon, silicon dioxide, silicon nitride, and amorphous hydrogenated silicon carbide. *Journal of Vacuum Science & Technology A*, 22(1):53–60, 2004.

[30] Sandeep Kumar Vashist, Edmond Lam, Sabahudin Hrapovic, Keith B Male, and John HT Luong. Immobilization of antibodies and enzymes on 3-aminopropyltriethoxysilane-functionalized bioanalytical platforms for biosensors and diagnostics. *Chemical reviews*, 114(21):11083–11130, 2014.

[31] Sanjukta Guha Thakurta and Anuradha Subramanian. Fabrication of dense, uniform aminosilane monolayers: A platform for protein or ligand immobilization. *Colloids and Surfaces A: Physicochemical and Engineering Aspects*, 414:384–392, 2012.

[32] AW Flounders, DL Brandon, and AH Bates. Immobilization of thiabendazole-specific monoclonal antibodies to silicon substrates via aqueous silanization. *Applied biochemistry and biotechnology*, 50(3):265–284, 1995.

[33] Sandeep Kumar Vashist. A highly-sensitive and rapid surface plasmon resonance immunoassay procedure based on the covalent-orientated immobilization of antibodies. *Protocol Exchange*, 2011.

[34] Sandeep Kumar Vashist. Comparison of 1-ethyl-3-(3-dimethylaminopropyl) carbodiimide based strategies to crosslink antibodies on amine-functionalized platforms for immunodiagnostic applications. *Diagnostics*, 2(3):23–33, 2012.

[35] Dohyun Kim and Amy E Herr. Protein immobilization techniques for microfluidic assays. *Biomicrofluidics*, 7(4):041501, 2013.

[36] Tohid Fatanat Didar, Amir M Foudeh, and Maryam Tabrizian. Patterning multiplex protein microarrays in a single microfluidic channel. *Analytical chemistry*, 84(2):1012–1018, 2011.

[37] Thermo Fisher Scientific Inc. Alexa Fluor® 488 dye. https://www.thermofisher.com/no/en/home/life-science/cell-analysis/fluorophores/alexa-fluor-488.html, 2016.

[38] NorFab. AFM Veeco. http://ntnu.norfab.no/WebForms/Equipment/EquipmentView.aspx?toolId=2.

[39] Bruker Nano Inc. SCANASYST-AIR. http://www.brukerafmprobes.com/p-3726-scanasyst-air.aspx, 2016.

[40] M Raposo, Q Ferreira, and PA Ribeiro. A guide for atomic force microscopy analysis of soft-condensed matter. *Modern research and educational topics in microscopy*, 1:758–769, 2007.

[41] Olympus. Knowledge: Roughness (2D) parameter. http://www.olympus-ims.com/en/knowledge/metrology/roughness/2d_parameter/, 2016.

[42] Filmetrics Inc. Filmetrics F20 series. http://www.filmetrics.com/thicknessmeasurement/f20, 2016.

[43] Hitachi High-Technologies. *Ultra-high Resolution Scanning Electron Microscope - Hitachi S-5500*.

[44] United States Carl Zeiss Microscopy, LLC. Filter Assistant. https://www.micro-shop.zeiss.com/?s=31547860f8dce1&l=en&p=us&f=f&a=v&b=f&id=489038-9901-000&o=, 2016.

[45] Xiangxuan Zeng, Guohua Xu, Yuan Gao, and Yue An. Surface wettability of (3-aminopropyl) triethoxysilane self-assembled monolayers. *The Journal of Physical Chemistry B*, 115(3):450–454, 2010.

[46] Roger P Woodward. Contact angle measurements using the drop shape method. *First Ten Angstroms Inc., Portsmouth, VA*, 1999.

[47] Darren L Williams, Anselm T Kuhn, Mark A Amann, Madison B Hausinger, Megan M Konarik, and Elizabeth I Nesselrode. Computerised measurement of contact angles. *Galvanotechnik*, 101(11):2502, 2010.

[48] Souren P Pogossian, Lili Vescan, and Adrian Vonsovici. The single-mode condition for semiconductor rib waveguides with large cross section. *Lightwave Technology, Journal of*, 16(10):1851–1853, 1998.

[49] Firehun Tsige Dullo, Jean-Claude Tinguely, Stian Andre Solbø, and Olav Gaute Hellesø. Single-mode limit and bending losses for shallow rib waveguides. *Photonics Journal, IEEE*, 7(1):1–11, 2015.

[50] Ananth Z Subramanian, Pieter Neutens, Ashim Dhakal, Roelof Jansen, Tom Claes, Xavier Rottenberg, Frederic Peyskens, Shankar Selvaraja, Philippe Helin, Beatrice Dubois, et al. Low-loss singlemode pecvd silicon nitride photonic wire waveguides for 532-900 nm wavelength window fabricated within a cmos pilot line. *Photonics Journal, IEEE*, 5(6):2202809–2202809, 2013.

[51] Muhammad Rizwan Amirzada, Andreas Tatzel, Volker Viereck, and Hartmut Hillmer. Surface roughness analysis of sio2 for pecvd, pvd and ibd on different substrates. *Applied Nanoscience*, pages 1–8, 2015.

[52] Lars Grønmark Holmen. *Silicon Photonic Crystal Mach-Zehnder Interferometer*. Master's thesis, Norwegian University of Science and Technology.

[53] Jinpian Diao, Dacheng Ren, James R Engstrom, and Kelvin H Lee. A surface modification strategy on silicon nitride for developing biosensors. *Analytical biochemistry*, 343(2):322–328, 2005.

[54] Amrita R Yadav, Rashmi Sriram, Jared A Carter, and Benjamin L Miller. Comparative study of solution–phase and vapor–phase deposition of aminosilanes on silicon dioxide surfaces. *Materials Science and Engineering: C*, 35:283–290, 2014.

[55] M Terracciano, I Rea, J Politi, and L De Stefano. Optical characterization of aminosilane-modified silicon dioxide surface for biosensing. *Journal of the European Optical Society-Rapid publications*, 8, 2013.

[56] Mojun Zhu, Maria Z Lerum, and Wei Chen. How to prepare reproducible, homogeneous, and hydrolytically stable aminosilane-derived layers on silica. *Langmuir*, 28(1):416–423, 2011.

[57] Joong Ho Moon, Jin Ho Kim, Ki-jeong Kim, Tai-Hee Kang, Bong-soo Kim, Chan-Ho Kim, Jong Hoon Hahn, and Joon Won Park. Absolute surface density of the amine group of the aminosilylated thin layers: ultraviolet-visible spectroscopy, second harmonic generation, and synchrotron-radiation photoelectron spectroscopy study. *Langmuir*, 13(16):4305–4310, 1997.

[58] Rory Stine, Christina L Cole, Kristy M Ainslie, Shawn P Mulvaney, and Lloyd J Whitman. Formation of primary amines on silicon nitride surfaces: a direct, plasma-based pathway to functionalization. *Langmuir*, 23(8):4400–4404, 2007.

[59] T Hayashi, TG Castner, and Robert W Boyd. Quenching of molecular fluorescence near the surface of a semiconductor. *Chemical physics letters*, 94(5):461–466, 1983.

[60] Lina Yoo, Keum-Young Ahn, Ji-Young Ahn, Thomas Laurell, Yong Man Lee, Pil J Yoo, and Jeewon Lee. A simple one-step assay platform based on fluorescence quenching of macroporous silicon. *Biosensors and Bioelectronics*, 41:477–483, 2013.

[61] Max Born and Emil Wolf. *Principles of optics: electromagnetic theory of propagation, interference and diffraction of light.* Cambridge university press, 1999.

Appendices

Appendix A

Fundamental Maxwell Theory

Maxwell's equations are a set of partial differential equations that describe the propagation of electromagnetic waves through a medium. These equations have two main variants, the microscopic and the macroscopic set. Whereas the microscopic set includes the atomic level charges and currents, the macroscopic set circumvents this by defining the auxiliary fields $\mathbf{D}$ and $\mathbf{H}$, i.e the electric flux density and magnetic field intensity, respectively [13, Ch. 3.8, 6.7]

$$\mathbf{D}(\mathbf{r},t) = \epsilon_0 \mathbf{E} + \mathbf{P}(\mathbf{r},t) \tag{A.1}$$

$$\mathbf{H}(\mathbf{r},t) = \frac{1}{\mu_0}\mathbf{B}(\mathbf{r},t) - \mathbf{M}(\mathbf{r},t) \tag{A.2}$$

where ϵ_0 is the vacuum permittivity, $\mathbf{E}$ is the electric field intensity, $\mathbf{P}$ is the polarization, μ is the vacuum permeability, $\mathbf{B}$ is the magnetic flux density and $\mathbf{M}$ is the magnetization. In linear, isotropic and homogeneous media, these have the constitutive relations

$$\mathbf{D} = \epsilon \mathbf{E} \tag{A.3}$$

$$\mathbf{H} = \frac{1}{\mu}\mathbf{B} \tag{A.4}$$

where ϵ and μ are the absolute permittivity and the absolute permeability, respectively.

The macroscopic Maxwell's equations, together with the continuity equation [13, p. 322] and the Lorentz's force equation [13, p. 226], form the foundation of electromagnetic theory. These equations are powerful tools enabling

explanation and prediction of *all* macroscopic electromagnetic phenomena [13, Ch. 7.3].

The macroscopic Maxwell's equations are

$$\boldsymbol{\nabla} \times \mathbf{E} = -\frac{\partial \mathbf{B}}{\partial t} \tag{A.5}$$

$$\boldsymbol{\nabla} \times \mathbf{H} = \mathbf{J} + \frac{\partial \mathbf{D}}{\partial t} \tag{A.6}$$

$$\boldsymbol{\nabla} \cdot \mathbf{D} = \rho \tag{A.7}$$

$$\boldsymbol{\nabla} \cdot \mathbf{B} = 0 \tag{A.8}$$

where, ρ is the volume density of *free charges* and $\mathbf{J}$ is the density of *free currents*. The equations (A.5)-(A.7) are individually called Faraday's law, Ampère's law and Gauss's law, respectively. Equation (A.8) states that there are no isolated magnetic charges, i.e there are no magnetic monopoles [13, Ch. 7.3].

A.1 Boundary Conditions

In order to solve Maxwell's differential equations, a set of boundary conditions need to be determined. At a boundary between two lossless linear dielectrics, the conditions are [13, p. 330]

$$E_{1t} = E_{2t} \tag{A.9a}$$
$$H_{1t} = H_{2t} \tag{A.9b}$$
$$D_{1n} = D_{2n} \tag{A.9c}$$
$$B_{1n} = B_{2n} \tag{A.9d}$$

where n and t represent the normal and tangential component, respectively, in medium 1 and 2.

A.2 Solutions to Maxwell's equations

We are interested in solving Maxwell's equations for a lossless dielectric. In such media, $\rho = 0$ and $J = 0$, i.e. there are no free charges or currents present. Equations (A.5) to (A.8) are first order differential equations for

the variables $\mathbf{E}$ and $\mathbf{H}$. To get second order equations for $\mathbf{E}$ and $\mathbf{H}$ alone, they can be combined. Taking the curl of (A.5) and using (A.6) yields

$$\nabla^2\mathbf{E} = \frac{1}{u^2}\frac{\partial^2\mathbf{E}}{\partial t^2} \tag{A.10}$$

where u is the speed of light in the medium. In a similar way we obtain an equation for $\mathbf{H}$.

$$\nabla^2\mathbf{H} = \frac{1}{u^2}\frac{\partial^2\mathbf{H}}{\partial t^2} \tag{A.11}$$

These are called the homogeneous vector wave equations [13, p. 335].

Since the electromagnetic field varies sinusoidally with time, the phasor notation for the time-harmonic electric and magnetic field is chosen as it is more convenient in calculations [13, Ch. 7.2]

$$\mathbf{E}(x,y,z,t) = \mathrm{Re}\big\{\mathbf{E}(x,y,z)e^{j\omega t}\big\} \tag{A.12}$$

$$\mathbf{H}(x,y,z,t) = \mathrm{Re}\big\{\mathbf{H}(x,y,z)e^{j\omega t}\big\}. \tag{A.13}$$

A.3   Time-harmonic Maxwell's equations

The time-harmonic Maxwell's equations for linear, isotropic and homogeneous media can be found by applying Maxwell's equations to the time-harmonic field, yielding [13, p. 339]

$$\nabla \times \mathbf{E} = -j\omega\mu\mathbf{H} \tag{A.14a}$$
$$\nabla \times \mathbf{H} = \mathbf{J} + j\omega\epsilon\mathbf{E} \tag{A.14b}$$
$$\nabla \cdot \mathbf{E} = \rho/\epsilon \tag{A.14c}$$
$$\nabla \cdot \mathbf{H} = 0. \tag{A.14d}$$

For simple source-free, non-conducting media characterized by $\rho = 0$, $\mathbf{J} = 0$ and $\sigma = 0$, time-harmonic Maxwell's equations simplify to

$$\nabla \times \mathbf{E} = -j\omega\mu\mathbf{H} \tag{A.15a}$$
$$\nabla \times \mathbf{H} = j\omega\epsilon\mathbf{E} \tag{A.15b}$$
$$\nabla \cdot \mathbf{E} = 0 \tag{A.15c}$$
$$\nabla \cdot \mathbf{H} = 0. \tag{A.15d}$$

By inserting the phasor notation of **E** and **H** in (A.10) and (A.11) we obtain

$$\nabla^2 \mathbf{E} + k^2 \mathbf{E} = 0 \tag{A.16}$$

and

$$\nabla^2 \mathbf{H} + k^2 \mathbf{H} = 0 \tag{A.17}$$

which are the homogeneous vector Helmholtz's equations [13, p. 340].

If we assume that the waves of interest propagate in the positive z-direction, with a propagation constant $\gamma = \alpha + j\beta$, with α being the attenuation constant and β the phase constant, the dependence on z and t for all field components can be described by

$$e^{-\gamma z} e^{j\omega t} = e^{-\alpha z} e^{j(\omega t - \beta z)}. \tag{A.18}$$

We can now describe the **E**-field in Cartesian coordinates as

$$\mathbf{E}(x, y, z, t) = \mathrm{Re}\big\{\mathbf{E}^0(x, y) e^{j\omega t - \gamma z}\big\} \tag{A.19}$$

where $\mathbf{E}^0$ is a two dimensional vector phasor depending on the cross sectional coordinates only.

The homogeneous vector Helmholtz-s equation (A.10) can be broken into two parts for the cross-sectional and longitudinal coordinates

$$
\begin{aligned}
\nabla^2 \mathbf{E} &= (\nabla_{xy}^2 + \nabla_z^2)\mathbf{E} = \left(\nabla_{xy}^2 + \frac{\partial^2}{\partial z^2}\right)\mathbf{E} \\
&= \nabla_{xy}^2 \mathbf{E} + \gamma^2 \mathbf{E}.
\end{aligned} \tag{A.20}
$$

Combining (A.10) and (A.20) give

$$\nabla_{xy}^2 \mathbf{E} + (\gamma^2 + k^2)\mathbf{E} = 0 \tag{A.21a}$$

$$\nabla_{xy}^2 \mathbf{E} + h^2 \mathbf{E} = 0 \tag{A.21b}$$

with $h^2 = \gamma^2 + k^2$, and similarly from (A.11) we have

$$\nabla_{xy}^2 \mathbf{H} + h^2 \mathbf{H} = 0. \tag{A.22}$$

The interrelationship among the six components of **E** and **H** can be examined by expanding the source-free curl equations (A.15a) to (A.15d). By manipulating the resulting equations, [13, p. 523], the transverse field components can be expressed in terms of the longitudinal components

$$H_x^0 = -\frac{1}{h^2}\left(\gamma\frac{\partial H_z^0}{\partial x} - j\omega\epsilon\frac{\partial E_z^0}{\partial y}\right) \tag{A.23}$$

$$H_y^0 = -\frac{1}{h^2}\left(\gamma\frac{\partial H_z^0}{\partial y} + j\omega\epsilon\frac{\partial E_z^0}{\partial x}\right) \tag{A.24}$$

$$E_x^0 = -\frac{1}{h^2}\left(\gamma\frac{\partial E_z^0}{\partial x} + j\omega\mu\frac{\partial H_z^0}{\partial y}\right) \tag{A.25}$$

$$E_y^0 = -\frac{1}{h^2}\left(\gamma\frac{\partial E_z^0}{\partial y} - j\omega\mu\frac{\partial H_z^0}{\partial x}\right) \tag{A.26}$$

where $h^2 = \gamma^2 + k^2 = \gamma^2 + \omega^2\mu\epsilon$. In a lossless dielectric, $\alpha = 0 \rightarrow \gamma = j\beta$.

In a similar way, equations for the longitudinal component of the electric and magnetic field can be established yielding the reduced wave equations for channel waveguides [9, p. 86]

$$\frac{\partial^2 E_z}{\partial x^2} + \frac{\partial^2 E_z}{\partial y^2} = \left[\beta^2 - k^2 n^2\right] E_z \tag{A.27}$$

$$\frac{\partial^2 H_z}{\partial x^2} + \frac{\partial^2 H_z}{\partial y^2} = \left[\beta^2 - k^2 n^2\right] H_z. \tag{A.28}$$

Note that the longitudinal components of the fields are in fact not independent, but related by

$$\beta\frac{\partial H_z}{\partial x} = \epsilon_0 n^2 \omega\frac{\partial E_z}{\partial y}. \tag{A.29}$$

A.3.1 Limitations of Maxwells's equations

Maxwell's equations are an approximation to the fundamental theory of quantum electrodynamics and can be quite inaccurate. For extremely strong fields or extremely short distances, some of Maxwell's equations need to be supplemented by higher power field components.[61, Ch. 1]

Appendix B

Nanolab Cources

- NanoLab Introduction
- Chemical Area
- Chemical Basics
- Lithography Area
- Plasma Enhanced Chemical Vapor Deposition (PECVD)
- Inductively Coupled Plasma - Reactive Ion Etch (ICP-RIE)
- Scriber
- Electron Beam Lithography (Elionix EBL)
- Scanning Transmission Electron Microscope (S(T)EM)
- Profilometer
- Plasma Cleaner
- Atomic Force Microscope (AFM)
- Fluorescence Microscope

Appendix C

Matlab Code

C.1 Single-mode Calculation using EIM

```matlab
% ————————————————————————————————————————————————————————
% ——————————————————————— Mode_calculation ———————————————————————
% ————————————————————————————————————————————————————————
% The script uses the waveguide geometry dimensions to calculate
% and plot conditions for single—mode propagation using the
% function single_mode_SiN.

close all
clear

% geometry
W_rib = 1e—6:1e—6:3e—6;                  % rib width
H_core = 550e—9;                         % core thickness
H_rib = 10e—9:1e—9:50e—9;                % rib height
h = H_core—H_rib;

% preallocating space
TEresult = zeros(length(H_rib),length(W_rib));
TMresult = zeros(length(H_rib),length(W_rib));

% uses function single_mode_SiN()
for i=1:length(H_rib)
    for j=1:length(W_rib)
    TEresult(i,j) = single_mode_SiN(W_rib(j),H_core,h(i), 'TE');
    TMresult(i,j) = single_mode_SiN(W_rib(j),H_core,h(i), 'TM');

    end
end

% legends
first  = ['TE ' num2str(W_rib(1)/1e—6) ,char(181),'m'];
second = ['TE ' num2str(W_rib(2)/1e—6) ,char(181),'m'];
third  = ['TE ' num2str(W_rib(3)/1e—6) ,char(181),'m'];
fourth = ['TM ' num2str(W_rib(1)/1e—6) ,char(181),'m'];
fifth  = ['TM ' num2str(W_rib(2)/1e—6) ,char(181),'m'];
sixth  = ['TM ' num2str(W_rib(3)/1e—6) ,char(181),'m'];

% plot
hfig = figure();
x = H_rib*1e9;
threshold(1:length(x)) = 0;
```

```matlab
plot(x, TEresult, x, TMresult, '--', 'LineWidth', 1.5);
hold on
legend(first, second, third, fourth, fifth, sixth);
set(gca, 'fontsize', 22);
axis([x(1) x(end) -inf inf]);

% making colorbox
ax = gca;
y = zeros(1,length(H_rib));          % single-mode boundary
baseline = ax.YTick(end)*(y+1)+3;    % upper boundary for colorbox
Y = [x fliplr(x)];
X = [baseline fliplr(y)];
upfill = fill(Y,X,'r');
set(upfill, 'facealpha', .8, 'edgecolor', 'none');
title 'Geometry limitations for single-mode propagation';
xlabel 'rib height (nm)'
ylabel 'au'

% saving to .pdf
savename = ['TE_TM_', num2str(H_core*1e9)];
hfig.PaperUnits = 'inches';
hfig.PaperPosition = [0 0 10 7];
hfig.PaperSize = [10 7];
hfig.PaperPositionMode = 'manual';
saveas(hfig, strcat(savename, 'PDF.pdf'));
```

```matlab
% ———————————————————————————————————————————————————————————————————
% ————————————————————————— Function SingleMode ————————————————————————
% ———————————————————————————————————————————————————————————————————
% The function takes the waveguide width (w), core height (H) and
% silicon nitride thickness (h) as inputs and returns a value
% based on the mode properties of the waveguide.
% If the returned value is less than 0, only the fundamental mode
% will propagate.

function [y] = single_mode_SiN(w, H, h, mode)

% refractive index of the materials
n_c = 1.44; n_f = 2.00; n_s = 1.44;
% where n_c is  the cover layer, n_f is the core, n_s is the
% substrate

if strcmp(mode,'TE')
gamma_s = 1; gamma_c = 1;                       % for TE
elseif strcmp(mode,'TM')
gamma_s = (n_s/n_f)^2; gamma_c = (n_c/n_f)^2;   % for TM
end
lambda = 633e-9;                                % wavelength
k = 2*pi()/lambda;                              % wave vector

% calculations
q = gamma_c/(k*sqrt(n_f^2-n_c^2)) +...
    gamma_s/(k*sqrt(n_f^2-n_s^2));
h_eff = h+q;
H_eff = H+q;
w_eff = w + (2*gamma_c)/(k*sqrt(n_f^2-n_c^2));
t = w_eff/H_eff;
r = h_eff/H_eff;

% single mode when t < r/sqrt(1-r^2) & r > 0.5
if r <= 0.5
    % return 0
    y=0;
else
    % return the difference
    for i=1:length(t)
    y = t - r(i)/sqrt(1-r(i)^2);
    end
end
```

Appendix D

Biofunctionalization

D.1 Biofunctionalization Protocol

The chosen methods for the immobilization of catcher antibodies are illustrated as flowcharts in Figure D.1.1 and Figure D.1.2, and the necessary process steps are described in the following sections. A detailed listing of the chemicals used are given in Table D.3.1.
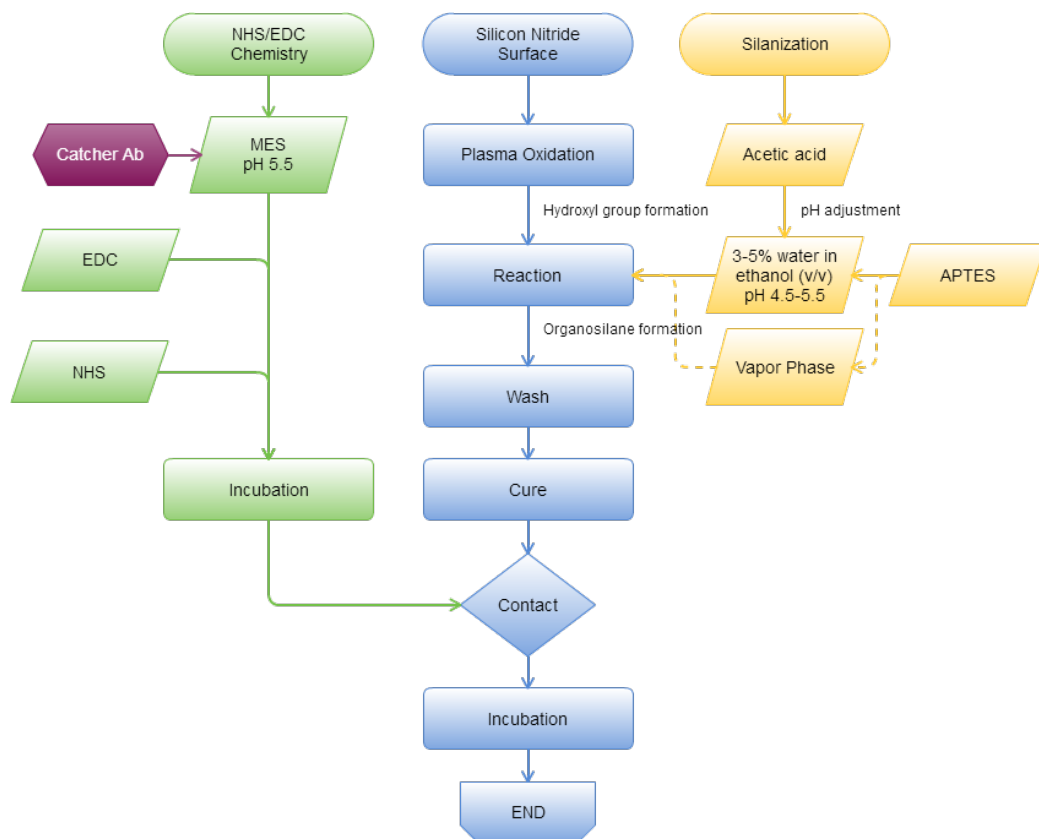
Figure D.1.1: Flowchart illustrating the process steps involved in biofunctionalization method I. The antibody to be immobilized is activated with EDC/NHS chemistry before applied to the APTES silanized surface.
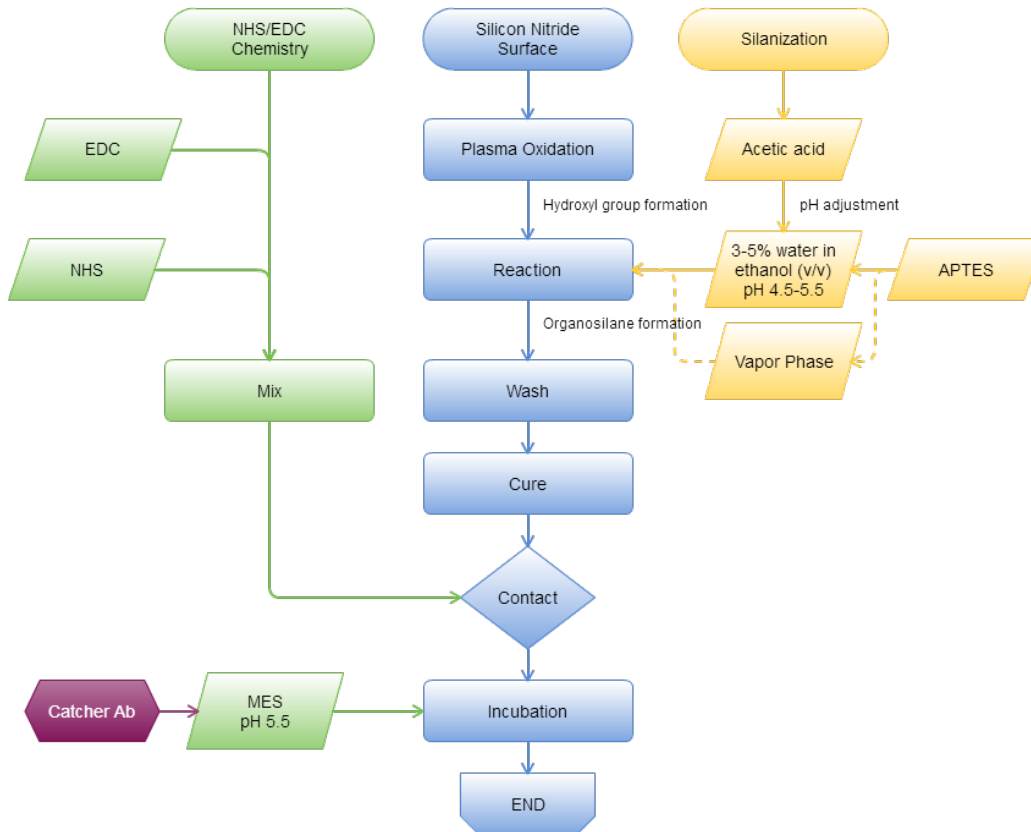
Figure D.1.2: Flowchart illustrating the process steps involved in biofunctional-ization method II. The APTES silanized surface is activated using EDC/NHS chemistry before the antibody to immobilize is applied.

D.2 APTES Silanization

The following protocol describes the process steps involved in both vapor-phase and liquid-phase silanization procedure using APTES [6, Ch. 13.1.1][6, Ch. 13.1.4].

Liquid-phase Protocol

1. Prepare solution containing 3 to 5 % water in ethanol (v/v) and adjust the pH to 4.5 to 5.5 using acetic acid.

2. Dissolve APTES in the solution prepared in step 1 with stirring to final concentration of 2 to 5 % (v/v). Allow hydrolysis for 5 min at RT to form reactive silanols.

3. Contact the silicon substrate for 2 min to several hours. The time determines the degree of organosilane polymer being deposited on the surface.

4. Wash the substrate with ethanol or the water/ethanol mixture to remove excess silane compound.

5. Cure the modified substrate by incubation at 110 °C for 30 min, alternatively at RT in a low humidity environment, or under vacuum.

Vapor-phase Protocol

1. Place the substrate to be modified in an enclosed chamber, e.g. vacuum desiccator, with the surface to be modified exposed.

2. Place the organosilane in a small reservoir below or adjacent to the substrate.

3. Apply vacuum to the chamber until silane volatilization occurs. Clamp off the vacuum tubing to maintain vacuum.

4. React for 4 to 24 h to result in a uniform organosilane layer.

D.3 EDC/NHS Chemistry

The following protocol describes the process steps involved in the EDC/NHS chemistry [6, Ch. 4.1.2].

Protocol

1. Dissolve the protein to be modified at a concentration of 1 to $10\,\mathrm{mg\,ml^{-1}}$ in 0.1-M sodium phosphate, pH 7.4.

2. Dissolve the molecule to be coupled in the buffer used in step 1. Add them to the reaction in at least a 10-fold excess over the amount of protein present.

3. Add the solution prepared in step 2 to the protein solution to obtain at least a 10-fold molar excess over the amount of protein present.

4. Add EDC to the solution in step 3 to obtain at least a 10-fold molar excess of EDC over the amount of protein present. Alternatively use a 0.05 to 0.1-M EDC. Add sulfo NHS to bring the final concentration to $5\,\mathrm{m}M$. Mix to dissolve. If this ratio of EDC/sulfo-NHS results in precipitation, scale back the amount of addition until a soluble conjugate is obtained.

5. React for $2\,\mathrm{h}$ at RT.

6. Purify conjugate by gel filtration or dialysis. If some turbidity has formed during conjugation, removal by centrifugation or filtration is advised.

Table D.3.1: Detailed listing of materials used for biofunctionalization.

Material	Quantity	Purity (%)	Concentration (mg/mL)	Molecular weight (g/mol)
Anti-mouse IgG (H+L)	2 mg	-	1.95	150000
Mouse IgG2a, Alexa Fluor® 488 conjugate	100	-	1	-
APTES	100 mL	99	-	221.37
EDC	1 g	-	-	191.70
NHS	25 g	98	-	115.09
MES	-	99.5	-	213.25
Acetic acid	100 mL	99	-	60.05
Sodium hydroxide	-	98	-	40.00
Acetone	1 L	99.9	-	-